
An Investigation of Single Wind Turbine Wakes with Static LiDAR Wind Profilers

Author:

Rannveig Oftedal Eikill

Supervisor:

Joachim Reuder

Co-supervisor:

Valerie-Marie Kumer

Finn Gunnar Nielsen

Master Thesis in Energy

Specialization: Renewable energy - Wind energy

June 2016



UNIVERSITY OF BERGEN
GEOPHYSICAL INSTITUTE

Abstract

Three static LiDAR wind profilers were deployed during the seven month field experiment WINTWEX-W at ECN's test site in Wieringermeer. The campaign was focused on capturing the structure and dynamics of the wake of a NORDEX N80 research wind turbine. The campaign has created a unique dataset for corresponding investigations. For this study also sonic anemometer and temperature difference measurement from a 108 m meteorological mast and SCADA data from the wind turbine have been used, in addition to the static LiDAR wind profiler datasets.

The compilation of a reliable LiDAR dataset for the campaign has been accomplished through a thorough re-examination of the raw measurements, and the development and application of an advanced de-spiking routine. Combining atmospheric data with SCADA data from the turbine, measurements of horizontal wind speed deficits and turbulence intensities in the wake region were analysed with respect to both atmospheric boundary layer stability and blade pitch angles. The results show an increased wake effect for stable stratifications in general, with wind speed deficits larger than 40%, and an increase in absolute TI of more than 10%. The main effect of the blade pitch happens in the angle interval between 0° and 3° . For pitch angles exceeding 3° , stability seemed to no longer have an affect on the wake strength, which additionally becomes substantially reduced.

Acknowledgements

First of all I would like to express my thanks to my supervisor Joachim Reuder for his support and encouragement throughout the last year. His ideas and enthusiasm have helped me immensely, along with his patient advice and valuable comments. I would also like to express my deepest gratitude to my co-supervisor Valerie-Marie Kumer for all her ideas and guidance, and for always being available for questions. I am also grateful to my co-supervisor Finn Gunnar Nielsen for helping me find out which direction I wanted to focus my thesis on.

I want to express my sincere thanks to NORCOWE and ECN for providing detailed wind measurements and SCADA data. A special thanks goes out to Jan Willem Wagenaar for his help in everything concerning the campaign data.

I also owe thanks to the "turbulence group" at the Geophysical institute for useful ideas and remarks, and in particular to my co-supervisor Valerie-Marie Kumer and PhD student Stephan Kral for their help in the development of the de-spiking routine used in this thesis.

I am also extremely thankful for all the support and encouragement my family has offered. My big-sister, Karen, deserves an extra thanks for offering to be my own personal proofreader in the final stages of writing my thesis.

Finally I would like to thank, from the bottom of my heart, my fellow students at GFI for five excellent years.

Contents

1	Introduction	5
2	Theory	9
2.1	Extracting wind power	9
2.1.1	Wind energy	9
2.2	Atmospheric boundary layer	10
2.2.1	Turbulence	12
2.2.1.1	Horizontal turbulence intensity	13
2.2.1.2	Turbulent kinetic energy	13
2.2.2	Stability	14
2.2.2.1	Wind profile	16
2.3	LiDAR Measurement principles	17
2.3.1	Wind vector	17
2.3.2	Carrier to Noise Ratio	19
2.3.3	Benefits	20
2.3.4	Disadvantages	20
3	Measurement Campaign and Instrumentation	23
3.1	Test site location	23
3.2	Instrumentation	25
3.2.1	LiDAR	25
3.2.2	Meteorological mast	25
3.2.2.1	Sonic anemometer	26
3.2.2.2	Temperature difference sensor	27

3.2.3	Turbine measurements	27
3.3	Campaign set-up	27
4	Data Overview and Quality Control	30
4.1	CNR and wipercount	31
4.2	De-spiking	33
4.3	Final LiDAR dataset	33
4.4	Data availability	35
5	Site Characterization	36
5.1	Characterizing structure disturbances	36
5.1.1	Effects on horizontal wind speed	40
5.1.1.1	Upstream instruments	40
5.1.1.2	Downstream instruments	43
5.1.2	Effects on horizontal turbulence intensity	43
5.2	Estimations of atmospheric stability	46
5.2.1	Finding stability criteria	46
5.2.2	Stability distribution	48
5.3	Wind distribution throughout the campaign	50
5.3.1	Horizontal wind speed	50
5.3.2	Wind direction	51
6	Effects of Stability	53
6.1	Vertical profiles	53
6.1.1	Horizontal wind speed deficit	54
6.1.2	Horizontal turbulence intensity	57
6.2	Wind distribution	59
7	Effects of Turbine Control	61
7.1	Effects of blade pitch angles on horizontal wind speed at hub height	62
7.2	Vertical profiles	63
7.3	Sample size	67

8 Conclusion	68
8.1 Summary	68
8.2 Further Outlook	70
Appendix A Weekly plots	73
Bibliography	102

Chapter 1

Introduction

The increased demand for renewable energy has led to great advancements in the use of wind power as an energy resource. Over the last 15 years the global cumulative installed wind capacity has grown by more than a factor of 20 (Global Wind Energy Council (GWEC), 2015). Even though this rapid increase cannot be expected to last, wind power is becoming of vital importance in the global energy production. For the further development and improvement of wind energy applications a detailed understanding of the wind turbine's effect on its surrounding is needed. This information is of particular importance for the improvement of modelling capabilities under the aspect of wind turbine and wind farm optimization and the prediction of power output and load estimates.

The wind field behind a wind turbine is in general characterized by a reduction in wind speed and an increase in turbulent mixing, and is referred to as the wind turbine's wake. The turbine acts to draw momentum out of the incoming air, and the loss of momentum in the flow is the cause of the reduced velocity in the wind propagating downstream. The wake will eventually dissolve by entraining undisturbed air with higher kinetic energy from the surroundings into the wake region, and the dissipation of the wake returns the boundary layer back to its original state. As the reduced wind results in a lower power output, and the increased turbulence leads to greater loads on the turbines further downstream, the understanding the wake

structure (e.g. vertical and horizontal extension and the magnitude of the wake deficit) and the wake dynamics (e.g. wake meandering) is of great relevance in wind farm operations (e.g., Kumer et al., 2015; Barthelmie et al., 2013). The wake structure is extremely intricate. Its characteristics change not only with turbine size and turbine controls, but also with the state of the surrounding atmospheric boundary layer (ABL). Several studies show that the atmospheric stability has a significant effect on the turbine's wake losses as it directly affects the power output (e.g. Alblas et al., 2014; Barthelmie et al., 2013; Westerhellweg et al., 2014). The suppression of turbulent mixing in a stably stratified boundary layer additionally affects the wake evolution, and can lead to a slower wake recovery and higher wind speed deficits in the wake region (Westerhellweg et al., 2013).

Wind turbine wakes are a current research topic and have been addressed by different approaches and methods. Results from both, wind tunnel studies (e.g., Chamorro and Porté-Agel, 2011; Zhang et al., 2013) and model simulations (e.g., Fitch et al., 2012; Wu and Porté-Agel, 2012) have contributed to a better understanding of wake dynamics. However, full scale measurements are needed for the validation of these results. Atmospheric measurements of the wake have been performed by the help of instrumented meteorological towers, so-called met-masts (e.g., Schepers et al., 2012). The rapid development of remote sensing instrumentation during the last decade has provided reliable data sets with appropriate spatial and temporal resolution for full scale wake observations (e.g., Kumer et al., 2015; Iungo and Porté-Agel, 2014; Banta et al., 2015). As turbines continue to grow in both capacity and size, remote sensing measurements, e.g. LiDARs, are, due to their increased flexibility as well as reaching altitudes exceeding most met-masts, becoming increasingly important contributors in wind energy research. However, most full scale LiDAR studies have been limited to relatively short measurement periods (e.g., Iungo et al., 2013; Banta et al., 2015; Wagner, R & Courtney, 2010). In addition suffer many corresponding studies from limited access to turbine control data for a detailed analysis of the wake measurements. There is also often a challenge with respect to publishing results from the analysis of that data, as

many commercial actors in the field regard this information as highly confidential. As such, the Wind Turbine Wake EXperiment Wieringermeer (WINTWEX-W) is the source for a unique data set, providing both atmospheric measurements from LiDARs and sonic anemometers and Supervisory Control And Data Acquisition (SCADA) from a NORDEX N80 wind turbine.

The main goal of this thesis was to gain a better understanding of single turbine wakes using measurements taken by several static LiDAR wind profilers placed upstream and downstream of a NORDEX N80 research wind turbine in prevailing wind conditions. Supplementary data from a 108 m meteorological mast, placed in the vicinity of the upstream LiDAR, was also used in this study. The analysis is in particular focussed on the wake's response to stability and blade pitch angle. During the course of this master project it also became obvious that the data quality checks provided by the LiDAR manufacturer are not sufficient. The compilation of a reliable LiDAR dataset for the WINTWEX-W campaign, by a thorough re-examination of the raw measurements and the development and application of an advanced de-spiking routine, therefore became another important focus area.

The measurement principle of the pulsed LiDAR wind profiler and some basics of wind energy and ABL meteorology are presented in chapter 2. Chapter 3 describes the field experiment in Wieringermeer and the instrumentation used during the campaign. Further evaluation of the LiDAR measurements and the removal of bad quality data is presented in chapter 4. Site characterization, including changes in both wind speed and turbulence intensity with wind direction, and the overall distribution of wind speed and wind directions measured by the LiDARs and the sonic anemometers, are given in chapter 5. This chapter also presents a method for determining a proxy for the atmospheric stability during the campaign, based on a simple temperature difference measurements. Chapter 6 presents an analysis of the wake profiles of wind speed and turbulence intensity from one of the research wind turbines, and illustrates how the wake changes under different stability regimes.

The effect of pitch control on the corresponding profiles is discussed in chapter 7. A summary of the main results and an outlook are presented in the final chapter.

Chapter 2

Theory

In addition to briefly describing the wind's potential as an energy resource, an introduction to the atmospheric boundary layer and the most relevant parameters in boundary layer meteorology for wind power generation is given in the following chapter. Mean horizontal wind speed, turbulence and atmospheric stability are all essential when assessing wind energy potential and wind turbine operations. The measurement principle of this thesis's most crucial instrument, the LiDAR wind profiler, is also presented.

2.1 Extracting wind power

Extracting power from wind energy is based on drawing as much kinetic energy out of the air flow as possible. The potential of wind as a renewable energy resource is immense, and due to technological improvements power generated by wind is beginning to play a significant part in the world's energy budget.

2.1.1 Wind energy

For a given cross section A , the available kinetic wind energy is

$$E = \frac{1}{2}mv^2 = \frac{1}{2}\rho Av^3 \quad (2.1)$$

where m is the mass of air passing the cross section, ρ is the air density and v is the wind speed (Ehrlich, 2013). Presuming the cross section is a wind turbine's rotor swept area, the maximum available wind power for that turbine can be described as:

$$P = \frac{E}{t} = \frac{1}{2}\rho Av^3 \quad (2.2)$$

However, due to physical constraints only a fraction of this available wind power can be extracted. The efficiency of a wind turbine is described by the power coefficient (C_p), which depends on the turbines design and operation, and illustrates how much wind power the turbine is able to extract (Christakos, 2013). Consequently equation 2.2 can be rewritten as:

$$P = \frac{1}{2}\rho C_p Av^3 \quad (2.3)$$

The theoretical efficiency maximum is $16/27 = 59.3\%$ and is referred to as the Betz limit (Ehrlich, 2013).

The expected performance of a wind turbine is often displayed in the form of a power curve as a function of wind speed. The turbine will only start generating power for wind speeds exceeding the cut-in speed. Power generation will then continue to increase with wind speed until its maximum is reached at the so called rated wind speed. At higher wind speeds the power will then be limited to this maximum by reducing the turbine's efficiency, usually by changing the pitch angles of the blades. In order to avoid damage, the turbine will shut down for wind speeds larger than the cut-out speed, which is usually in the order of 25 m s^{-1} . A sketch of the power curve and the corresponding C_p is illustrated in figure 2.1 for the turbine type used in this study (NORDEX N80).

2.2 Atmospheric boundary layer

The lowest part of the troposphere is known as the atmospheric boundary layer (ABL). The earth's surface, serving as the lower boundary to the earth's atmosphere, will have an impact on the ABL. Stull (2003) defines the ABL as the

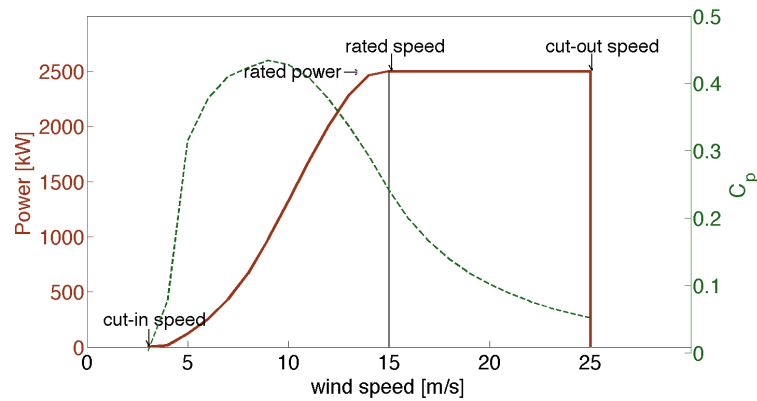


Figure 2.1: Powercurve and C_p as a function of wind speed. Based on properties of wind turbine NORDEX N80 (NORDEX, 2016).

part of the atmosphere which directly feels the presence of the ground, and will change in response to it within an hour. In addition to surface characteristics, synoptic weather conditions, seasons and the time of the day all have an impact on the ABL height, which may vary between a couple of hundreds of meters to a few kilometres (Stull, 2003). A temperature inversion indicates the top of the ABL and is during daytime called the entrainment zone (EZ), and the rest of the troposphere is referred to as the free atmosphere (Foken, 2008). The structure of the ABL over land is strongly dependent on the daily cycle. Figure 2.2 shows the diurnal evolution of the substructures in a daytime convective ABL. After sunrise the atmosphere is warmed by the earth's surface and creates a mixed convective layer, which is characterized by strong turbulent motion. Shortly before sunset the turbulence start to decay, resulting in a residual layer. Closer to the ground a thinner stable boundary layer develops due to the colder surface temperatures. Quickly after sunrise the convective mixed layer starts to develop once more. The lowest region of the ABL, where the turbulent fluxes are almost constant, is called the surface layer and exists throughout the day (Foken, 2008). The wind in the free atmosphere is approximately geostrophic, but when approaching the earth's surface the wind speed is greatly reduced due to the increase of frictional drag near the ground (Foken, 2008). A near logarithmic profile is established in the surface

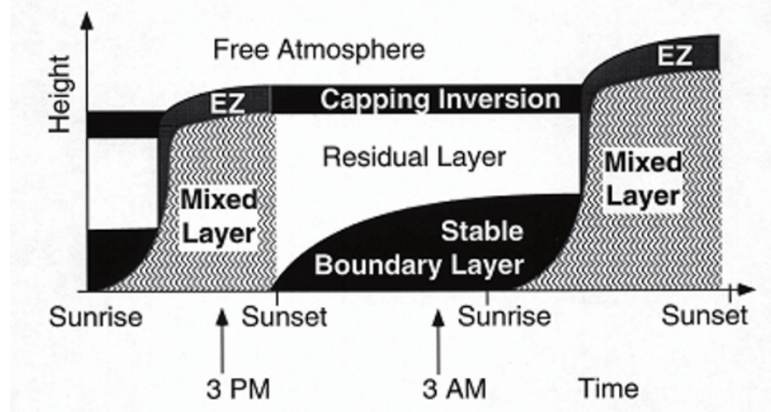


Figure 2.2: Diurnal evolution of the ABL substructures over land (Foken, 2008).

layer for neutral conditions. The profile can be described by equation 2.4 (e.g. Holton and Hakim, 2012). By integrating from the roughness length z_0 , the height at which $\bar{u} = 0$, to any height z , the mean wind at that height can be determined.

$$\frac{\partial \bar{U}}{\partial z} = \frac{u_*}{kz} \quad (2.4)$$

$k \approx 0.4$ is the von Karman constant and has been empirically determined. The parameter u_* is the friction velocity and is defined as $u_*^2 = [\overline{u'w_s'^2} + \overline{v'w_s'^2}]^{1/2}$. This relationship is, however, only suited for a neutral ABL. The wind profile's dependency on stability is explained further in section 2.2.2.1.

Due to the further turbine development of ever increasing hub height and rotor diameter, a wind profile description only valid and applicable for the atmospheric surface layer is no longer sufficient. New methods predicting accurate wind profiles up to a few hundred meters are therefore being established (e.g. Gryning et al., 2007).

2.2.1 Turbulence

Turbulence is characterized as stochastic fluctuations superimposed on the mean wind. Turbulence is highly diffusive and is therefore an effective mechanism for

the transport of atmospheric quantities and constituents (Stull, 2003). Strong turbulence increase loads and cause fatigue of wind turbines, however, a well mixed wind field helps to draw momentum into the wake region leading to quicker wake recovery (Barthelmie et al., 2013). Additionally, the turbine itself is inducing more turbulence both by the tower and the nacelle and, in particular, by the vortices created by the rotating blades (Alblas et al., 2014). Parameters describing the presence and strength of turbulence in the wind field are therefore important, not only in boundary layer meteorology, but also for wind energy applications.

2.2.1.1 Horizontal turbulence intensity

The most commonly used parameter in the wind energy community to characterize the turbulence level is the so called horizontal turbulence intensity (TI) (e.g. Barthelmie et al., 2013, Westerhellweg et al., 2013, Alblas et al., 2014, Kumer et al., 2015).

$$TI = \frac{\sigma_H}{U_H} \quad (2.5)$$

TI is the ratio of the standard deviation of the horizontal wind speed σ_H and its mean value U_H (e.g. Stull, 2003). For wind energy applications the corresponding averaging interval chosen is 10 minutes, and the wind speed is typically measured with 1 Hz temporal resolution.

2.2.1.2 Turbulent kinetic energy

The part of the kinetic energy of a flow that is associated with turbulent motion is called the turbulent kinetic energy (TKE) and is most often measured per unit mass. It is a direct measurement of the energy content of turbulence in all three dimensions of the wind field, and is given by equation 2.6 (e.g Stull, 2003).

$$\bar{e} = \frac{TKE}{m} = \frac{1}{2}(\overline{u'^2} + \overline{v'^2} + \overline{w'^2}) \quad (2.6)$$

Because TKE, in contrast to TI , also include the wind fluctuations in the vertical, it is a much better measure for the overall turbulence level, in particular in the high turbulence environment of a turbine wake.

2.2.2 Stability

The capability of vertical movement within an air column is linked to the atmospheric stability. Wind field stratification and turbulence are strongly connected to stability and serve as the main contributors of vertical motion. Based on the vertical temperature gradient, the atmosphere is classified as stable, neutral and unstable (e.g Holton and Hakim, 2012, Stull, 2003, Wallace and Hobbs, 2006). Neutral stability is a situation with a temperature gradient following the adiabatic lapse rate and without free convection. Atmospheric instability is generally characterized by a more turbulent wind field in addition to having a positive buoyancy flux, while the opposite is the case for a stable situation (Wallace and Hobbs, 2006). Convection caused by vertical density differences and mechanically generated turbulence are the bases of atmospheric instability. If low density air is overlying high density air, thereby inhibiting vertical motion, the atmosphere is said to be stable. This can, however, be overturned by mechanically generated turbulence (Stull, 2003). The traditional definition of stability is only based on local temperature changes with altitude. Comparing the surrounding lapse rate Γ with the adiabatic lapse rate Γ_a , is used to establish the stratification of the atmosphere (Holton and Hakim, 2012). The dry adiabatic lapse rate is $g/c_p \approx 10 * 10^{-3} Km^{-1}$ throughout the ABL, while the saturated adiabatic lapse rate is dependent on temperature and pressure (Wallace and Hobbs, 2006). The change in potential temperature with height can be related to the lapse rate, and using the same traditional definition this change can also be used to determine stability (Holton and Hakim, 2012). The lapse rate and potential temperature stability criteria can be seen in table 2.1.

However, determine the stability based on the local lapse rate alone is usually inadequate (Stull, 2003). A more reliable means of describing the stability is the heat flux, but the stabilities strong dependence on dynamically generated turbulence in addition to convection, may also leave this definition incomplete (Stull, 2003). Wind shear counteracts thermal stratification and can cause mixing in statically stable air, leading to dynamic instability. Two parameters often used to determine stability in boundary layer meteorology are the stability parameter

statically stable	$\Gamma_a > \Gamma$	$\frac{d\theta}{dz} > 0$
statically neutral	$\Gamma_a = \Gamma$	$\frac{d\theta}{dz} = 0$
statically unstable	$\Gamma_a < \Gamma$	$\frac{d\theta}{dz} < 0$

Table 2.1: Traditional stability conditions. Adapted from Holton and Hakim (2012).

and the Richardson number. The stability parameter, which sign indicate the atmospheric stability, can be written as

$$\zeta = \frac{z}{L} \quad (2.7)$$

where z is the altitude and L is the Obukhov length. A positive (negative) stability parameter represent stable (unstable) conditions, and the sign is mainly determined by the buoyancy flux (Foken, 2008). The Obukhov length represents the height where turbulence induced by buoyancy fluxes dominates over shear production and is given by equation 2.8 from Stull (2003)

$$L = \frac{-\overline{\theta}_v u_*^3}{kg \overline{(w'\theta'_v)_s}} \quad (2.8)$$

$\overline{(w'\theta'_v)_s}$ represents the kinematic temperature flux, k is the von Karman constant and u_* the friction velocity.

Another parameter to describe the dynamic stability and the transition between laminar and turbulent flow is the gradient Richardson number

$$Ri = \frac{\frac{g}{\theta_v} \frac{\partial \overline{\theta}_v}{\partial z}}{[(\frac{\partial \overline{U}}{\partial z})^2 + (\frac{\partial \overline{V}}{\partial z})^2]} \quad (2.9)$$

where θ_v is the virtual potential temperature and U and V are the longitudinal and latitudinal wind speed components, respectively (Stull, 2003).

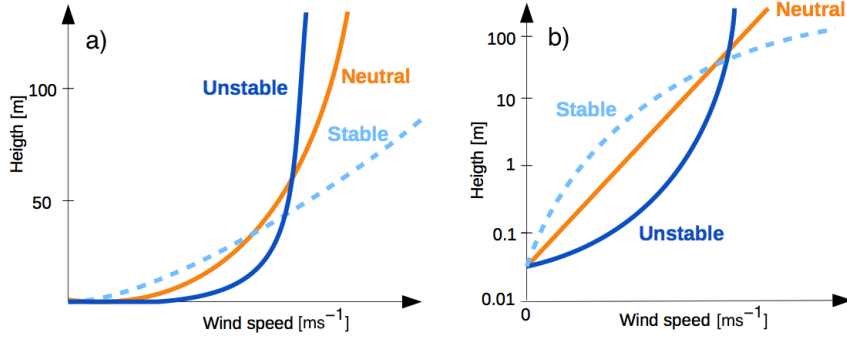


Figure 2.3: Wind speed profiles in the ABL for a stable, neutral and unstable situation. a) a linear and b) a semi-logarithmic plot. Adapted from Fig.9.17 by Wallace and Hobbs (2006).

2.2.2.1 Wind profile

The shape of the wind speed profile, which typically shows an increase with height, is strongly dependent on the atmospheric stability. The neutral wind profile, presented in section 2.2, can be extended by the Businger-Dyer relationships to include non neutral surface layer conditions. The relationships can be expressed as:

$$\begin{aligned}
 \phi_M &= 1 + \left(\frac{4.7z}{L} \right) && \text{for } \frac{z}{L} > 0 \quad (\text{stable}) \\
 \phi_M &= 1 && \text{for } \frac{z}{L} = 0 \quad (\text{neutral}) \\
 \phi_M &= \left[1 - \frac{15z}{L} \right]^{-1/4} && \text{for } \frac{z}{L} < 0 \quad (\text{unstable})
 \end{aligned} \tag{2.10}$$

where L is the Obukhov length, z is the height and ϕ_M is the dimensionless wind shear, which can be derived by dividing equation 2.4 by $u_*/(kz)$ (Stull, 2003).

All situations show an increase of wind speed with height. However, due to turbulent mixing the unstable profile has a more rapid increase of wind speed with height very close to the ground compared to the other stability regimes, before

it develops a more or less constant wind speed at higher altitudes (Wallace and Hobbs, 2006). Semi-logarithmic wind profiles in different stability conditions are presented in figure 2.3 b). The wind profile for neutral stability is then represented by a straight line, while the stable and unstable situations appear as concave and convex lines in the semi-logarithmic scale of figure 2.3 b).

2.3 LiDAR Measurement principles

Measurements done by LiDARs are remote sensing measurements based on an emitted laser pulse or beam, which gets backscattered by aerosol particles in the atmosphere. The returned signal is affected by the relative movement of the atmospheric particles, and will thus experience a shift in frequency. This so-called Doppler shift can be used to measure the average radial velocity of the particles in the instrument's line of sight. Assuming stationarity and homogeneity, subsequent measurements in different directions can be combined to determine the three dimensional wind vector (Peña et al., 2013).

2.3.1 Wind vector

Finding the height of the measurement of interest can easily be determined by accurate knowledge of the time difference between when the pulse starts and the time you receive the backscattered signal. A pulsed LiDAR sends out a short light beam, and the time of arrival t , of the backscattered signal will correspond to a given range z along the line of sight given by $z = c/t$, where c is the speed of light (Wagner, R & Courtney, 2010). Depending on the instrument's height configurations, measurements from the corresponding time period will be evaluated in order to derive the radial wind speed. The evaluated range gate, called the probed length, is determined by the length of the emitted pulse, and is 20 m for the Windcube V1 (Pauliac, 2009). Consequently, in order to find the radial wind speed at the desired height z , backscatter from $z \pm 10$ m along the line of sight is processed. The low power of the LiDAR's transmitted pulse makes it, however, necessary to accumulate and average approximately 10 000 pulses in order to get

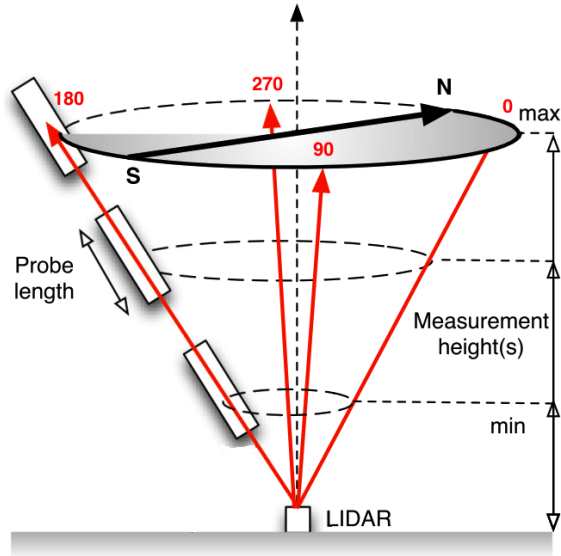


Figure 2.4: Sketch of the scanning pattern for the Windcube V1. Adapted from International Energy Agency (2013)

a good quality measurement (Pauliac, 2009). The backscattered signal is transformed into a power spectrum, and the wind speed at the middle of the range, which is the desired measurement height, is assumed to correspond to the peak in the power spectrum (Peña et al., 2013). The spectral broadening of the backscattered signal is dependent on the turbulence and wind shear of the ambient wind field (Wagner, R & Courtney, 2010).

Assuming that the aerosols in the atmosphere move with the wind, the radial velocity can be determined. In order to provide a three dimensional wind vector, three or more independent radial wind speed measurement at different azimuth angles are needed (International Energy Agency, 2013). This can be done either by moving the scanner (as is the case for Windcube V1), or by having several telescopes where only one is active at a time (the design for Windcube V2). The Windcube V1 measure the radial wind speed at four different locations, rotating the prism by 90° each time (Wagner, R & Courtney, 2010). Using the following equations (e.g. Christakos (2013)) the different components of the

three dimensional wind vector can be determined from the four radial wind speed measurements.

$$u = \frac{V_{r270} - V_{r90}}{2 \sin(\phi)} \quad (2.11)$$

$$v = \frac{V_{r180} - V_{r0}}{2 \sin(\phi)} \quad (2.12)$$

$$w = \frac{V_{r0} + V_{r90} + V_{r180} + V_{r270}}{4 \cos(\phi)} \quad (2.13)$$

The conical angle, ϕ , of the scan is around 30° for the Windcube V1 (Pauliac, 2009), and in order to calculate the wind vector it is necessary to assume homogeneous conditions along the horizontal plane within the cone. After the first four measurements the LiDAR will calculate the next wind vector by rotate the prism another 90° . By using this new radial velocity and the previous three, only a single new measurement is needed. Consequently the Windcube V1 is able to deliver data of the three dimensional wind speed with 1 second intervals, however it takes 4 seconds to derive a new fully independent wind reading.

2.3.2 Carrier to Noise Ratio

The carrier to noise ratio (CNR) measures the relative amount of noise that is present in a received signal, giving an indication of the signal strength, and the unit of measure is dB (Christakos, 2013). Setting the CNR limit gives the opportunity to select a suitable quality in the received signal. The pulse emitted from the Windcube V1 is focused at approximately 80 m, causing a peak in the CNR at this height (Wagner, R & Courtney, 2010). Due to backscattering, the strength of the received signal will decrease with height and set a limit for the maximum altitude at which the LiDAR can measure appropriately. LEOSPHERE recommend a CNR threshold of -22 dB for their Windcube V1, below which the measurements uncertainty is too large (Pauliac, 2009). It is also stated that the Windcube V1 has a range of 200 m, and thus has the possibility to give high quality measurements up to this altitude, depending on atmospheric conditions (Pauliac, 2009).

2.3.3 Benefits

The LiDAR has several advantages compared to other atmospheric measurement systems. The mobility of the LiDAR allows for more flexibility in positioning compared to a meteorological mast, which is usually a more permanent installation and costly to relocate. A LiDAR can also measure at several altitudes more, as one instrument measure multiple altitudes simultaneously. The LiDAR also reaches higher in the atmospheric boundary layer than most meteorological masts, accommodating the height of state of the art wind turbines (Peña et al., 2013).

2.3.4 Disadvantages

Horizontal homogeneity

In order to calculate the three dimensional wind velocity, assuming horizontal homogeneity within the horizontal plane of the cone angle is imperative. The prism rotates between 0° , 90° , 180° and 270° , and measure the radial wind speed around a circle. The circle's diameter depends on the measurement height (h) and is given by equation (2.14)

$$D = 2h \tan(\phi) \quad (2.14)$$

where ϕ is the cone angle. Working with measurements up to an altitude of 200 m altitude, will for the Windcube V1 result in an area of $41,548 \text{ m}^2$ and a diameter of more than 230 m, which will also be the maximum distance separating the radial wind speed measurements. Assuming horizontal homogeneity over areas of this size might be a limiting factor for the accuracy of the wind measurements in turbulent wind fields, in particular when the terrain is complex. (Wagner, R & Courtney, 2010)

Precipitation

Falling rain droplets also backscatter the laser light, and as their movement is a combination of wind speed and fall velocity of the droplet, the backscattered signal might be biased, causing errors particularly for the vertical wind speed (Intern-



Figure 2.5: Picture of Windcube V1 wiper. Adapted from Pauliac (2009)

tional Energy Agency, 2013). The fall speed of the rain droplets may be measured instead of the actual vertical velocity component, as seen in the study performed by Aitken et al. (2012). Precipitation can also affect the light transmission. When the LiDAR's window is obstructed by water, dust or other debris, the CNR drops. The Windcube V1 has the option to activate a wiper which will swipe the window clean in these cases, as seen in figure 2.5. However, when the wiper passes the window it might block the laser beam, causing irregular and unreliable measurements of the radial wind speed, and thereby also in the three dimensional wind vector.

Concentration of atmospheric particles

The LiDAR measurement principle is dependent on the presence of aerosol particles in the atmosphere using the small dust particles movement to find the wind vector, assuming the particles velocity and the wind velocity are one and the same. The strength of the measurement signal is strongly related to the aerosol concentration. A high concentration will result in a strong signal and thus a large CNR (International Energy Agency, 2013). The earth's surface is the main source of atmospheric particles and higher altitudes have therefore typically a lower particle concentration. Because the atmospheric boundary layer usually has a higher aerosol concentration than the free atmosphere, the majority of LiDAR wind measurements are done there (Stull, 2003). This thesis is focused on the lowest few

hundred of meters of the atmosphere, and the cases of too low aerosol concentration are therefore the result of other circumstances. The concentration of atmospheric particles is related to the origin and history of the air mass. Comparing e.g. maritime and continental air masses, the concentration is typically significantly higher for continental air. Other variations in the concentration of aerosols might be due to the presence of clouds or fog and the cleaning of the atmosphere by rain and snow. Clouds and fogs can disturb the light transmission, causing large errors in the wind estimations (International Energy Agency, 2013). The strong amount of reflection and absorption by the cloud can attenuate the beam to such a degree that the cloud becomes impenetrable. Getting measurements from altitudes beyond the cloud will then be impossible (Stull, 2003). Because the presence of aerosols, clouds and fog are determined by the surrounding atmosphere, the data availability from a LiDAR is strongly dependent on atmospheric conditions.

Chapter 3

Measurement Campaign and Instrumentation

Three pulsed LiDAR wind profilers (LEOSPHERE Windcube V1) were used in a seven months field experiment from November 2013 to the middle of May 2014. The campaign was a collaboration between the University of Bergen (UiB), Christian Michelsen Research (CMR) and the Energy Centre of the Netherlands (ECN), as part of the Norwegian Centre for Offshore Wind Energy (NORCOWE). The campaign was conducted at ECN's test site in Wieringermeer (Kumer et al., 2015). A short description of this site, the instruments used in the further analysis and the field experiment set-up is given in this chapter.

3.1 Test site location

Situated in the north-east of the province Noord-Holland, the Wieringermeer test site lays approximately 2 km west of the coast of lake IJsselmer. The site altitude is 5 m below sea level and the surroundings are mainly agricultural areas, causing only small distortions in the wind field. Even though the test site is characterized by flat terrain, there are a few obstacles that might be relevant for our analysis. The IJsselmer dike, other surrounding turbines, a row of trees, a farmhouse and the village of Kreilerood 1 km north of the site, may all cause small disturbances

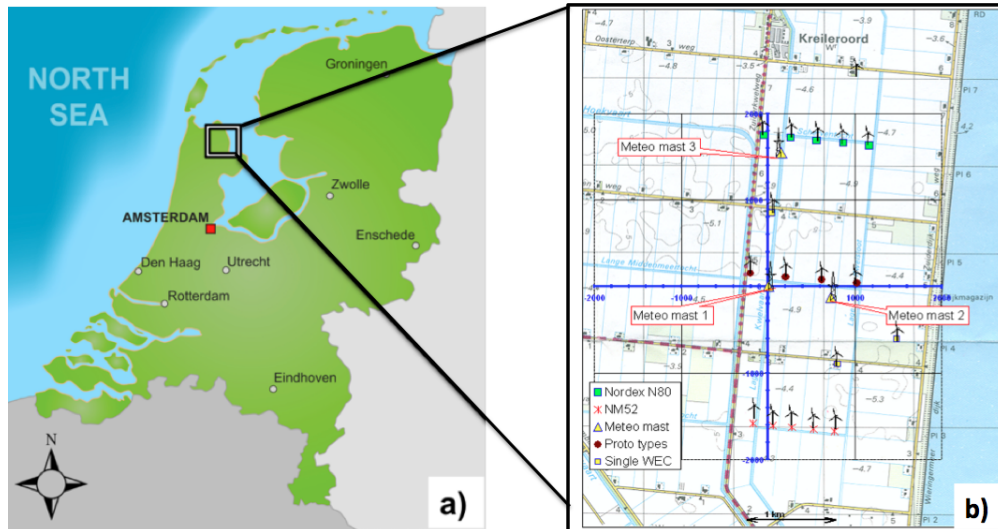


Figure 3.1: a) Map of Noord-Holland. b) A detailed sketch of the ECN test site in Wieringermeer. Adapted from Kumer et al. (2015).

in the wind field. A detailed description of the obstacles and their vicinity to the research wind farm is given in Eecen and Verhoef (2007).

The layout of the research farm is presented in figure 3.1 b). It consists of two main wind turbine rows, one southern row of four prototype turbines (numbered 1 to 4), and one row of five NORDEX research turbines (numbered 5 to 9) (Schepers et al., 2012). For this field campaign, the research turbines are the only ones under investigation, in particular wind turbine number 6 (WT6) from where we have detailed Supervisory Control And Data Acquisition (SCADA). With a hub height and a rotor diameter of 80 m, each research turbine has a rated power of 2.5 MW. They are aligned more or less East to West along a line of 95° – 275° with respect to North, and are separated by a distance of 3.8 rotor diameters (D) (Schepers et al., 2012). As shown in figure 3.1 b) the meteorological mast number 3 (MM3) is located South of the row of research turbines. With a height of 108 m, the met-mast measures both wind speed and direction at several altitudes and is situated 2.5 D South-West of WT6, i.e. upstream with respect to the main wind direction (Schepers et al., 2012).



Figure 3.2: The LEOSPHERE Windcube WLS-65 used during this campaign. Picture by Valerie-Marie Kumer.

3.2 Instrumentation

This study was mainly based on pulsed LiDAR measurements and their use for turbine wake analysis. In addition meteorological measurements from the met-mast in the vicinity and SCADA data from WT6 were evaluated. The following section presents all the instruments used in this thesis.

3.2.1 LiDAR

Three pulsed LiDAR wind profilers were deployed during this field experiment. The measurement principle is described in detail in section 2.3. The Windcube V1 LiDARs are produced by LEOSPHERE, and one of the LiDAR instruments used in the campaign is presented in figure 3.2.

3.2.2 Meteorological mast

The met-mast has three main measurement heights and their placement allows it to provide measurements at the hub height of WT6, as well as 28 m above and

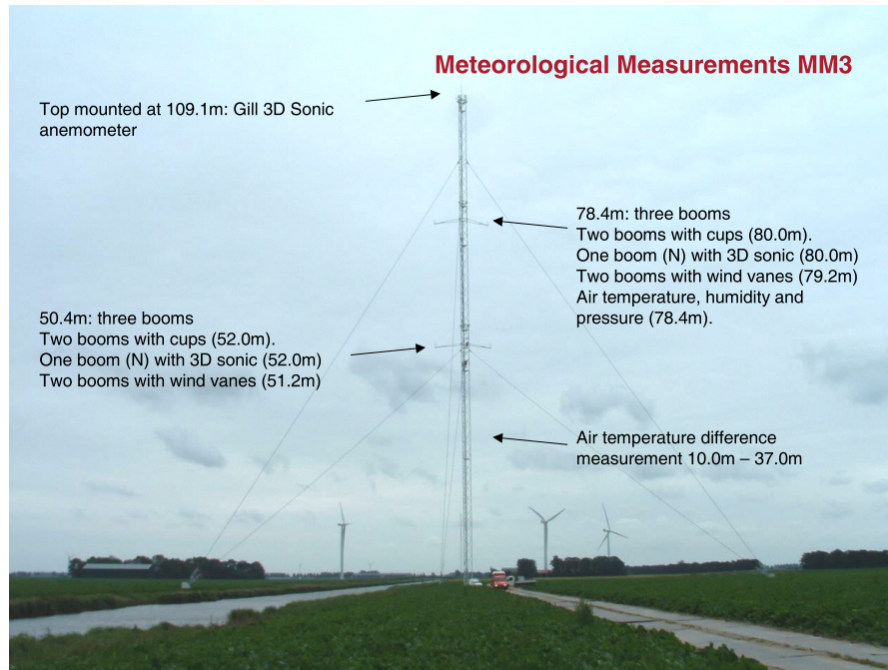


Figure 3.3: Photo of the meteorological mast 3 (MM3) with instrumentation, from Eecen and Verhoef (2007).

below. The instruments are placed on booms at 52 and 80 m, and at the top of the met-mast at 108 m, as can be seen in figure 3.3 (Eecen and Verhoef, 2007). Data used in this study are taken from the sonic anemometers at 80 and 108 m and from the temperature difference sensor measuring between 37 m and 10 m. Only 10 minute averaged statistical data from the met-mast was available for the further analysis.

3.2.2.1 Sonic anemometer

At 80 m a 3D Gill sonic anemometer is mounted on a triangular boom directed towards North, and at 108 m a 3D Gill sonic anemometer is located on the east mast pillar. A 5 m long lightning rod is situated on top of the south pillar, and causes some disturbance in the anemometer measurements from a South-West wind direction (Eecen and Verhoef, 2007) (see also Chapter 5).

3.2.2.2 Temperature difference sensor

The temperature difference between 37 and 10 m height is measured. The measuring unit is °C and the data will be used later on to determine atmospheric stability conditions.

3.2.3 Turbine measurements

Some key parameters of the NORDEX N80 turbine are given in table 3.1. Supervisory control and data acquisition has been made for research WT6. The SCADA measurements include 10 minute statistical data for blade pitch, turbine yaw error, generated power, generator speed, rotor speed, rotor position, nacelle wind speed and nacelle wind direction.

Properties	
Power	2500 kW
Number of blades	3
Rotor diameter	80 m
Hub height	80 m
Power regulation	pitch
Cut-in wind speed	3 ms^{-1}
Cut-out wind speed	25 ms^{-1}
Rated wind speed	15 ms^{-1}

Table 3.1: Key parameters of the NORDEX N80 turbine from NORDEX (2016).

3.3 Campaign set-up

The main object of this field experiment was to collect a comprehensive data set for single turbine wake investigations. As previously mentioned the met-mast's measurement instruments are placed at heights that correspond to WT6, and are located closer to this turbine than the others. Additionally, the dominate wind

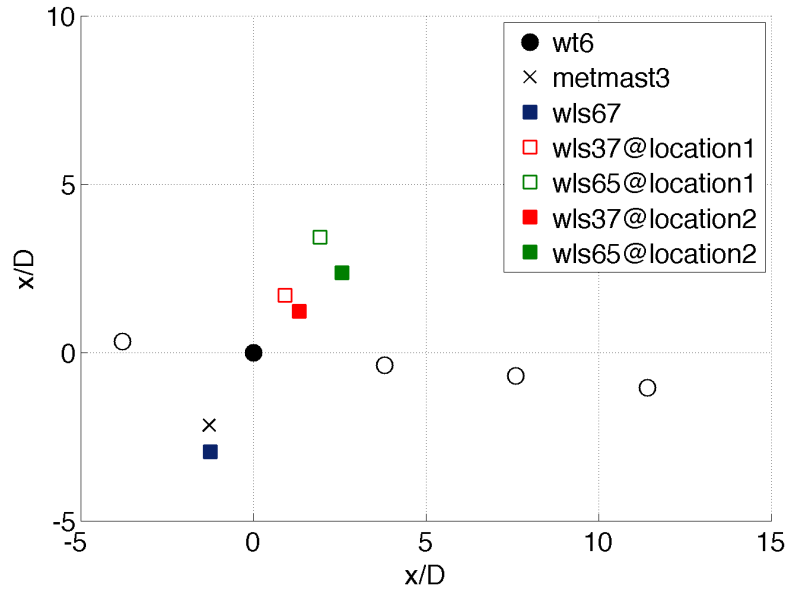


Figure 3.4: Measurement set-up around wind turbine 6 illustrating relative location and distance with respect to rotor diameter (D). Filled dots represent the second location of the instruments. Adapted from Kumer et al. (2015).

direction in the area is south-westerly, and the placement of the met-mast will thus give good upstream wind conditions for wake analysis of WT6 (Hu, 2015). Therefore it was natural to focus the single turbine wake measurements on this turbine. The selected positions of the downstream LiDARs allows them to measure in the wake of WT6 under prevailing wind conditions.

In addition to the permanent instrumentation on the meteorological mast, three Windcube V1s were also deployed, one upstream close to the met-mast and two downstream along the line of the main wind direction with respect to WT6. The devices, in the following named after their serial numbers WLS-67, WLS-37 and WLS-65, were respectively placed 3.2 D upstream, 1.9 D downstream and 3.9 D downstream, aligned along the wake line coming from 210° . On November 29th the downstream devices were relocated to 1.8 D and 3.49 D for wind coming from 227° . A sketch of the campaign set-up can be seen in figure 3.4. The static Li-

DARs measure the wind vector at several heights, creating vertical profiles at the three different locations. Originally, the height configurations were set differently for the three instruments, but on the 10th of December they were mutually reset to measure at 40, 52, 60, 80, 100, 108, 120, 140, 160 and 200 m, for both WLS-67, WLS-37 and WLS-65 (Kumer et al., 2015). Height and location configurations for the entire campaign are given in table 3.2. The LiDARs were sampling wind profiles with a temporal resolution of 1 Hz (Pauliac, 2009).

Instruments	Wake line from wt6		Rotor diameters from wt6		Height configurations [m]	
	Loc 1	Loc 2	Loc 1	Loc 2	Loc 1	Loc 2
WLS-67	210°	210°	3.2	3.2	40, 52, 60, 80, 100, 108, 140, 160, 200	40, 52, 60, 80, 100, 108, 140, 120, 160, 200
WLS-37	210°	227°	1.9	1.8	40, 52, 60, 80, 100, 108, 140, 120, 160, 200	40, 52, 60, 80, 100, 108, 140, 120, 160, 200
WLS-65	210°	227°	3.9	3.5	40, 52, 60, 80, 100, 108, 140, 120, 160, 200	40, 52, 60, 80, 100, 108, 140, 120, 160, 200

Table 3.2: Location and height configurations of the LiDARs throughout the campaign.

Chapter 4

Data Overview and Quality Control

Statistical data containing 10 minutes averaged mean, minimum, maximum and standard deviations were available from the meteorological mast's sonic anemometer at 80 m and 108 m height. SCADA data from WT6 were accessible in the same resolution and structure. As such, choosing the same temporal resolution for the LiDAR's seemed pertinent. LEOSPHERE's Windcube V1 already provides 10 minute averages of its measurements. Having a first look at this data, weekly time plots showed periods of abnormal and suspicious values for the LiDAR wind speed measurements. Large spikes, fluctuating over relative short time intervals, were detected, varying in magnitude and frequency of occurrence for the three different instrument. An example can be seen in figure 4.1, where enhanced wind speeds are clearly visible for WLS-65 for several days in week 47 (18.Nov.2013-24.Nov.2013), in addition to some large irregularities for WLS-67 at the beginning of November 19th. Consequently, advanced methods for the detection and removal of bad quality data had to be developed and applied to finally provide a reliable dataset for the further investigations.

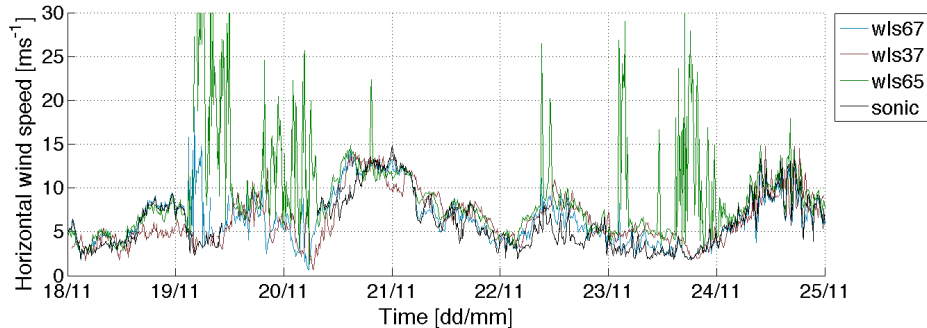


Figure 4.1: Weekly plot comparing horizontal wind speeds measured by WLS-67, WLS-37, WLS-65 and the sonic anemometer at 80 m height.

4.1 CNR and wipercount

The CNR threshold was originally set to -28 dB for the WLS-65, -23 dB for the WLS-67 and -22 dB for WLS-65. Noticing that the main errors in the instruments dataset were accompanied with a low CNR, a higher CNR threshold was chosen as a first approach. Following the recommendations from the Windcube V1 manufacturer LEOSPHERE, all measurements with a corresponding CNR of -22 dB or lower were discarded, regarding the quality to be inadequate. Figure 4.2 displays a time series of the 19th of November measured by WLS-65. The amount of low quality data is particularly bad for all three wind components, and clearly corresponds with a drop in the CNR level and an increase in the CNR variability.

The filtering removes a considerable portion, but not all, of the low quality data. Physical abnormalities in the measurements are generally associated with a wiper count, as seen in figure 4.2. The wiper count registers 1 every time the wiper swipes, and is activated by CNR values below a certain threshold. Choosing a rather conservative approach in the quality control, the periods ± 10 minutes of a wiper count has been excluded in this analysis in order to get a reliable dataset.

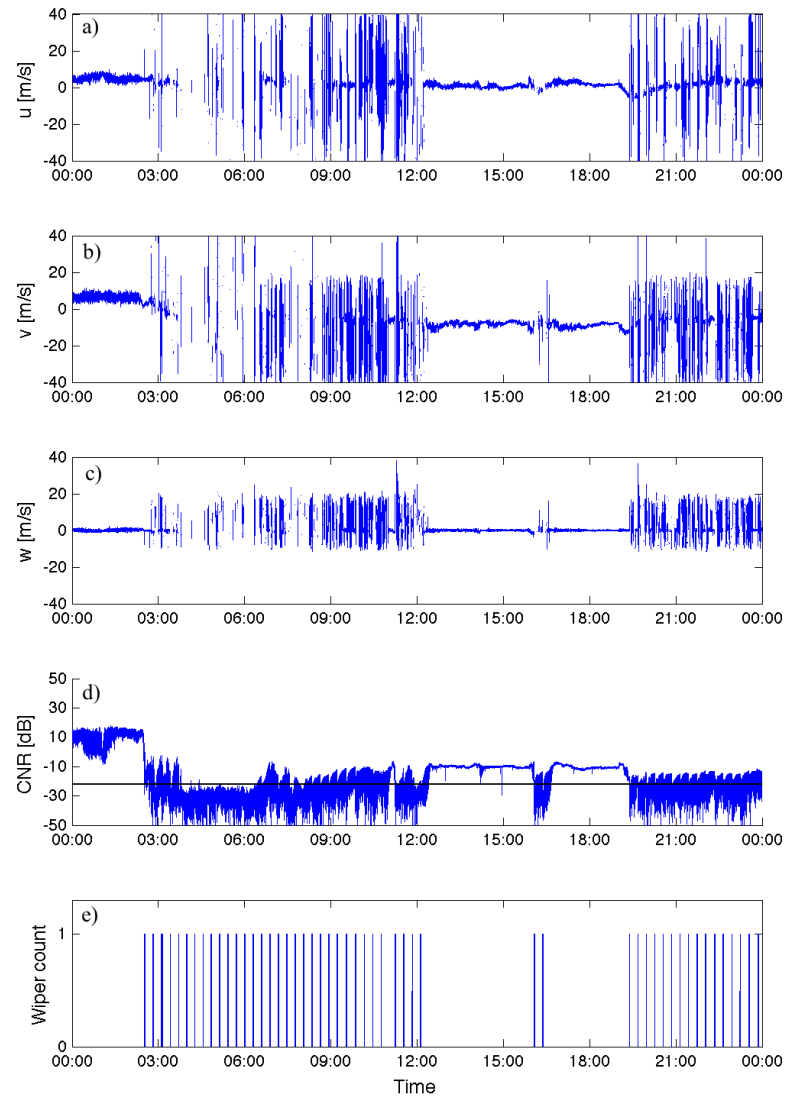


Figure 4.2: Daily plot for measurements from WLS-65 on the 19th of November at hub height. a), b) and c) show the three wind components. d) is the CNR with the CNR threshold of -22 dB represented by the black line and e) is the wiper count.

4.2 De-spiking

In order to get rid of remaining irregularities, a de-spiking routine has been developed and applied. By block averaging and using the standard deviation as a threshold, the final spikes in the dataset were detected and removed. Necessary input parameters for the de-spiking routine are the averaging interval, the standard deviation threshold, the number of repetitions of the de-spike algorithm, and the number of consecutive deviating data points that will be detected as spikes. After experimental evaluations of the different variables, I arrived at the following parameters for this data set, which were chosen for the final data processing. The block averaging was done over 15 minute intervals, which correspond to 900 measurements. The de-spiking routine was carried out four times using a standard deviation threshold of 4 for each run, i.e. all points outside a 4 standard deviation interval around the mean were discarded. In order to not mark certain physical event as spikes the routine implemented a threshold for consecutive deviating data points. More than 15 detected irregular measurements in a row were therefore not considered to be a spike any longer. An example of the effect of the de-spiking routing applied to measurements taken from the WLS-67 is shown in figure 4.3.

4.3 Final LiDAR dataset

For the further analysis a dataset on 10 minute basis has been derived from the quality controlled 1 second data. It consists of mean, standard deviation, maximum and minimum of all three wind components in addition to the horizontal wind speed, wind direction, TI, TKE, mean kinetic energy and total kinetic energy. Even though the LiDAR delivers measurements of 1 second intervals, only every fourth measurement was included in calculating the averages. For further studies of energy spectra, it is important to have independent measurements. The LiDAR principle of using three previous measurements in combination with a single new one to find the wind vector, as described in section 2.3, can cause an overestimated

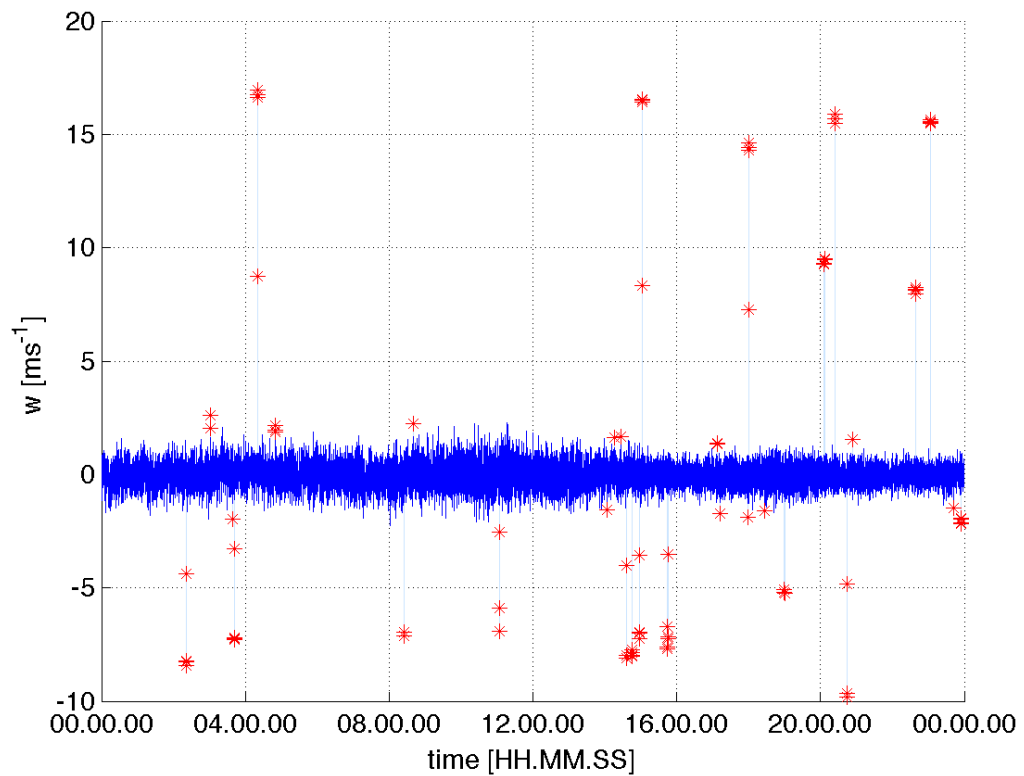


Figure 4.3: The bright blue line shows the vertical wind speed after de-spiking and the transparent blue line represent the data before. Red stars indicate the spikes. This is a daily plot of the vertical wind speed for WLS-67 on January 28th at 40 m altitude.

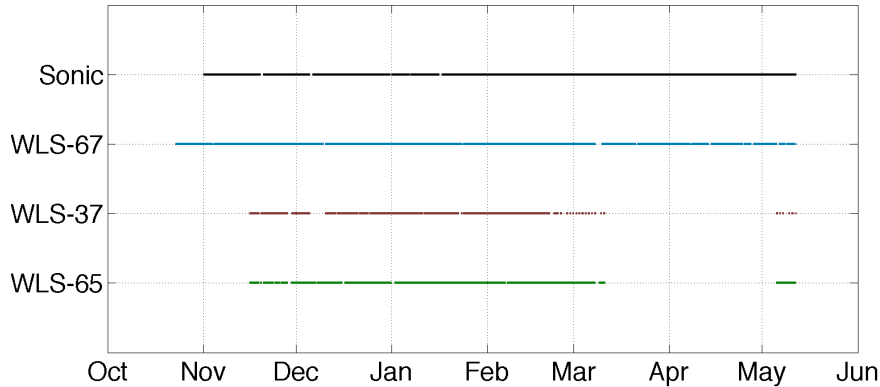


Figure 4.4: Data availability for the Windcubes WLS-65 (green), WLS-37 (red), WLS-67 (blue) and for the sonic anemometer (black) at 80 meter height.

turbulence (Kumer, 2016). It is in order to avoid this overestimation, and to get a fully independent data set, that only every fourth measurement is taken into account.

4.4 Data availability

Data availability is the ratio of the amount of measurements taken compared to the amount of measurements that were theoretically possible (Wagner, R & Courtney, 2010). The availability of measurements during the entire campaign is presented in figure 4.4. The larger gaps for WLS-37 and WLS-65 at the end of November and the smaller gaps in the beginning of December are caused by the instruments relocation on November 29th and the height configuration changes on December 10th, respectively. Farm work conducted North of the research wind turbines is the cause of the main gap in WLS-37 and WLS-65 measurements, and is why there is no data available from the middle of March to the beginning of May. Additionally, in WLS-37 measurements for the last three weeks, approximately half of every day was lost due unknown reasons. Low quality data, identified by the de-spiking algorithm, is the source of other minor discontinuities in the LiDAR time series.

Chapter 5

Site Characterization

Before investigating the single turbine wake of WT6 in more detail, a thorough site characterization had to be performed. It is presented in this chapter together with a method of determining a reliable stability classification from just a temperature difference measurement. At the end of the chapter the main characteristics of the wind conditions during the campaign are summarized.

5.1 Characterizing structure disturbances

An overall display of the most important measurement parameters has been made and separated into weekly time series. An example is shown in figure 5.1 and figure 5.2, while the remaining weeks can be found in appendix A. Even though the Wieringemeer test site is situated on a low lying agricultural area, obstacles, like the surrounding wind turbines and the meteorological mast, will influence the wind measurements. Having a first look at the weekly times series there is e.g. a significant drop in the sonic wind speed measurements whenever the wind direction approximates 180° . In addition the wind speed measurements are also substantially decreased for WLS-65 and WLS-67 in proximity to the wake line of WT6 at 227° . Table 5.1 shows at which wind directions the different measurement instruments are influenced by any particular object and the corresponding distance between them.

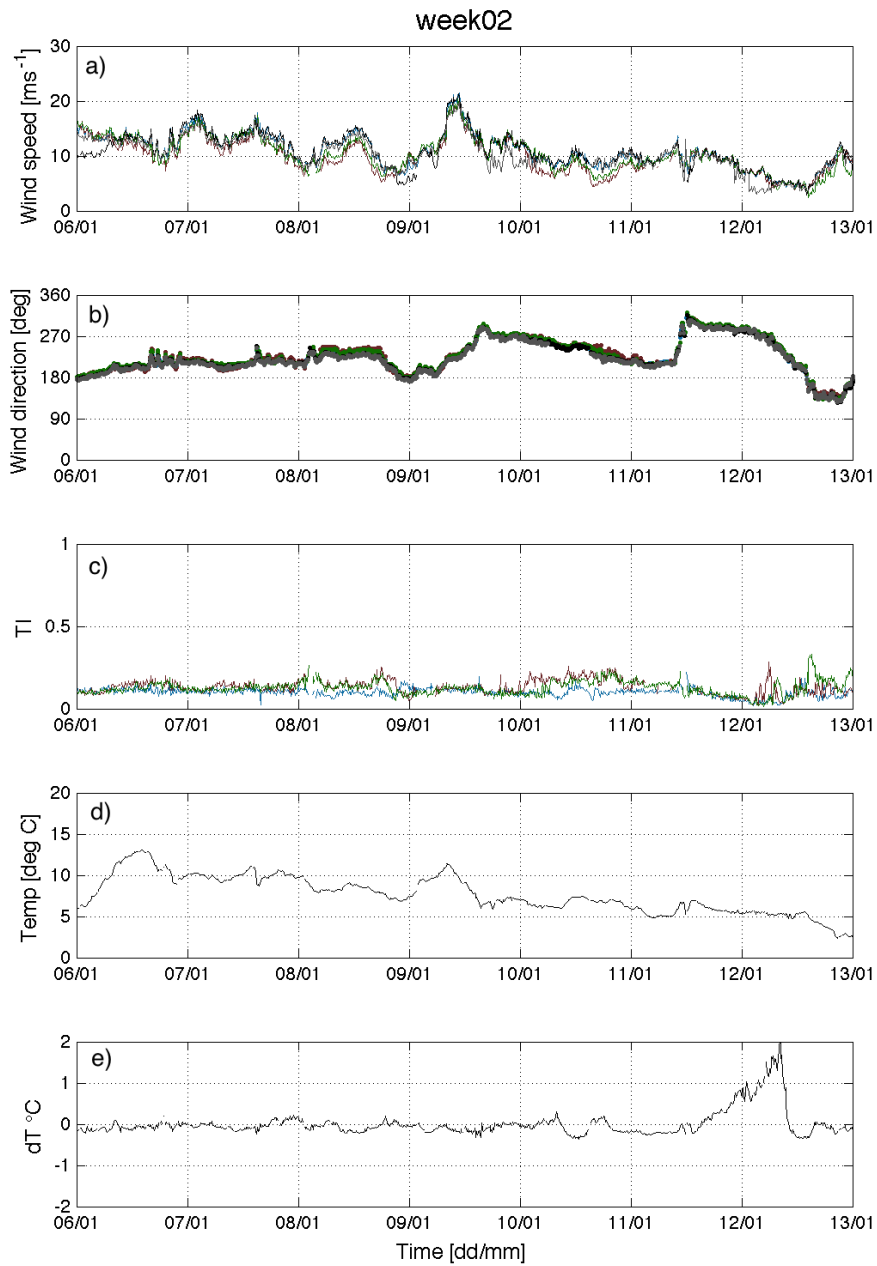


Figure 5.1: Plot of wind speed, wind direction, turbulence intensity, temperature at 80 m and temperature difference between 37 and 10 m height for week 2 (06.Jan.2014-12.Jan.2014). WLS-67 (blue) WLS-37 (red), WLS-65 (green), sonic anemometer (black) and WT6 (grey).

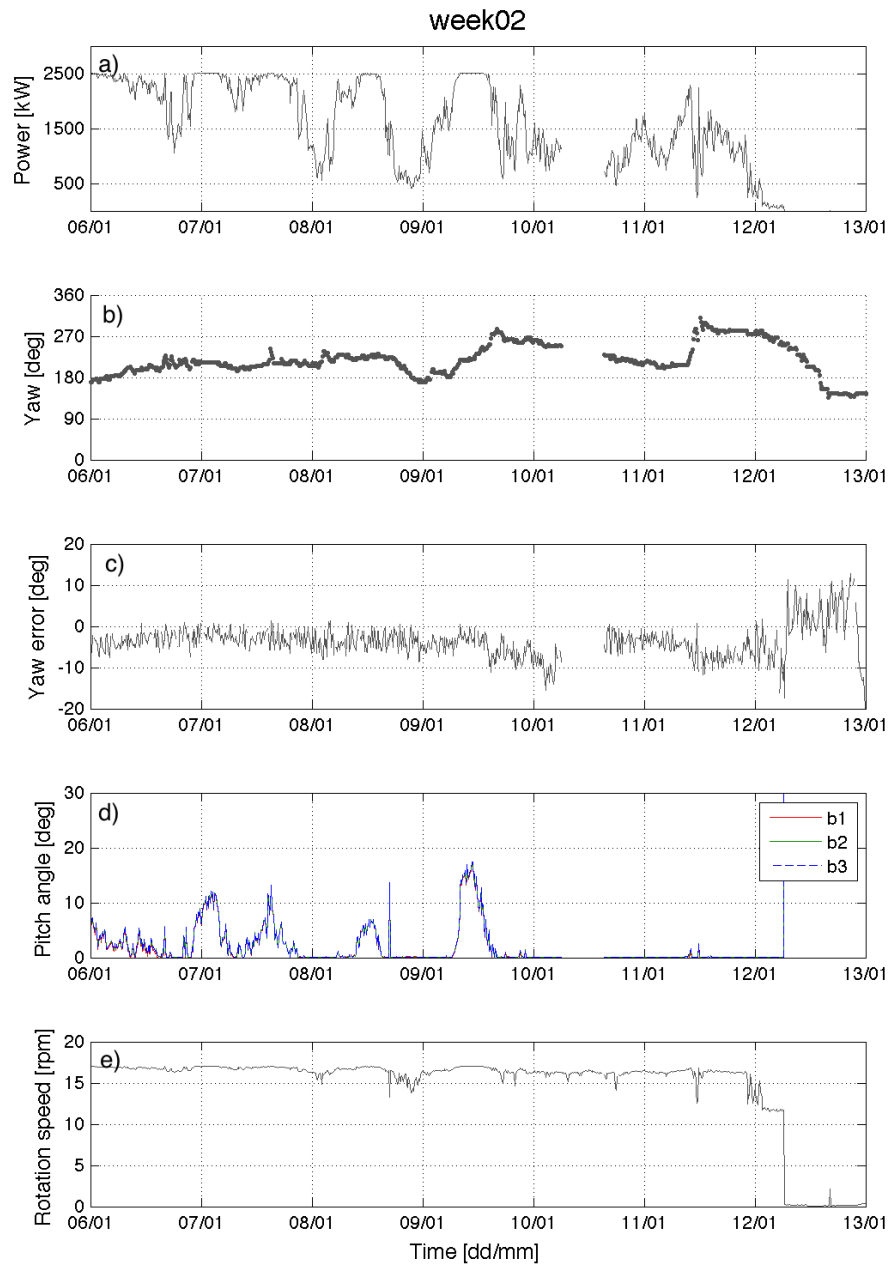


Figure 5.2: Plot of a) power output, b) yaw angle, c) yaw error, d) blade pitch angle and e) rotational speed measurements from WT6 for week 2 (06.Jan.2014-12.Jan.2014).

Instrument	Shadow	Distance [D]	Direction [°]	
M3	M3 shadow	0	180	
	WT5	3.5	315	
	WT6	2.5	31	
	WT7	5.4	71	
	WT8	9.0	81	
	WT9	12.7	85	
V1-067	M3	0.8	357	
	WT5	4.2	322	
	WT6	3.2	23	
	WT7	5.7	63	
	WT8	9.1	76	
	WT9	12.8	81	
V1-037	Loc 1	WT 5	4.9	254
		WT6	1.9	209
		WT7	3.6	126
		WT8	7.1	110
		WT9	10.8	105
	Loc 2	WT 5	5.2	260
		WT6	1.8	228
		WT7	2.9	123
		WT8	6.6	107
		WT9	10.3	103
V1-065	Loc 1	WT 5	6.5	242
		WT6	3.9	209
		WT7	4.2	154
		WT8	7.0	126
		WT9	10.5	115
	Loc 2	WT 5	6.7	252
		WT6	3.5	227
		WT7	3.0	156
		WT8	5.9	121
		WT9	9.5	111

Table 5.1: Wind direction and distance given in rotor diameter [D].

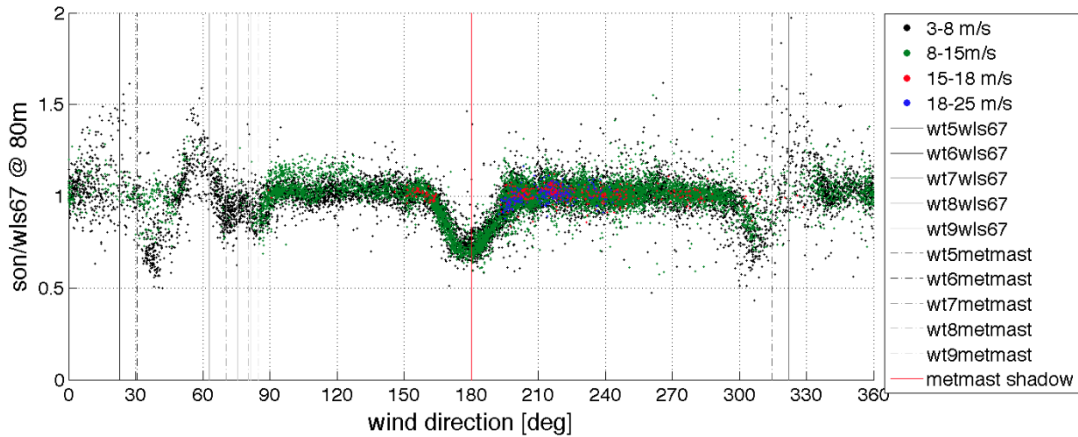


Figure 5.3: Wind speed ratio between sonic and WLS-67 measurements at hub height. Measurements are separated into wind speed intervals: $3\text{-}8\text{ m/s}$ (black), $8\text{-}15\text{ m/s}$ (green), $15\text{-}18\text{ m/s}$ (red) and $18\text{-}25\text{ m/s}$ (blue).

5.1.1 Effects on horizontal wind speed

The wake region of a wind turbine or of a support structure like a mast, is characterized by a reduction in wind speed. How much the wind speed decreases is strongly dependent on the distance from the object as illustrated in this section. Looking at figures displaying wind speeds measured at one location relative to measurements at another, can easily illustrate the complexity in the wind field at that location caused by various disturbances. The main distortions discussed here are caused by the met-mast and the adjacent research wind turbines.

5.1.1.1 Upstream instruments

A comparison between the WLS-67 and the sonic anemometer, both located upstream of WT6 in the prevailing wind direction, shows how much the wind field can alter, even for instrumentation as closely located as these upstream devices are. Only separated by a distance of approximately 60 m, there are large variations in the wind speed ratio between the sonic anemometer and the WLS-67 (figure 5.3).

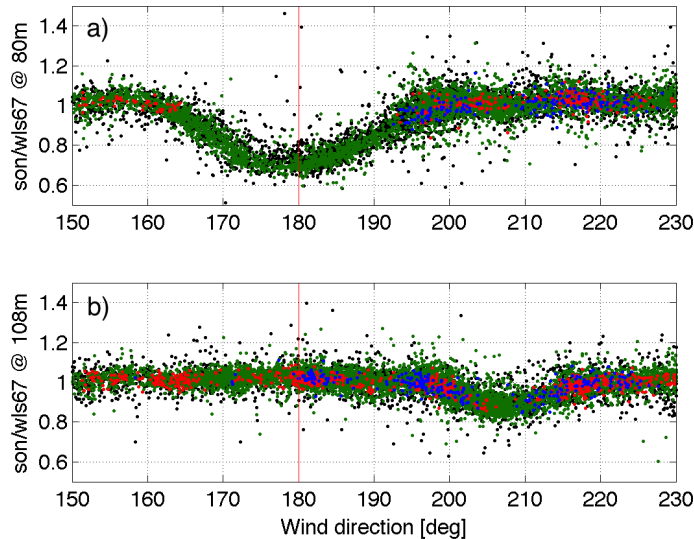


Figure 5.4: Wind speed ratio between sonic anemometer and WLS-67 measurements for wind directions $150^{\circ} - 250^{\circ}$. Measurements are separated into wind speed intervals: $3-8 \text{ m s}^{-1}$ (black), $8-15 \text{ m s}^{-1}$ (green), $15-18 \text{ m s}^{-1}$ (red) and $18-25 \text{ m s}^{-1}$ (blue). Measurements from 80 m is shown in a) and 108 m in b).

The vertical lines indicate wake lines of different structures as viewed from the sonic anemometer (solid lines), and the WLS-67 (dashed lines). The ratio, mostly varying between 0.5 and 1.5, seems to follow the wake lines, but its drop is distinctly more enhanced in the met-mast shadow of the sonic anemometer than for any of the wind turbine wakes. At 80 m height the sonic anemometer is placed at the tip of a 6.5 m long boom facing North (Eecen and Verhoef, 2007). Consequently, southerly winds will be blocked by the met-mast structure. As illustrated in figure 5.4 a), even though the met-mast is only 1.6 m wide, the close proximity to the sonic anemometer results in a decrease in wind speed of up to 40%, and the wake spans over approximately 40° , from $160^{\circ} - 200^{\circ}$. The vertical red line indicates the center of the met-mast shadow.

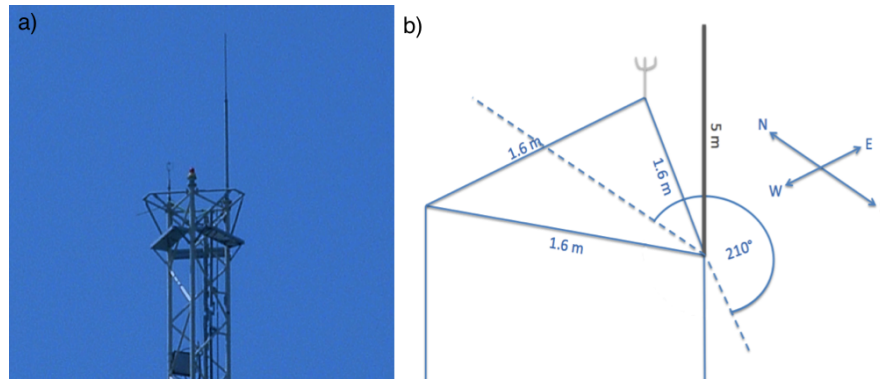


Figure 5.5: a) picture of the lightning conductor on top of the met-mast (Eecen and Verhoef, 2007) and b) a schematic picture of the incoming flow disturbed by the rod.

One would, however, expect that the instrumentation placed on top of the 108 m met-mast would not be the subject of flow distortion caused by the mast, but that is not the case. Mounted at the top of the meteorological mast is a 5 m long lightning conductor. Placed on the southern mast pillar it influences the sonic anemometer mounted on the eastern mast pillar for flow from South-Southwest. The meteorological mast is an equilateral triangle of 1.6 m side length, and as shown in figure 5.5 b) the angle from which the lightning conductor blocks the sonic anemometer is around 210° . Figure 5.4 b) shows how even a small and slender object, like the lightning rod of 22 mm diameter, can have a substantial impact on the wind measurements, reducing the wind speed by up to 20% compared to wind speed measurements from the LiDAR WLS-67 at the same direction.

The wind direction most relevant for further investigations of the wake of WT6 is in the region of 207° to 247° . Figure 5.3 shows that these wind directions are relatively free from disturbances for both the sonic anemometer located on the met-mast and the WLS-67. As such the two devices can be assumed to provide undisturbed measurements for upstream inflow conditions.

5.1.1.2 Downstream instruments

For the downstream LiDARs the research wind turbines are the main cause of flow distortions. The met-mast is located in the shadow of WT6 when viewed from WLS-37 and WLS-65, and its effect is therefore obscured by the wind turbine wake. Due to the relocation of the two downstream instruments, it is necessary to divide the measurements into two separate time series when analysing the wakes, as they shift several degrees after the relocation. Unfortunately the small dataset available for the first location for WLS-37 and WLS-65 does not give a full overview over all wind directions and has therefore not been presented separately here. Figure 5.6 a) displays the ratio of WLS-37 to WLS-67 after the relocation of the instruments. Due to the superposition of the wakes from wind turbine number 7, 8 and 9, the decrease in wind speed is almost as large in this wind direction section (90° to 140°) as it is for WT6, even though the proximity to WT6 is closer. For low wind velocities there is a reduction of over 50%, but the wake effect weakens as the wind speed increases. Wind turbine 5, which is more than 5 rotor diameters from WLS-37, also has a visible wake, reducing the wind speed by more than 20%. A comparison of wind speed measurements from WLS-65 and WLS-67 is shown in figure 5.6 b). The loss in momentum is considerably less than for WLS-37, but still exceeds 40%. As seen in table 5.1 the distance between WLS-65 and WT6 and wind turbine number 7 are relatively similar, being respectively 3.5 D and 3.0 D, and consequently the wind speed reduction is also fairly similar. There is also a small indication of a wake from wind turbine 5 (250° to 270°), which is more than 6 rotor diameters from WLS-65.

5.1.2 Effects on horizontal turbulence intensity

Similarly to the wind speed ratio plots the horizontal turbulence intensity (TI) can be an indicator of flow disturbance. The increase in turbulent motion in the wake is clearly visible in all four measurement instruments (figure 5.7). Higher wind speeds tend to have a lower TI , and the increase in TI in the wake regions is substantially larger for lower wind speeds. For wind speed exceeding 15 ms^{-1}

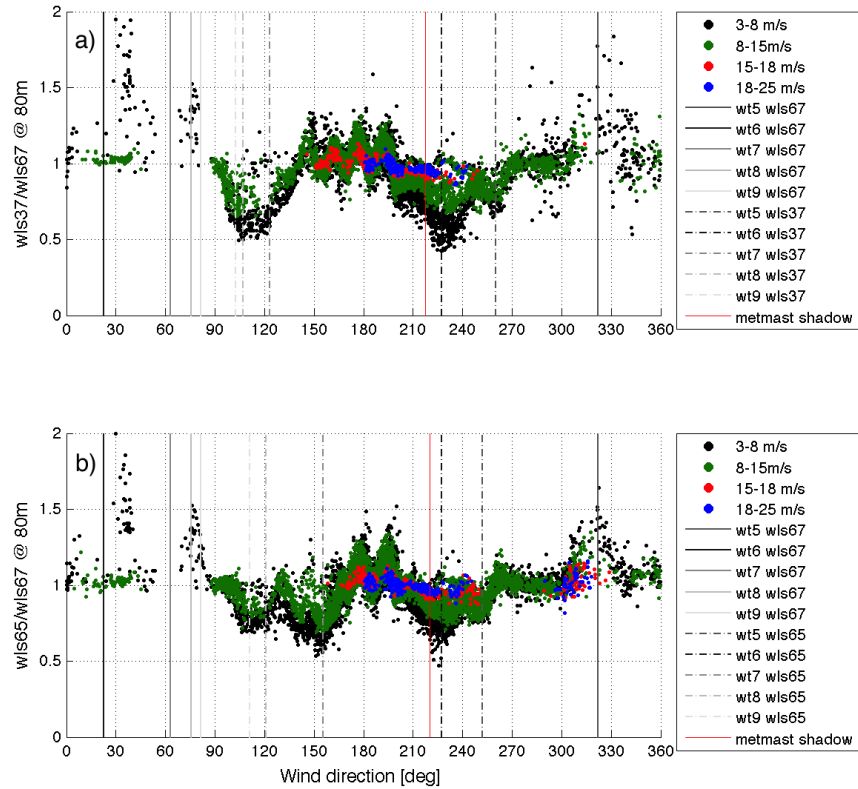


Figure 5.6: Wind speed ratio of a) WLS-37 and b) WLS-65 over WLS-67 at 80 m height, for all wind direction. The direction at which the measurement instruments are in the shadow of an object is indicated by vertical lines. Solid lines show when WLS-67 is in shadow while dashed lines represents a) WLS-37 and b) WLS-65. Measurements are separated into four wind speed intervals: $3-8 \text{ m s}^{-1}$ (black), $8-15 \text{ m s}^{-1}$ (green), $15-18 \text{ m s}^{-1}$ (red) and $18-25 \text{ m s}^{-1}$ (blue).

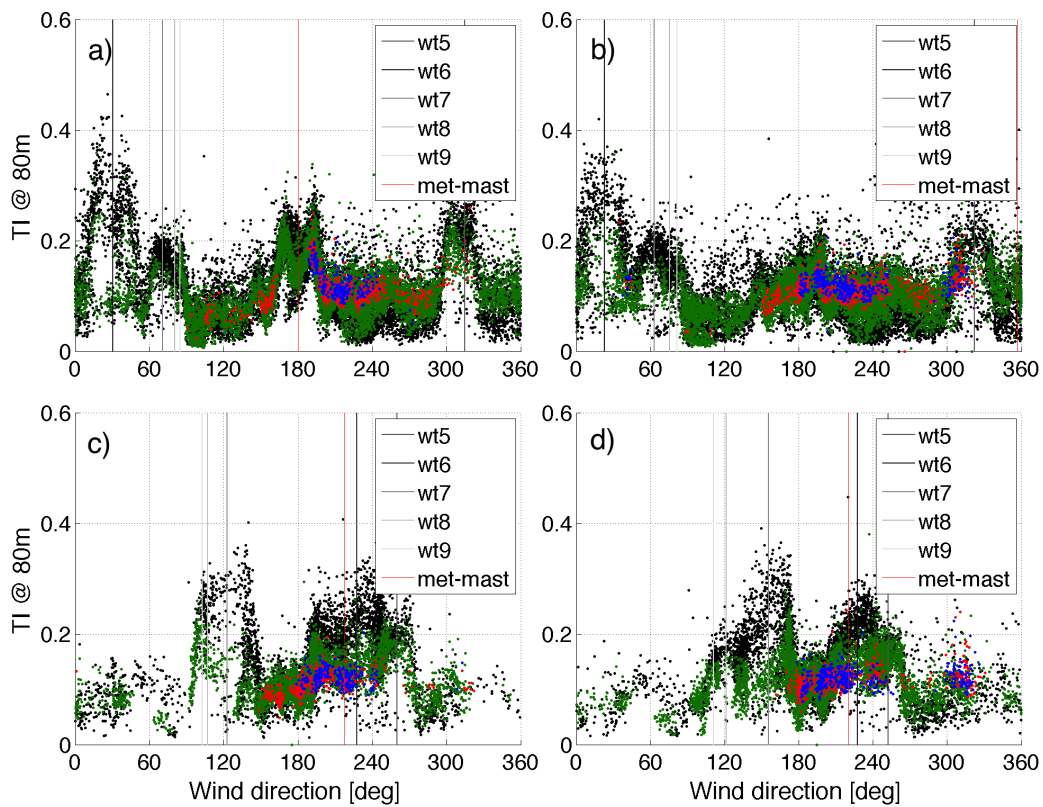


Figure 5.7: Horizontal turbulence intensity at 80 m altitude over the entire campaign for the a) sonic anemometer and b) WLS-67 and after relocation for c) WLS-37 and d) WLS-65. Vertical lines indicate the wake center. Measurements are separated into four wind speed intervals: $3\text{--}8\text{ m s}^{-1}$ (black), $8\text{--}15\text{ m s}^{-1}$ (green), $15\text{--}18\text{ m s}^{-1}$ (red) and $18\text{--}25\text{ m s}^{-1}$ (blue).

TI measurements from WLS-37 and WLS-65 show hardly any elevation in the wake regions, as illustrated in figure 5.7 c) and d). Lower wind speeds however experience an added increase in TI of 10% or more in wake regions.

5.2 Estimations of atmospheric stability

5.2.1 Finding stability criteria

In the absence of appropriate measurements the most common stability parameters can not be calculated. The only available information from the site is a temperature difference measurement between 37 m and 10 m. Due to the lack of wind speed measurements at the same height as the temperature difference the Richardson number cannot be estimated. Equation 2.8 show that the heat flux is needed to calculate the Obukhov length. Only 10 minute mean temperature measurements were available, making it impossible to calculate the covariances and thus also the Obukhov length, required to determine the stability parameter z/L . The only means to estimate the atmospheric stability is thereby the temperature difference with height.

Assuming a dry adiabatic laps rate, and using the traditional stability definition described in section 2.2.2, the local change in temperature over a 27 meter height interval should under neutral conditions result in a temperature difference of $-0.27K$. A first trial using this assumption and just the raw data of this measured parameter resulted, however, in suspicious results with respect to the frequency distribution of the occurrence of the different stability classes. This indicate a calibration issue of the temperature difference measurements. To establish a more reliable stability classification based on the available data set, an additional investigation has been preformed. The adiabatic laps rate for the temperature difference sensor was therefore found empirically by selecting neutral conditions where the change in temperature with height should equal the adiabatic laps rate. Filtering the dataset for night time conditions with high wind speeds will represent neutral stability in both clear and overcast situations. Table 5.2 shows the results of a

corresponding analysis of the local temperature change at night for different wind speed regimes.

Night and strong wind				
	samples	mean	median	std
$>10 \text{ m s}^{-1}$	2107	-0.060	-0.077	0.126
$>15 \text{ m s}^{-1}$	332	-0.042	-0.047	0.067
$>20 \text{ m s}^{-1}$	31	-0.059	-0.07	0.045

Table 5.2: Number of samples and mean, median and standard deviation for wind speeds exceeding 10 m s^{-1} , 15 m s^{-1} and 20 m s^{-1} during night.

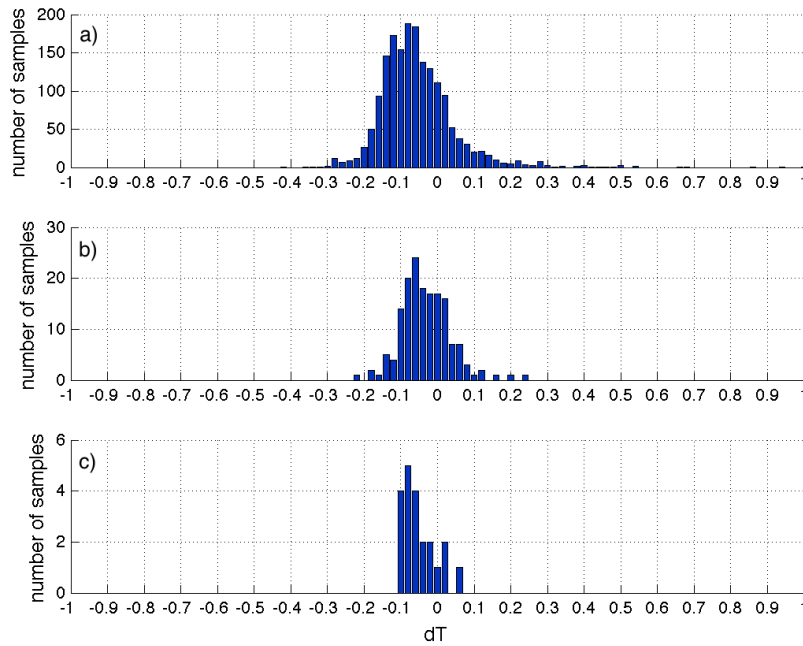


Figure 5.8: Histogram of the temperature difference over 27 meters for wind speed larger than a) 10 m s^{-1} , b) 15 m s^{-1} and c) 20 m s^{-1} during night.

Figure 5.8 shows how the temperature measurements are distributed for the three different scenarios. The slight skew to the right is why the median has a somewhat lower value than the mean, and this is clearly most noticeable for wind speeds exceeding 20 m s^{-1} . However, all the results, both in mean and median, give a lower adiabatic temperature difference than theoretically expected by the dry adiabatic lapse rate. Consequently, a new neutral stability criteria has been defined. The new stability limits based on the dataset from this campaign are shown in table 5.3.

	$\Delta T[\text{K}]$	Share of data [%]
Stable	> -0.01	35%
Neutral	≤ -0.01 and ≥ -0.11	17%
Unstable	< -0.11	49%

Table 5.3: Stability criteria derived from the temperature difference measurement during the campaign.

5.2.2 Stability distribution

Illustrated in figure 5.9 is the distribution of the resulting stability for different wind directions displayed as a wind rose. Except from a slight surplus of stable conditions for north-westerly winds, the majority fraction of the other sectors is neutral to convective. The different wind speed distribution for the three stability classes are shown in figure 5.10. Neutral conditions clearly contain the most high wind speed events and have a peak shifted further to the right than both stable and unstable conditions. The wind measurements used to describe the stability distribution are combined measurements from the three deployed Windcube V1 LiDARs. The reason for combining the measurements and the method used are explained in the next section.

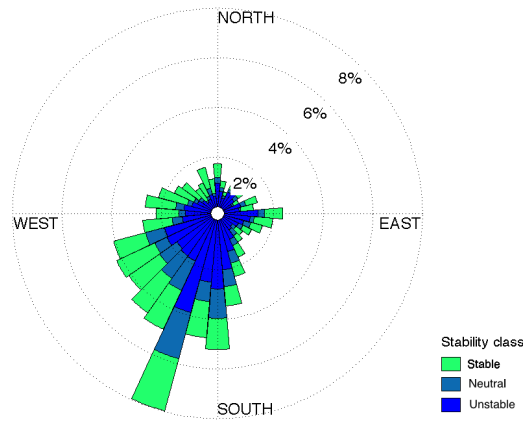


Figure 5.9: Overall wind direction distribution of the different stability classes.

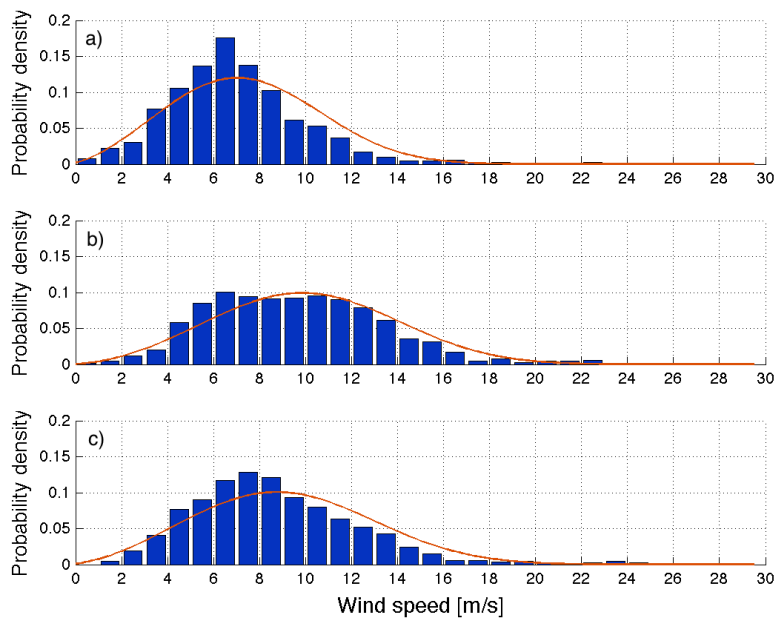


Figure 5.10: Histogram of horizontal wind speed at 80 m and a fitted Weibull distribution (red lines) for a) stable, b) neutral and c) unstable conditions.

5.3 Wind distribution throughout the campaign

When analysing the distribution of wind speed and wind direction for a test site looking at wind measurements undisturbed by surrounding obstacles will be beneficial compared to met-mast measurements alone, which will always experience some distortion because of the structure of the mast. In an attempt to get undisturbed wind data from the campaign, wind speed measurements for wind directions North of the row of research wind turbines were taken from WLS-65, and the WLS-67 was used for southerly winds. However since there were two LiDARs situated North of the research turbines, missing measurements from the WLS-65 were substituted with WLS-37 whenever possible. Both data from the sonic anemometer and the combined wind measurements from the Windcube V1s are presented in the following sections.

5.3.1 Horizontal wind speed

Horizontal wind speed is an important parameter in calculating several wind power variables like power generation and fatigue load. The wind speed follows a regular pattern over a longer period, and in the lack of wind measurements a wind speed probability distribution can be useful to estimate the power production (Ehrlich, 2013). A probability distribution that is normally used to resemble the wind speed is the Weibull distribution (Christakos, 2013). It is used to statistically describe any distribution with a single maximum that approach zero as the variable grows small or large, and with appropriate shape and scale parameters the distribution can be used to approximate any variable (Ehrlich, 2013). The Weibull distribution can be written as

$$f(s, u_0, U) = \frac{s}{u_0} \left(\frac{U}{u_0} \right)^{s-1} e^{(-U/u_0)^s} \quad (5.1)$$

where U is the horizontal wind speed, s is the shape parameter and u_0 is the scale parameter, all of which vary with location (Ehrlich, 2013). Overall his-

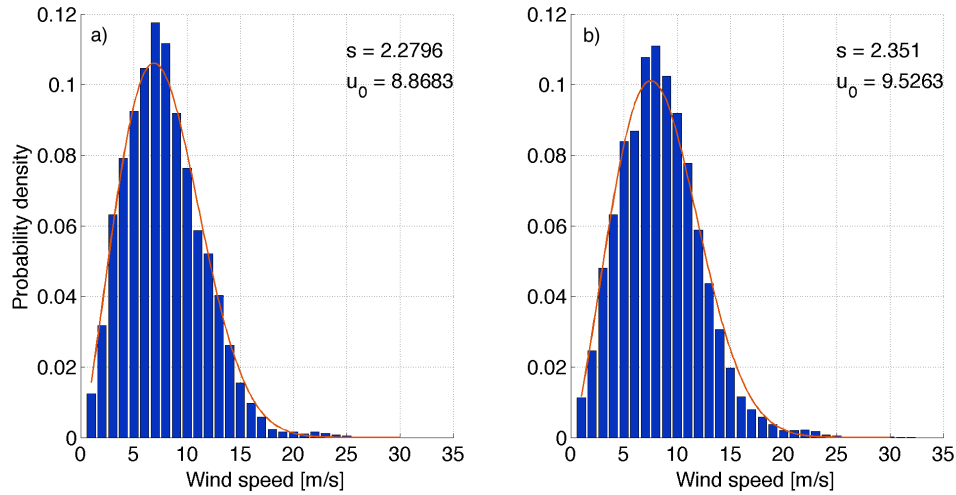


Figure 5.11: Overall histogram of the wind speed measurements at 80 m and corresponding Weibull distribution (red) for a) sonic anemometer and b) combined wind measurements from the Windcube V1s

tograms of the horizontal wind speed at 80 m altitude for the entire field experiment are illustrated in figure 5.11, along with fitted Weibull distributions. The sonic anemometer measurements are shown in 5.11 a). Peaking at about 7 m s^{-1} the distribution has a fairly narrow spread and is slightly skewed to the right. The entire distribution is ever so slightly shifted towards higher wind speeds for the assumed undisturbed wind measured by the Windcube V1s (figure 5.11 b)) with a peak at 8 m s^{-1} , but the spread is fairly similar in both cases.

5.3.2 Wind direction

Wind roses for the campaign are plotted in figure 5.12. In addition to showing the directional distribution, the wind rose also displays how the wind speed is distributed within the specific wind direction range. As illustrated by both figures 5.12 a) and b), the dominant part of the wind is south-westerly, which was previously described as the site's prevailing wind condition in section 3.3. The measure-

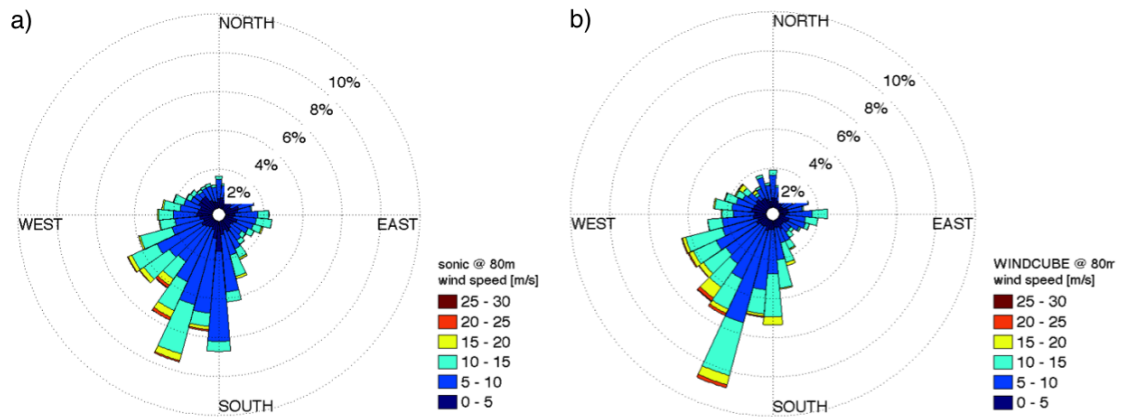


Figure 5.12: Wind direction distribution at 80 m for the entire campaign for a) the sonic anemometer and b) combined measurements from Windcube V1s

ment instruments are thus properly placed to catch the wind turbine wake from WT6 in the main wind direction. No other distinct peak in the wind direction can be seen, but measurements from the Windcubes have a more distinguishable peak in the wind direction sector 210° - 220° . A slight increase in wind speeds can be seen in the LiDAR measurements for winds coming from North of the research turbine row, even though the low percentage in winds from this direction remains. Furthermore looking at southerly winds, where the sonic anemometer is in the shadow of the met-mast, there is a significant decrease in the wind speed compared to what is measured by the LiDARs. For the LiDARs a large fraction of the wind speed coming from this direction is above 10 m s^{-1} , whereas nearly all measurements are below 10 m s^{-1} for the sonic anemometer.

Chapter 6

Effects of Stability

Section 2.2.2.1 describes how the wind profile changes with stability, but also the characteristics of the wake will vary with the different stability classes. The turbulent mixing in the ambient wind field helps to draw momentum from the surroundings into the wake region, leading to reduced wind deficits and a shallower wake expansion. Enhanced turbulence in unstable conditions will therefore most likely result in a weaker wake, while the opposite is the case for a stably stratified boundary layer where vertical motion is more inhibited (Alblas et al., 2014).

6.1 Vertical profiles

Static LiDAR instruments can be used for full scale observations of the vertical wind profile inside the wake. The most relevant properties for the wake analysis is the decrease in mean horizontal wind and the increase in turbulence. Varying with both, the surrounding meteorological conditions, as velocity of the incoming flow and atmospheric stability, and the wind turbine control settings, as blade pitch, the behaviour of an individual wake is truly complex. The wake profile behind WT6 has been measured by both WLS-37 and WLS-65, and the vertical variation in horizontal wind speed and TI as a function of stability is presented in this chapter. The effect of turbine control is discussed in more detail in Chapter 7. As the turbine wake is in focus, the dataset is filtered to only include measurements

taken when WT6 was generating power.

6.1.1 Horizontal wind speed deficit

In order to analyse and compare the wind speed deficit in the wake region, the wind speed is normalized by the value of the undisturbed incoming wind speed measured by WLS-67 at the nacelle height of 80 m. Figures 6.1 and 6.2 show the wake profiles measured by the three static LiDARs for incoming wind directions a) 0-360°, b) 207-247°, and c) 217-237°. While figure 6.1 illustrates how the wake evolves downstream, comparing the three LiDAR measurement with each other, the effect of the atmospheric stability on each instrument is more easily seen in figure 6.2, where the differences between a stable, neutral and unstable ABL are displayed with solid, dashed and dotted lines, respectively. The wind profiles of the undisturbed wind field measured by WLS-67 shows a nice similarity to the theoretical wind profiles displayed in figure 2.3 a). The profiles measured by WLS-37 and WLS-65 reveal, however, a wind speed reduction of up to 40% at hub height, depending on stability conditions and downstream distance from the wind turbine. As expected only a weak signal is detectable for the unfiltered data set with respect to the wind direction (figure 6.1 a)). Centering in towards the wake line of 227°, the effect becomes more pronounced for all stabilities, expressed by an increase in the wind speed deficit. Narrowing the wind direction range from 40° to 20° in figure 6.1 c), increases the wind speed loss by several percent. Depending on the stability condition, the turbulent mixing is either enhanced or suppressed, leading to respectively smaller or larger wind speed deficits. Figure 6.2 illustrates that the decrease in horizontal wind speed is significantly larger for stable cases than for both unstable and neutral situations. The wake deficit is generally larger at an altitude of 60 m, i.e. slightly below hub height. For the narrowest (20°) wind direction interval and 1.8 D downstream, it reaches 40% in the stable situation and of about 30% for the neutral and unstable cases. Further downstream at 3.5 D, the effect has already decreased to 30% (stable) and 20% (neutral and unstable). Previous measurements of velocity deficits inside wind turbine wakes at different downstream positions, are summarized in Aitken et al. (2014). For stable

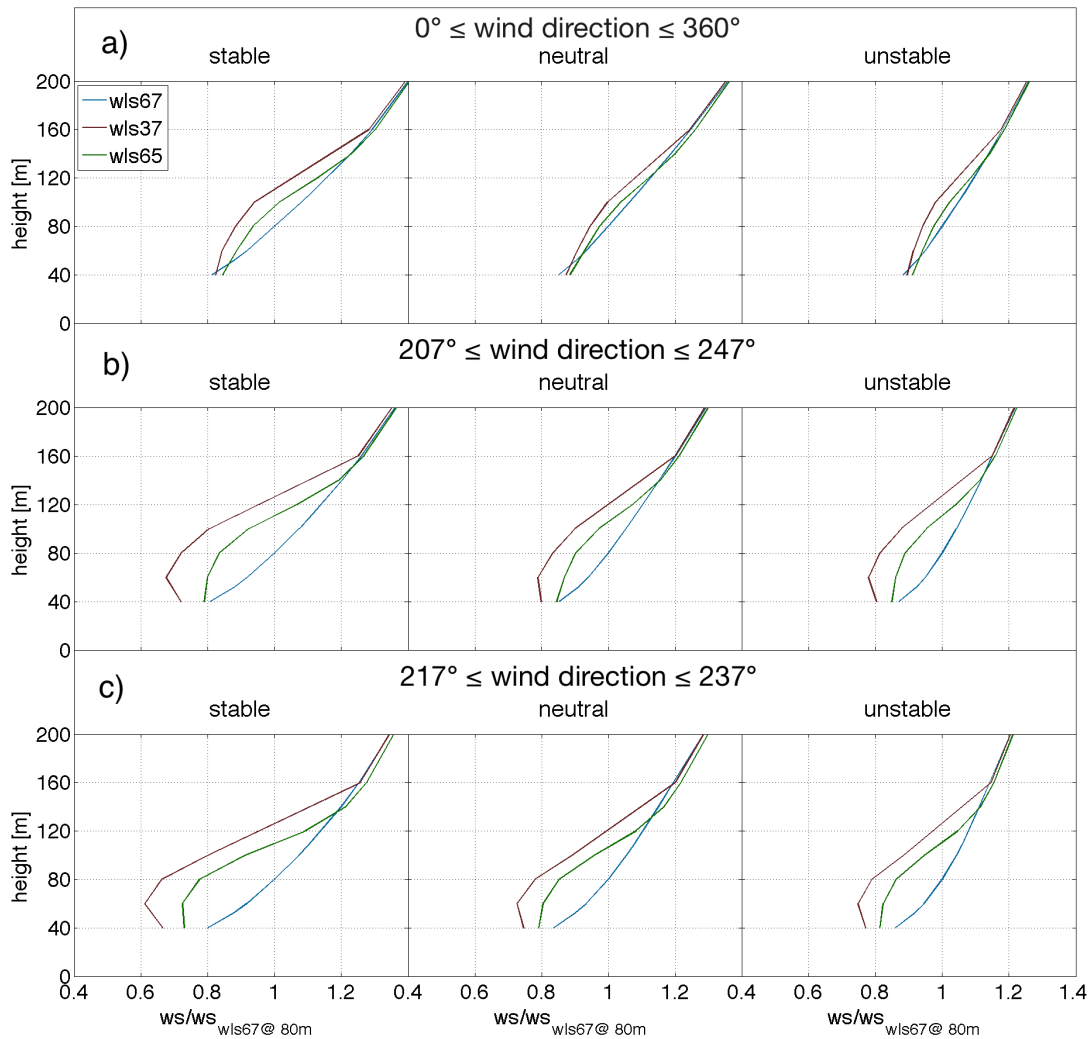


Figure 6.1: Mean wind speed measured by WLS-67 (blue), WLS-37 (red) and WLS-65 (green), normalized by WLS-67 at 80 m, for stable, neutral and unstable conditions for wind directions a) 0° - 360° , b) 204° - 247° and c) 217° - 237° .

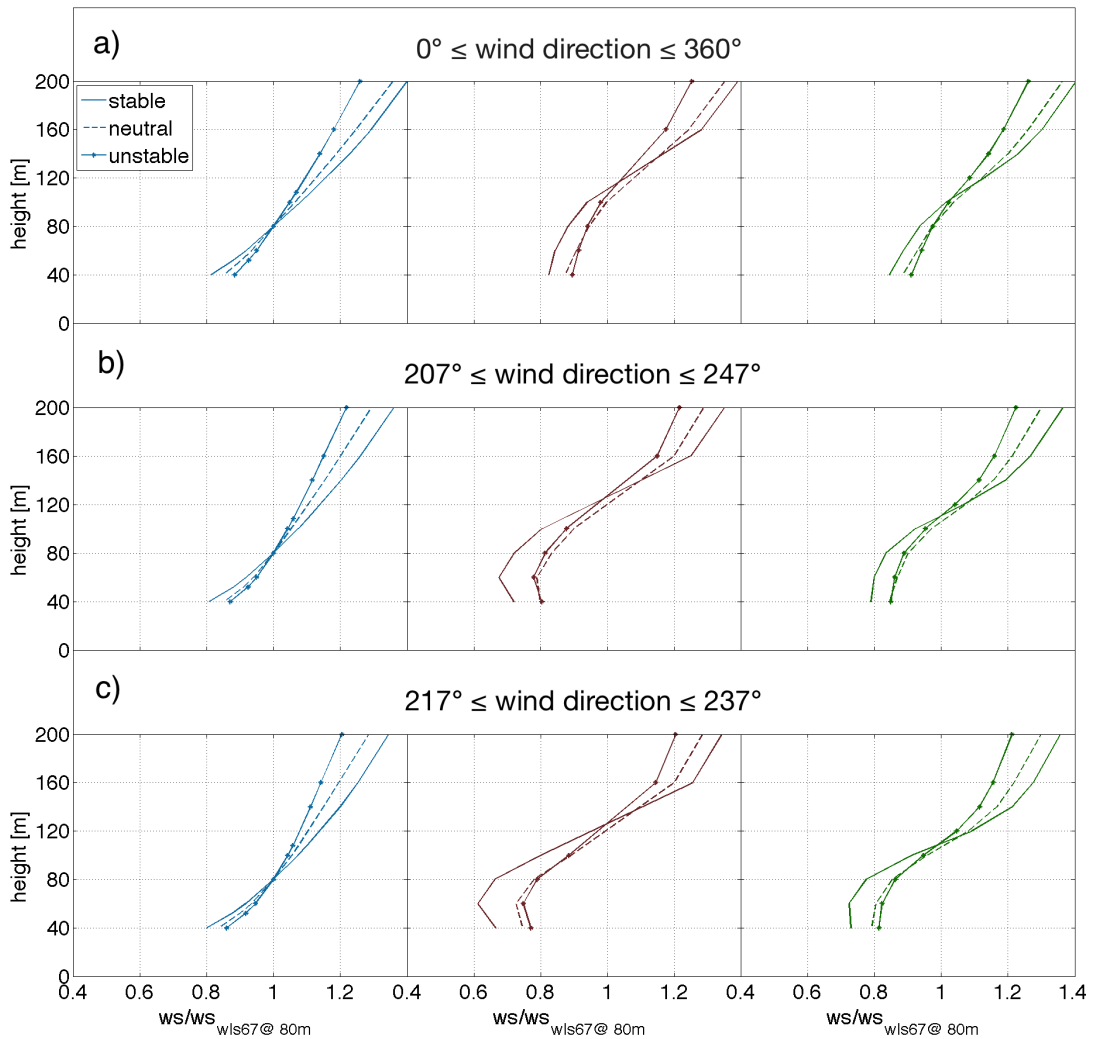


Figure 6.2: Mean wind speed measured by WLS-67 (blue), WLS-37 (red) and WLS-65 (green), normalized by WLS-67 at 80 m, for stable (solid line), neutral (dashed line) and unstable (dotted line) conditions for wind directions a) 0° - 360° , b) 204° - 247° and c) 217° - 237° .

conditions, the measured deficit at Wieringermeer, at both 1.8 D and 3.5 D, is in good agreement with the earlier records, while stable and unstable cases measure deficits slightly below the reported ones.

The vertical wake expansion is, however, fairly similar under all types of atmospheric stratification, and seem to reach an altitude of 160 m when measured by WLS-37, but decreases to about 120 m for measurements taken by WLS-65 further downstream at a distance of 3.5 D. This is somewhat unexpected, as wake models in general predict a typical wake expansion also in the vertical (e.g. Fitch et al. (2012)). Obviously is the location of the second downstream LiDAR during the WINTWEX-W campaign already far enough downstream that the vertical expansion at that point is overcompensated by downward mixing of momentum that tends to reduce the wake deficit. This result is also in accordance with findings by Iungo et al. (2013) from scanning LiDAR wake measurements of a single ENERCON 2 MW wind turbine performed in Switzerland. They reported a steep increase of the wake region right behind the turbine, reaching 0.8 D above the hub height at a distance of 1 D downstream. With increasing distance from the turbine the vertical wake extension decrease to about 0.5 D above hub height at a distance of 3.5 D, which is in excellent agreement with our measurements.

6.1.2 Horizontal turbulence intensity

Figure 6.3 shows that the profiles of TI in upstream conditions are, as expected, decreasing with stronger stratification and altitude. The LiDARs situated in the wake of WT6 does, however, show a large increase in turbulent activity centred around hub height. Narrowing in the wind direction on our particular region of interest, i.e. the wake line of WT6 at 227° , nearly doubles the horizontal turbulence intensity for stable conditions. The difference in TI with downstream distance is, however, relatively small. Varying between 0 and 2% at hub height, the increase of TI in the wake region is fairly similar for measurements done by WLS-37 and WLS-65, at respectively 1.8 D and 3.5 D. Looking at the different stability classes, the enhanced TI in the wake region is largest for stable cases, where the TI in-

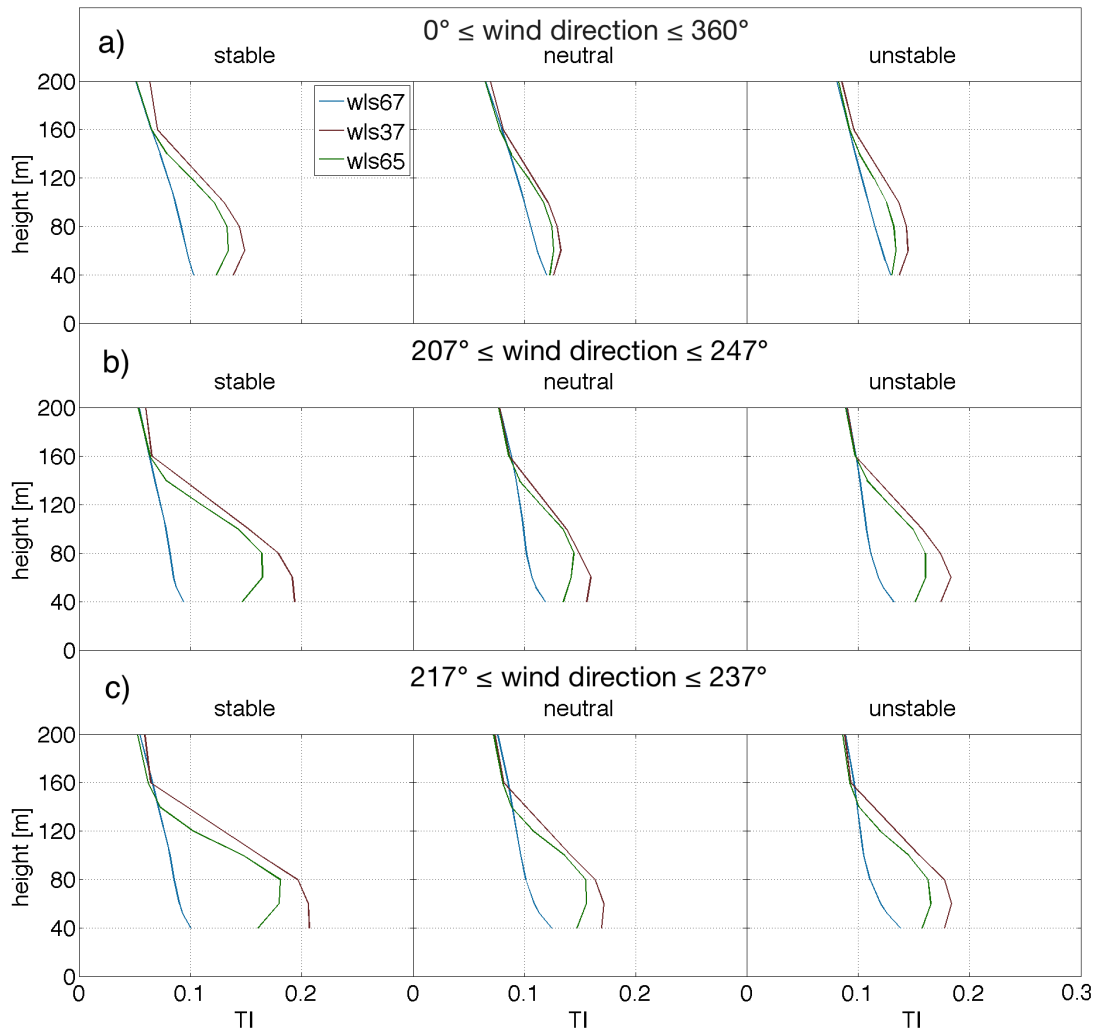


Figure 6.3: Mean horizontal turbulence intensity measured by WLS-67 (blue), WLS-37 (red) and WLS-65 (green) for stable, neutral and unstable conditions for wind directions a) 0° - 360° , b) 204° - 247° and c) 217° - 237° .

creases by more than 10%. TI measurements, from WLS-37 and WLS-65 during stable conditions, reaches values surpassing both neutral and unstable situations, even though TI was initially lowest for the stable cases. When comparing TI measurements filtered for incoming wind directions 217° to 237° , the peak values in stable situations reach about 5% higher than for neutral and unstable events. Even though model simulations of TI in the wake, tend to have its largest increase above hub height (e.g. Wu and Porté-Agel, 2012), the peak values measured by the downstream LiDAR in this campaign are centered around 60 m.

Determining the vertical wake expansion by the increased TI leads to similar results as using wind speed deficits, when looking at measurements taken from WLS-37, reaching an altitude of 160 m. WLS-65, measuring further into the wake, does, however, show a larger vertical extension of TI than derived from the wind speed deficits, reaching altitudes closer to 150 m rather than 120 m. One possible explanation for this behaviour could be an enhanced shear production of turbulence at the edge of the wake leading to higher TI values.

6.2 Wind distribution

The wind speed distribution for the different stability classes throughout the campaign for all wind directions is displayed in figure 5.10. Looking more thoroughly at the wake region, filtering for wind direction from 207° to 247° , shows a similar distribution, where stable cases seem to be associated with low wind speeds and neutral conditions tend to have a distribution shifted towards higher velocities (figure 6.4). As the wind speed increases, the turbines efficiency decreases as the blades are pitched out of the wind (see also Chapter 7). This results in a larger flow through the rotor plane and therefore results in a weaker wake. This is clearly shown in both figure 5.6 and figure 5.7, where the wind speed deficit and increased TI in the wake region are substantially larger for lower velocities. The wind speed distributions of figure 6.4 indicate that the results presented in the previous section may not solely be due to the effects of stratification and turbulence of the incident

flow, but it can also be a result of the incoming wind speed and the corresponding changes in turbine control.

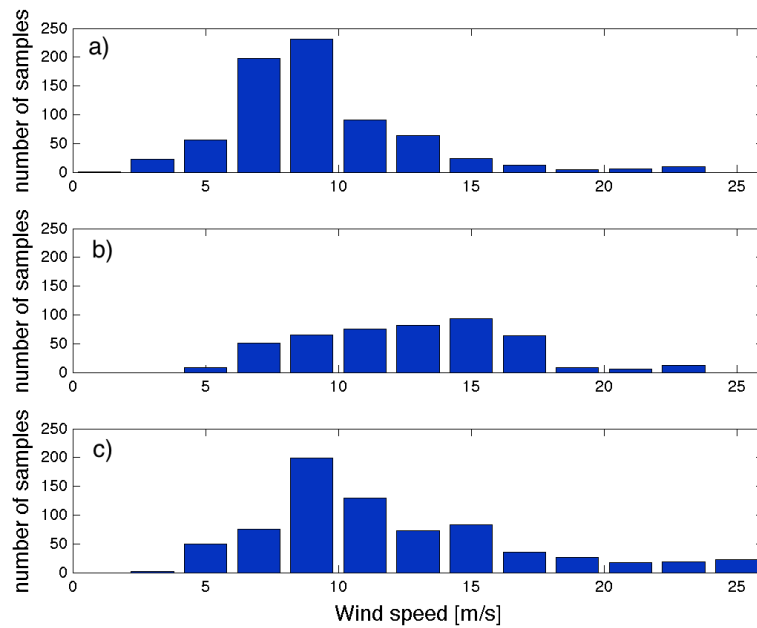


Figure 6.4: Wind speed distribution from wind directions 207° and 247° for a) stable, b) neutral and c) unstable conditions.

Chapter 7

Effects of Turbine Control

To avoid over exhausting of the wind turbine's generator, the power produced is limited for wind speeds exceeding the rated velocity. The NORDEX N80 turbine has an active power regulation referred to as pitch control (NORDEX, 2016). Altering the pitch angle of the turbine blades will result in a new power coefficient, changing the efficiency of the wind turbine and keeping the power output constant at the maximum level. The variations in power coefficient for NORDEX N80 wind turbines with wind speed is displayed in figure 2.1. The following chapter illustrates how pitch angles alter with incoming wind speeds at hub height, and the effect this has on the wind speed deficit in the wake. Further on a description of the changes in the vertical profile with varying blade pitch angle is given. The ratio plots in section 5.1.1.2 indicate that the WT6 wake's horizontal expansion ranges from $207^\circ - 247^\circ$, therefore are the wake investigations in the following chapter filtered for these wind directions. Similarly to the previous chapter, the data is also filtered to only include measurements where WT6 is generating power, since the focus of this analysis is to catch the wind turbine's effect on the downstream wind field under operational conditions.

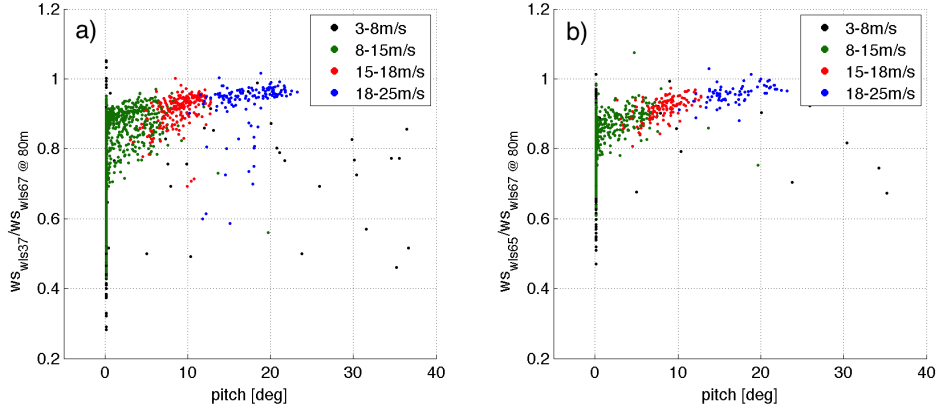


Figure 7.1: Wind speed ratio of a) WLS-37 and b) WLS-65 over WLS-67 at hub height. The measurements are separated into four interval based on the velocity of the incoming wind: $3\text{--}8\text{ m s}^{-1}$ (black), $8\text{--}15\text{ m s}^{-1}$ (green), $15\text{--}18\text{ m s}^{-1}$ (red) and $18\text{--}25\text{ m s}^{-1}$ (blue).

7.1 Effects of blade pitch angles on horizontal wind speed at hub height

The changes in wind speed deficits at hub height relative to the incoming velocity of the wind and the blade pitch angle, are shown in figure 7.1. For incident wind speeds below 8 m s^{-1} (black dots), and a portion of the speed interval $8\text{--}15\text{ m s}^{-1}$ (green dots), the pitch is centred around 0° . This indicates the wind speed range where the produced power of the turbine is determined by a variable rotational speed of the rotor. For higher wind speeds a functional relationship between wind speed ratio and pitch angle appears. As expected, an increase in wind speed results in a larger blade pitch angle. The three wind speed intervals in figure 7.1 exceeding 8 m s^{-1} , clearly correspond to certain pitch angle intervals. Wind speeds between 8 m s^{-1} and 15 m s^{-1} are associated with pitch angles between 0° and 6° , $15\text{--}18\text{ m s}^{-1}$ with $6^\circ\text{--}12^\circ$ and $18\text{--}25\text{ m s}^{-1}$ with $12^\circ\text{--}22^\circ$. Additionally, the wind speed deficits between measurement taken downstream and upstream of

WT6, continue to decrease as the blade pitching increases in correspondence to the higher wind speeds. For pitch angles around 0° the decrease in wind speeds are as high as 70% for WLS-37 at 1.8 D downstream, and 50% for WLS-65 at 3.5 D. However, increasing the pitch angle ever so slightly, result in much smaller wind speed deficit. A blade pitch of 5° reduces the wind speed deficit, measured by WLS-37, to less than 20%, while a pitch angle of approximately 1 has the same effect on deficits measured by WLS-65. As the blade pitch angle reaches 20° , the wind speed deficit approaches 0, and the pronounced effect of the wind turbine on the wind speed will have disappeared. As a result it is clear to conclude that pitch has a pronounced effect on the wake's strength.

7.2 Vertical profiles

Variations in the vertical profiles of wind speeds and TI with altering blade pitch angle in addition to stability, are shown in figure 7.2 and figure 7.3, respectively. The figures are separated in three pitch angle intervals, ranging from $0^\circ - 3^\circ$, $3^\circ - 8^\circ$ and $8^\circ - 30^\circ$. It is evident from both figures that the largest reduction in wind speed, and highest increase in turbulence intensity, correspond to the cases where the blade pitch does not exceed 3° . Mean horizontal wind speed ratios of the downstream LiDAR measurements, normalized by the value of the wind speed measurements from WLS-67 at hub height, are presented in figure 7.2. A blade pitch angle below 3° results in an increase in the wind speed deficit of more than 20%, depending on stability and downstream distance from the wind turbine. For instance, in stable conditions, wind speed deficit measured by WLS-37 at 1.8 D downstream, grows from 10% to 30% at hub height when the blade pitch interval changes from $3^\circ - 8^\circ$ to $0^\circ - 3^\circ$. A similar change can be seen in the measurement from 3.5 D downstream, where the wind speed deficit rises from 5% to 20%. Further increasing pitch angles from $3^\circ - 8^\circ$ to $8^\circ - 30^\circ$, however, have only little effect on the strength of the wake, which only decreases to a value of around 8% at 1.8 D and 3% at 3.5 D.

Comparing the wake profile for different stability conditions, the stable cases continue to have the largest velocity deficits in situations with low pitch. When the blade pitch remains below 3° , the wind speed ratio at 1.8 D downstream of WT6, has decreased by 30% in stable situations, and to about 25% in neutral and unstable cases. The effect subsides further downstream at 3.5 D, where the deficits are approximately 20% and 15% for stable situations and neutral and unstable cases, respectively. However, this pattern seems to disappear for blade pitches larger than 3° . In fact the wind speed deficit appears to be slightly higher for unstable cases, when the blade pitching is between 3° and 8° , in particular for WLS-65. Exceeding a pitch of 8° , all atmospheric conditions show similar wind speed profiles with only small differences of up to 5%, between the upstream and downstream LiDAR measurements.

Changes in TI with altering pitch for different stability conditions are shown in figure 7.3. Similarly to the wind speed deficits, the largest wake effect is seen for low blade pitching in a stably stratified boundary layer, where the increase in TI is about 10%. More precisely, for blade pitch angles between 0° and 3° , the added increase in TI at 1.8 D downstream is 10% for stable conditions and 7% for neutral and unstable cases, even though the highest TI values, i.e. 20%, are to be found during unstable situations. In spite of the distance separating the two LiDARs placed in WT6's wake, there are only small variations in the measured TI . The difference seems to grow smaller for larger blade pitch angles, with the exception of stable conditions with pitch angles exceeding 8° .

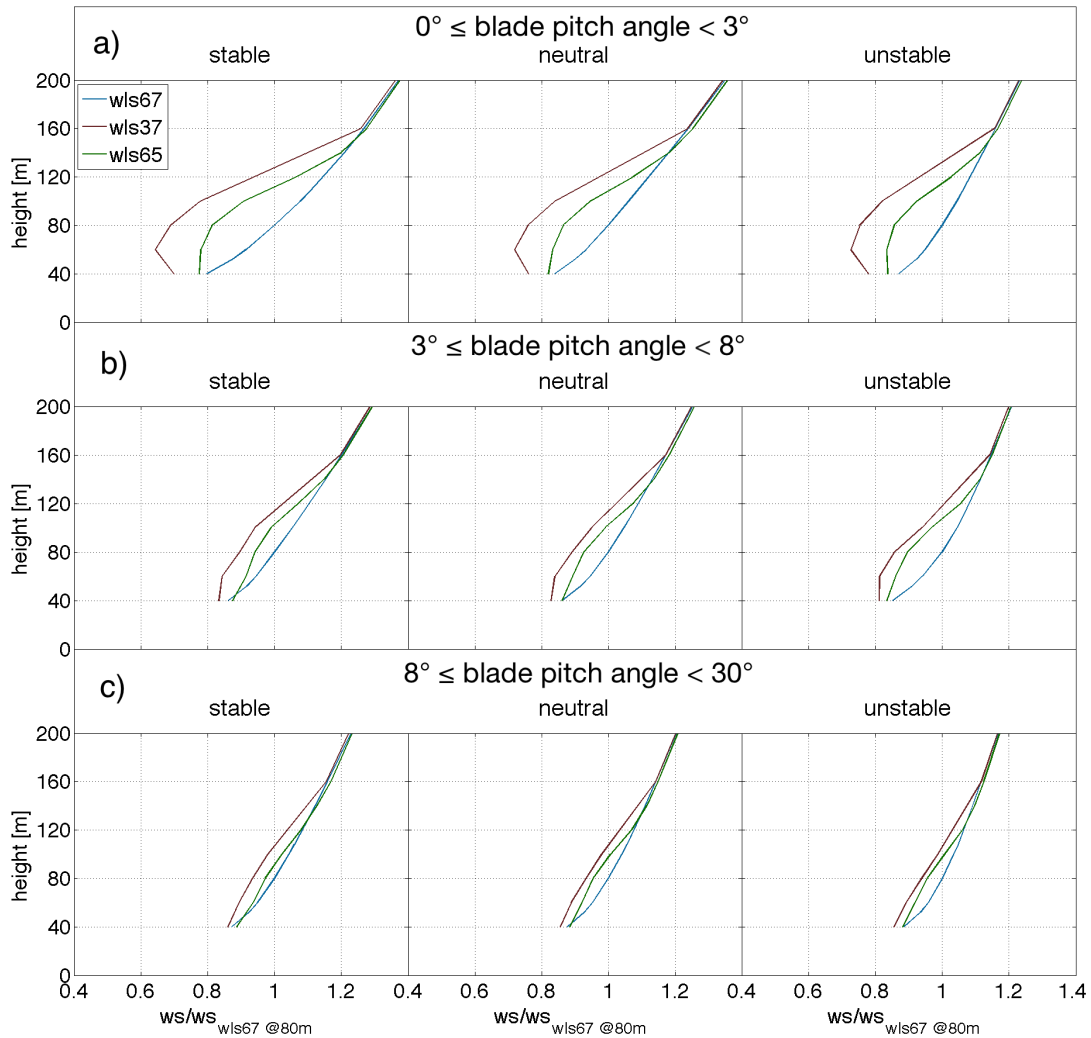


Figure 7.2: Mean horizontal wind speed measured by WLS-67 (blue), WLS-37 (red) and WLS-65 (green) normalized by hub height measurements from WLS-67. The stable, neutral and unstable conditions are separated by blade pitching $0^\circ - 3^\circ$ in a) and subsequently $3^\circ - 8^\circ$ in b) and $8^\circ - 30^\circ$ in c).

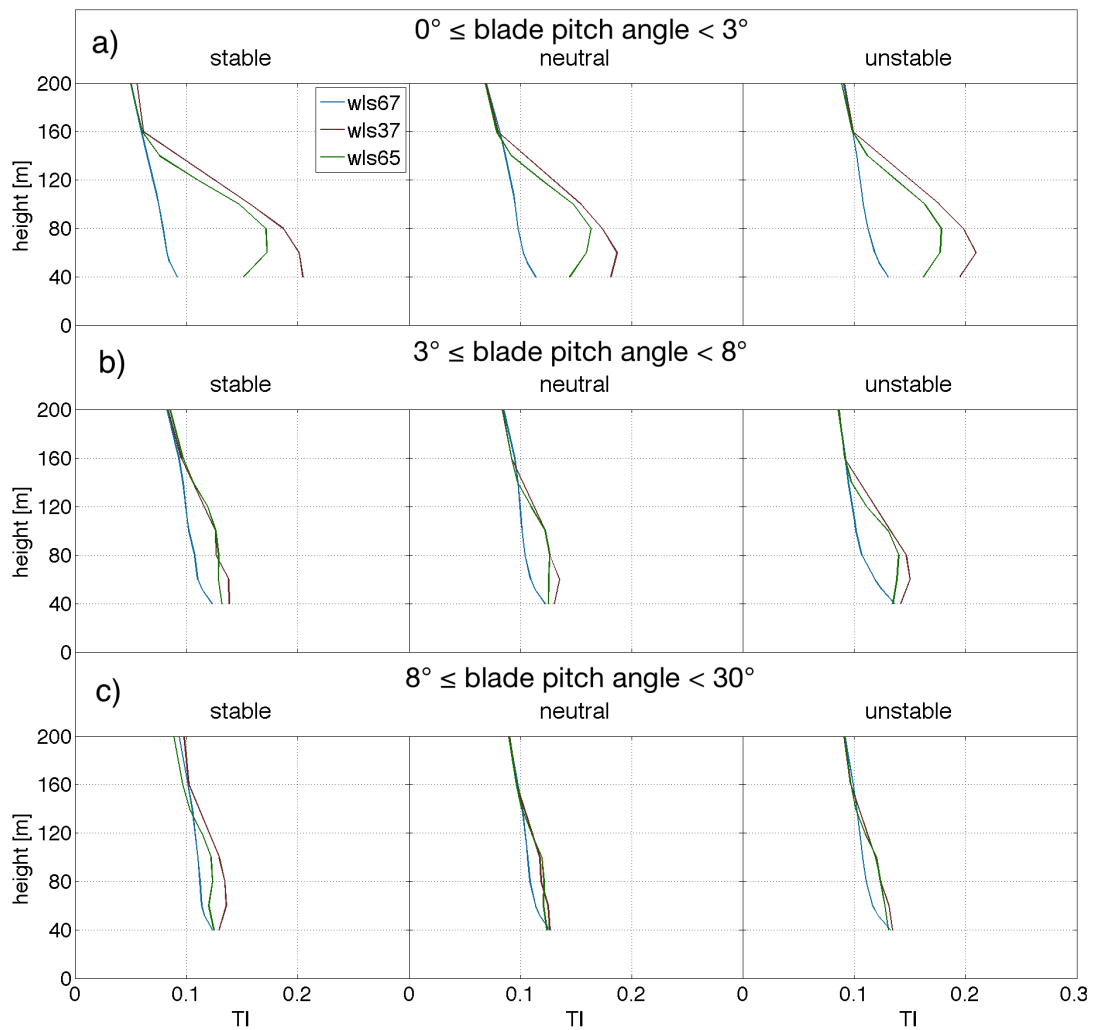


Figure 7.3: Mean horizontal turbulence intensity measured by WLS-67 (blue), WLS-37 (red) and WLS-65 (green). The stable, neutral and unstable conditions are separated by blade pitching $0^\circ - 3^\circ$ in a) and subsequently $3^\circ - 8^\circ$ in b) and $8^\circ - 30^\circ$ in c).

7.3 Sample size

Pitching is strongly affected by the wind velocity. The larger the wind speed, the more pitching is required to lower the efficiency and to limit the power production to 2.5 MW. The distribution of wind speed with stability classes for south-westerly winds, described in Chapter 6, shows that there are large variations in the number of events for the different velocities in stable, neutral and unstable situations. The few incidents where stable conditions coincide with high wind speed is why there are so few stable cases of pitching above 3° , leading to choppy profiles. This effect is particularly visible for TI in figure 7.3. Table 7.1 shows the number of incidents of the different pitching angles in the three stability classes for an estimation of the significance of the presented profiles.

Pitch	Number of samples		
	$0^\circ - 3^\circ$	$3^\circ - 8^\circ$	$8^\circ - 30^\circ$
stable	625	61	47
neutral	245	206	105
unstable	465	194	118

Table 7.1: Number of samples in the three stability classes for different blade pitching.

Chapter 8

Conclusion

8.1 Summary

Three pulsed LiDAR wind profilers were deployed in a seven month field campaign at ECN's test site in Wieringermeer, focusing on capturing the single wake structure and dynamics from a NORDEX N80 research wind turbine. Combining these measurements with SCADA data from the turbine and measurements from a nearby met-mast, both of which provide averaged data over 10 minutes intervals, the 10 minutes statistical data from the LEOSPHERE's Windcube V1 instruments were initially used. Due to inconsistencies and errors in this statistical dataset, a more thorough investigation of the raw data, with a temporal resolution of 1 second, had to be performed. Raising the CNR threshold to -22 dB and discarding measurements 10 minutes before and after a wiper swipe, removed most of the bad quality data. The remaining irregularities and spikes were filtered by developing and applying a de-spiking routine. It is based on a standard deviation threshold applied on a block average, filtering out points outside the chosen standard deviation interval.

The deployment of several wind LiDAR systems allowed for a thorough site characterization, describing potential disturbances by the surrounding turbines and the meteorological mast, and their affect on the wind speed and turbulence measured

by the different systems as function of the wind direction. The results illustrate a very complex wind field, influenced by all the nearby research wind turbines and the met-mast, decreasing wind speeds by up to 50% and increasing turbulence intensities by more than 20% in the corresponding wake or flow distortion regions. For prevailing wind conditions, represented by south-westerly winds, the instrumentation placed South of research wind turbine number 6, i.e. the met-mast and WLS-67, seem to experience mainly undisturbed winds, and are therefore expected to give a good representation for upstream conditions. However, the met-mast measurements are strongly influenced by the structure of the mast tower, decreasing the wind speed by up to 40%. Looking at wind speed and wind direction distributions, it might therefore be beneficial to combine measurements from the three LiDARs instead of using the sonic anemometer measurements alone.

Trying to separate the measurements into cases where the ABL was either stable, neutral or unstable, by assuming that the atmosphere's lapse rate equalled the dry adiabatic lapse rate of 10 K km^{-1} , resulted in an unrealistic distribution of stability occurrences. A new, empirically estimated, stability criteria was developed by filtering the data for neutral conditions, i.e. high wind speed events during night. The temperature difference over 27 m has been found to be on average -0.06 K for those conditions. Consequently, the temperature difference interval from -0.01 to -0.11 has been chosen to represent neutral conditions in this study, while larger (smaller) differences will result in a stable (unstable) situation.

Investigating the wake's vertical profile of normalized wind speed and turbulence intensity measured by the LiDAR instruments, both stability and blade pitch angle were taken into account. While the difference between neutral and unstable conditions is virtually non-existent, a stably stratified ABL results in larger wake effects. The normalized wind speeds in the wake decrease by 10% more at hub height for stable situations compared to the other stability classes, looking at wind directions centred around the wake line of 227° . Slight changes in pitch dramati-

ically alters the vertical profile of the turbulence intensity and normalized wind speed. Increasing the blade pitch angle reduces the extraction of wind energy and results in a lower efficiency of the turbine. Consequently, the wake effect will not be as pronounced as it is for lower pitch angles. The effect of the stability, still evident for small blade pitching, where stable cases still results in a stronger wake, seems to vanish for blade pitch angles exceeding 3° .

The small differences between neutral and unstable cases for all the vertical wake profiles is most likely caused by the fact that most high wind speed events are associated with neutral conditions, which becomes apparent when looking at the wind speed distribution of the different stability classes. As both wind speed, TI, stability and pitch are all interlinked, it can, however, be difficult to quantify the effect of a single variable, and filtering the dataset to too specific scenarios may lead to sample size that are too small for a reliable outcome.

8.2 Further Outlook

This study has shown how wind speed and turbulence intensity are dependent on stability and blade pitch angle. However, due to the unforeseen issues with the data quality of the LiDAR dataset, the analysis of the single turbine wake was not as extensive as initially intended. For a more direct link to turbine performance it would be useful to link the result of stability and pitch to power output. It would also be interesting to look more closely into fine scale pitching in the range between 0° and 3° , where the largest effects have been detected. This information will be of particular interest for new turbine control strategies based on individual blade pitch. The compiled data set could also allow for an investigation of the statistics and dynamics of wake meandering. A first attempt to detect a corresponding signal in the raw dataset of the downstream LiDAR wind profilers was made, filtering the data for time intervals with a relative constant wind direction around the wake center line of 227° . One of the ideas is to block average the raw data over different time intervals of 5, 10, 20, 30 and 60 s, to detect a typical

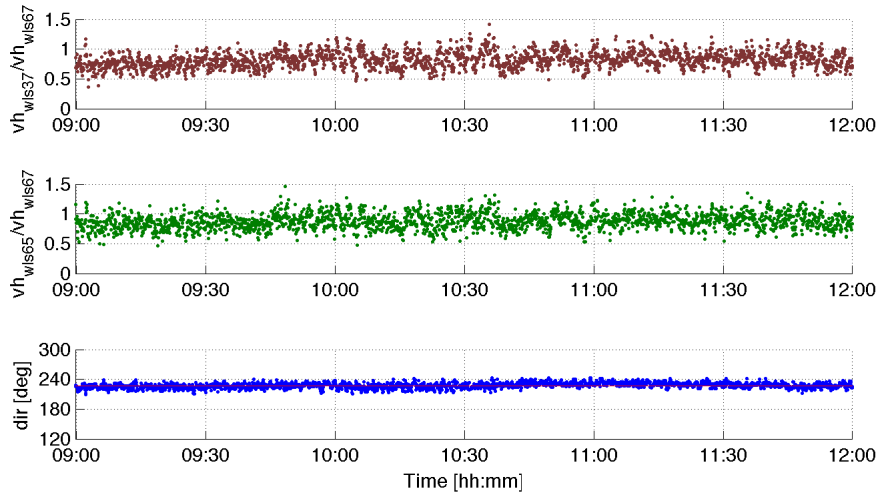


Figure 8.1: Wind speed ratios between a) WLS-37 and b) WLS-65 and WLS-67 measured at hub height. Measurements are from 8.Jan.2014.

time scale for the meandering. One example for a selected 3 hour time interval, averaged over 5 s, is shown in figure 8.1. Although no consistent and clear pattern was detected in this case, there are definitely some altering structures in the wind speed ratio, visible, in particular, between 10:00 and 12:00 and for the LiDAR 1.8 D downstream. A more detailed analysis of these structures, and their possible link to wake meandering, would be a great addition to this single turbine wake investigation.

For future measurement of wakes with LiDAR instruments it could be beneficial to have additional measurements of the temperature profile and of turbulent fluxes for the classification of stability by Richardson number or Obukhov length. I will also stress the importance of having a substantial dataset that is large enough to filter the measurement to specific situations. Other advantages can come from including the data from both the scanning LiDAR, located ca. 12 D downstream, and from the nacelle mounted LiDAR, that are available at least for parts of the WINTWEX-W campaign, as they can offer a more detailed insight in the wake's

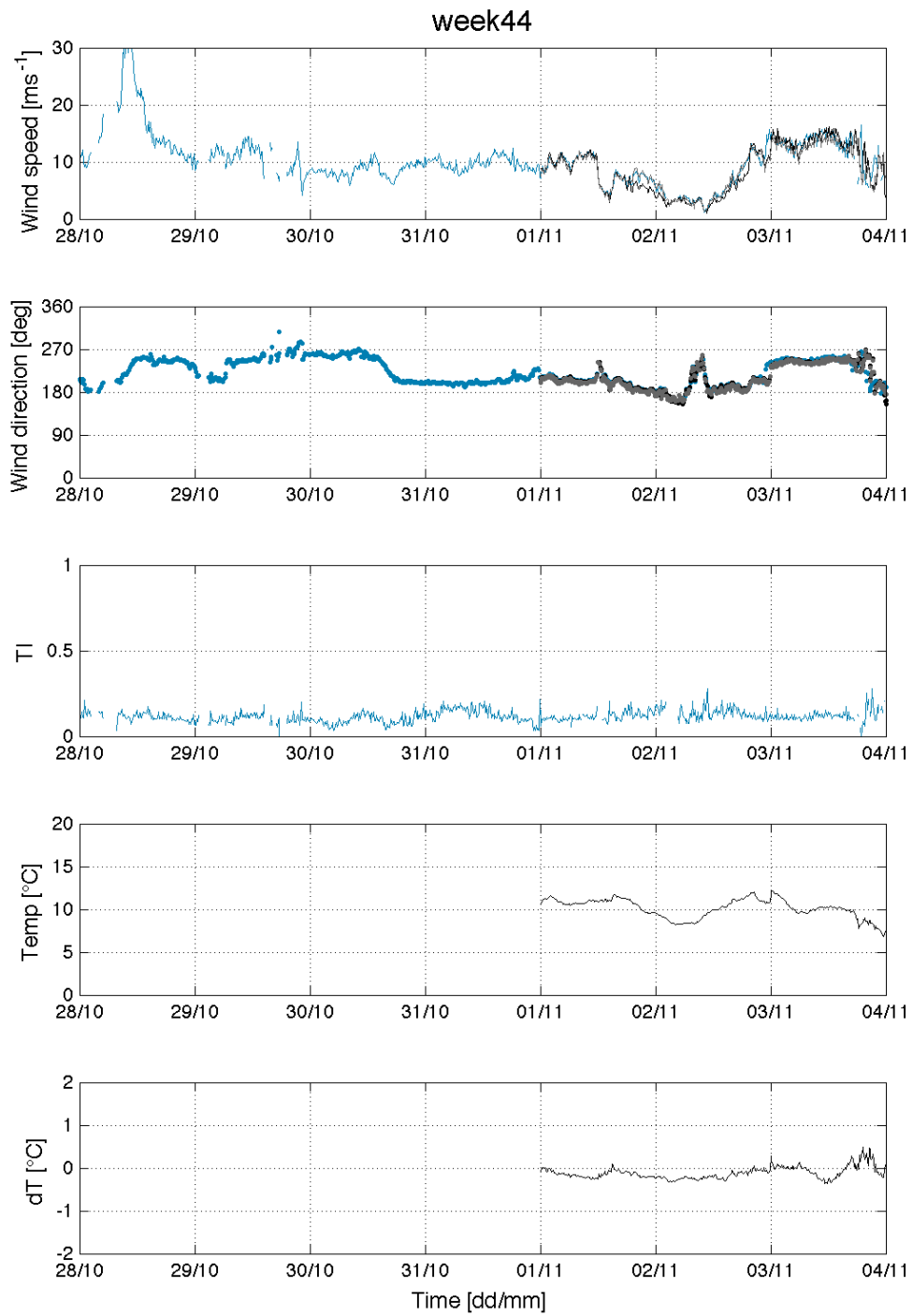
dynamics, and will give the opportunity to investigate more specific wake propagation structures, like wake meandering.

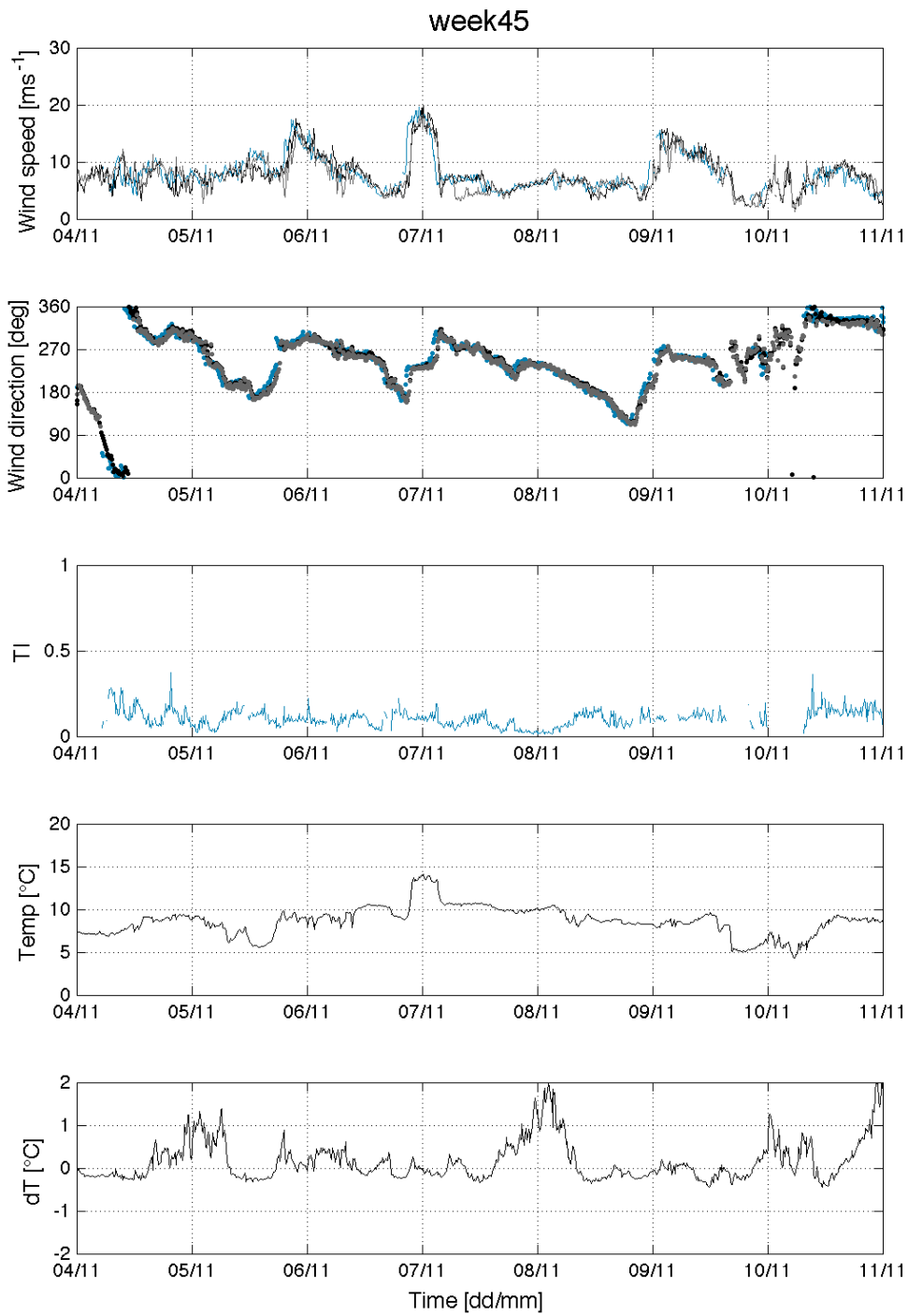
In addition I personally feel that future measurement campaigns of wind turbine wakes should also focus on higher altitudes. The potential vertical range of the LiDAR wind profilers of 250 – 300 *m*, makes it possible to perform wake measurements in all levels relevant for state of the art and future wind turbines. Full scale observations may lead to a better understanding of the wake's dynamics and evolution beyond the surface layer, and can help to make wake models more suited for the larger wind turbines of the future.

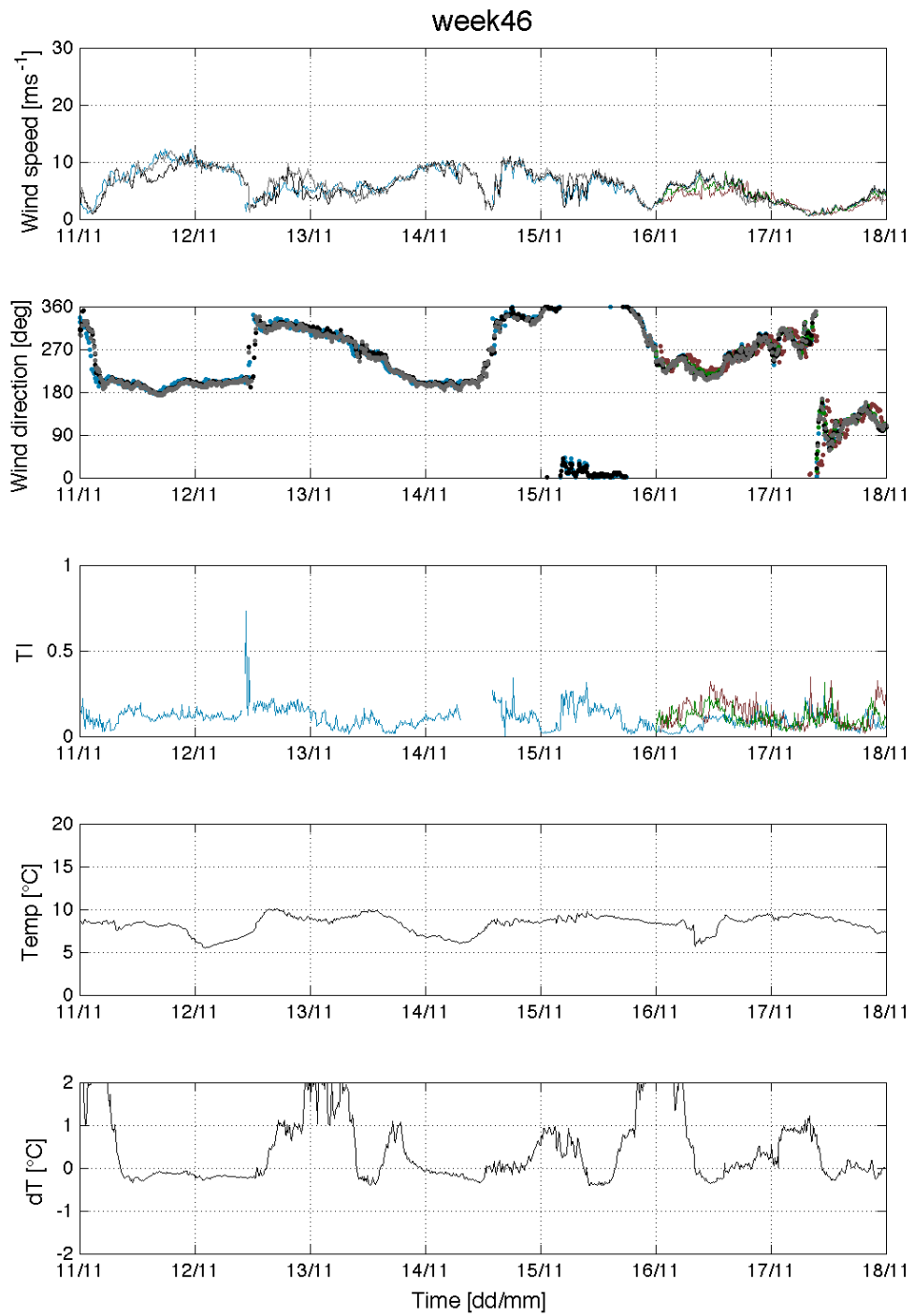
Appendix A

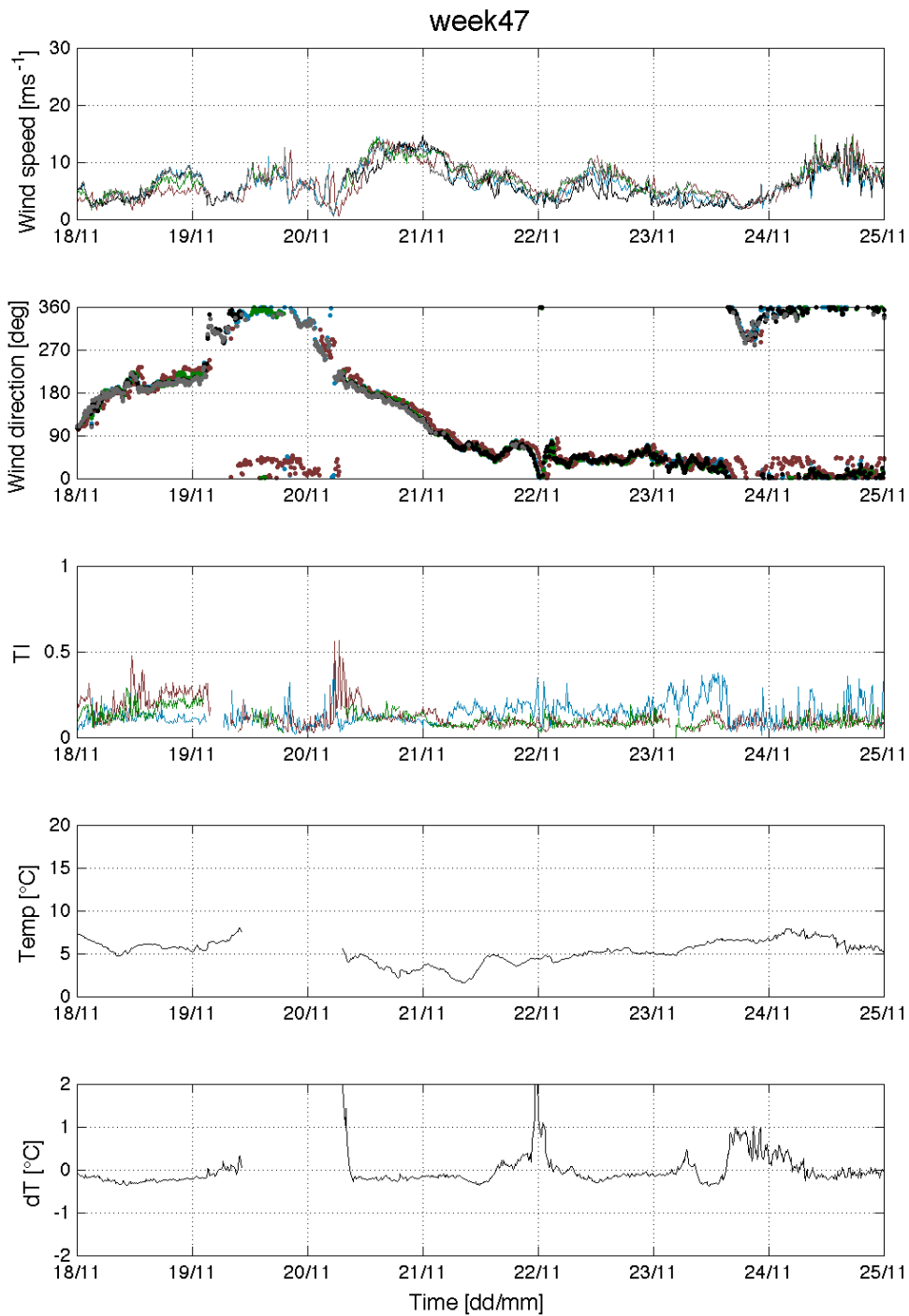
Weekly plots

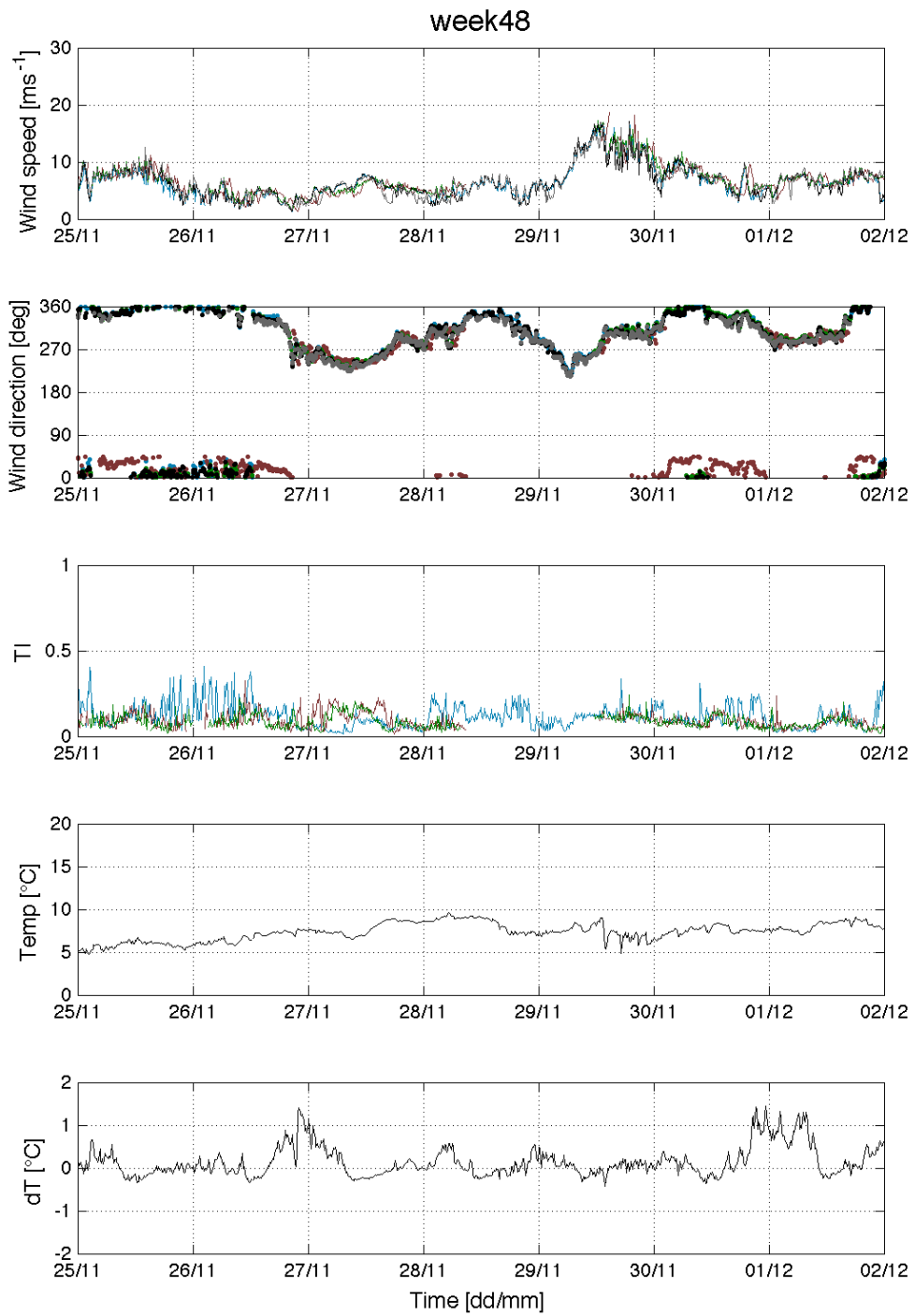
Weekly time series of 10 minute averaged horizontal wind speed, wind direction and turbulence intensity measured at hub height by sonic anemometer (black), WLS-67 (blue), WLS-37 (red), WLS-65 (green) and WT6 (grey), and temperature and temperature difference measurements from the met-mast, throughout the entire WINTWEX-W campaign.

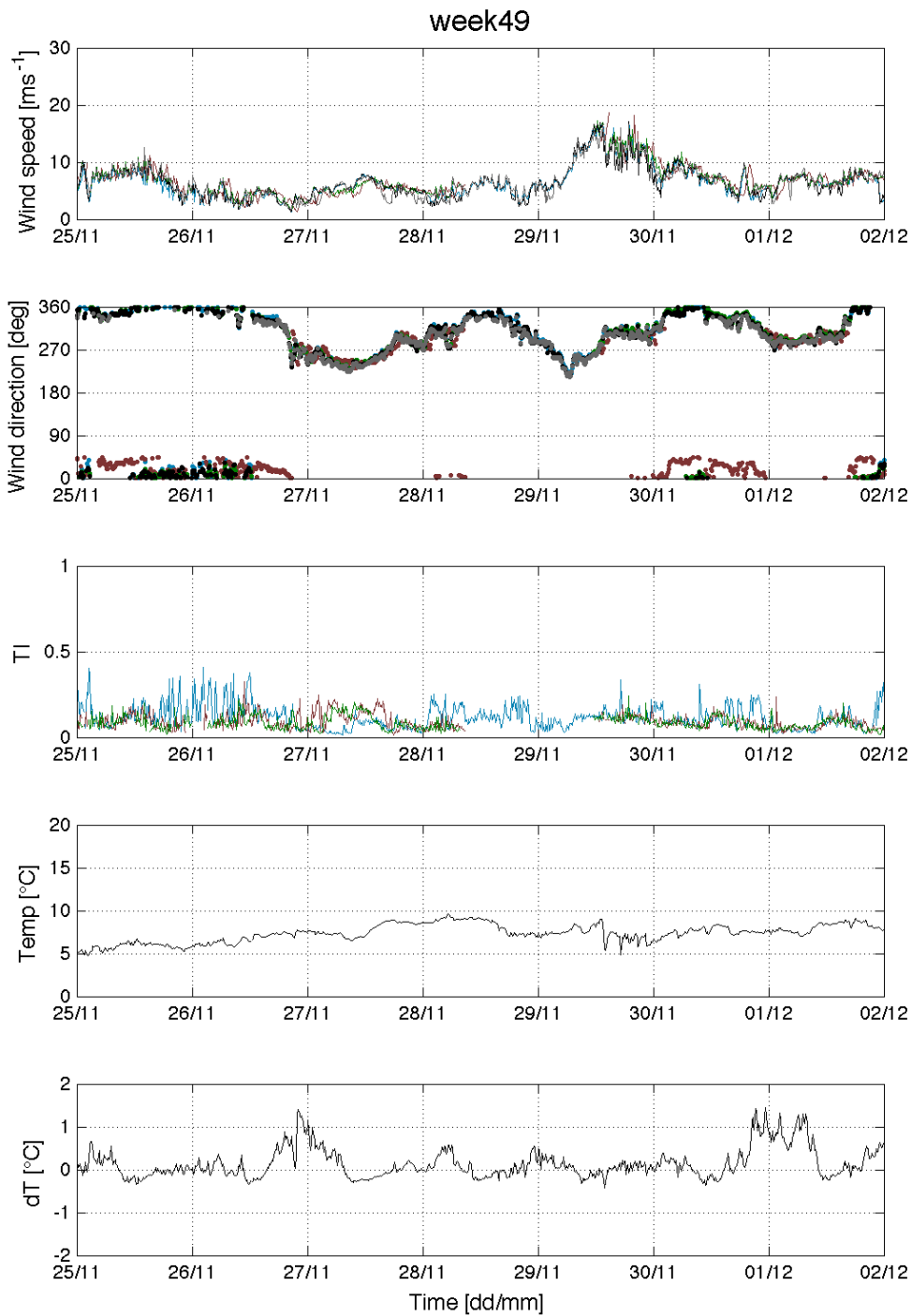


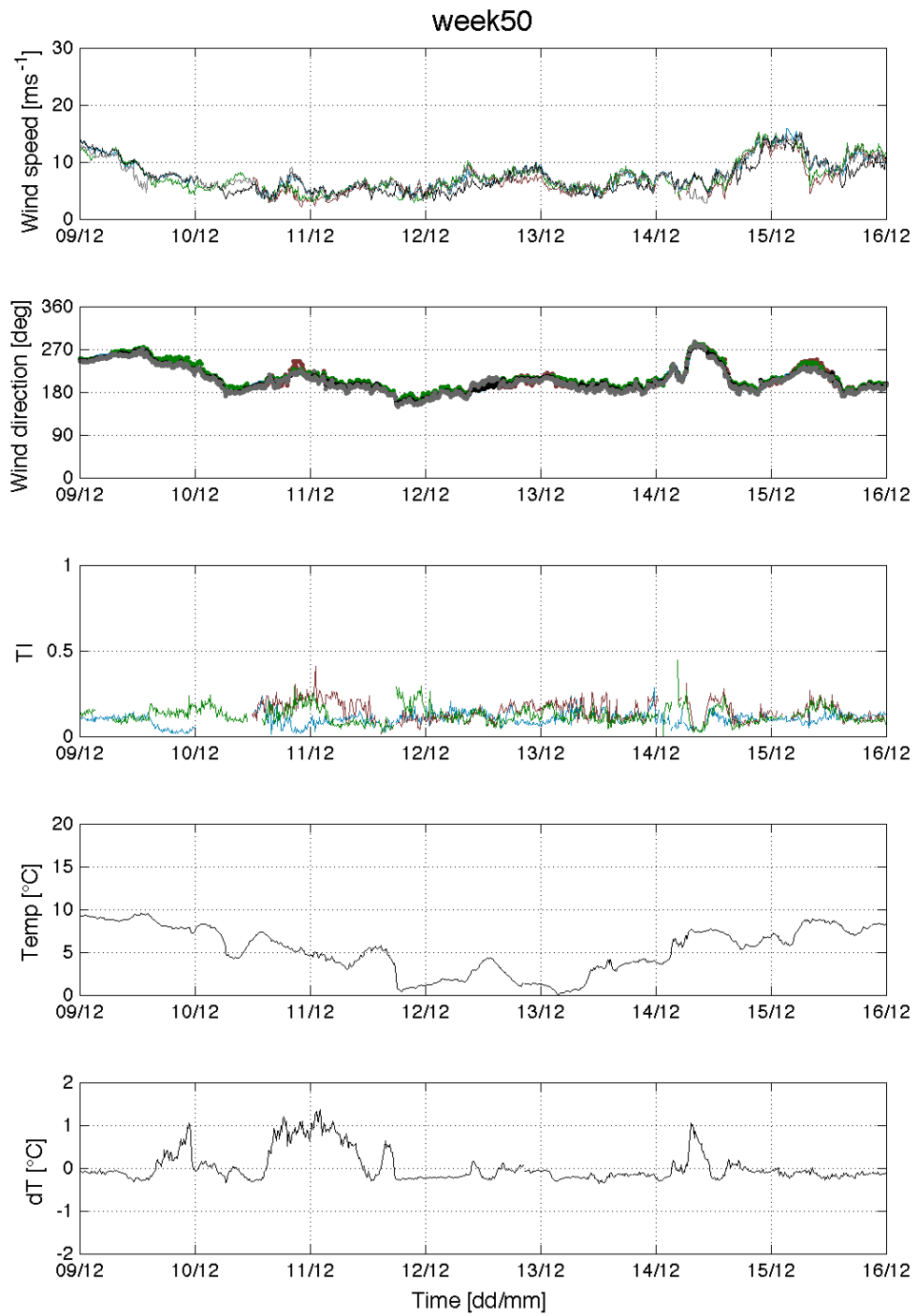


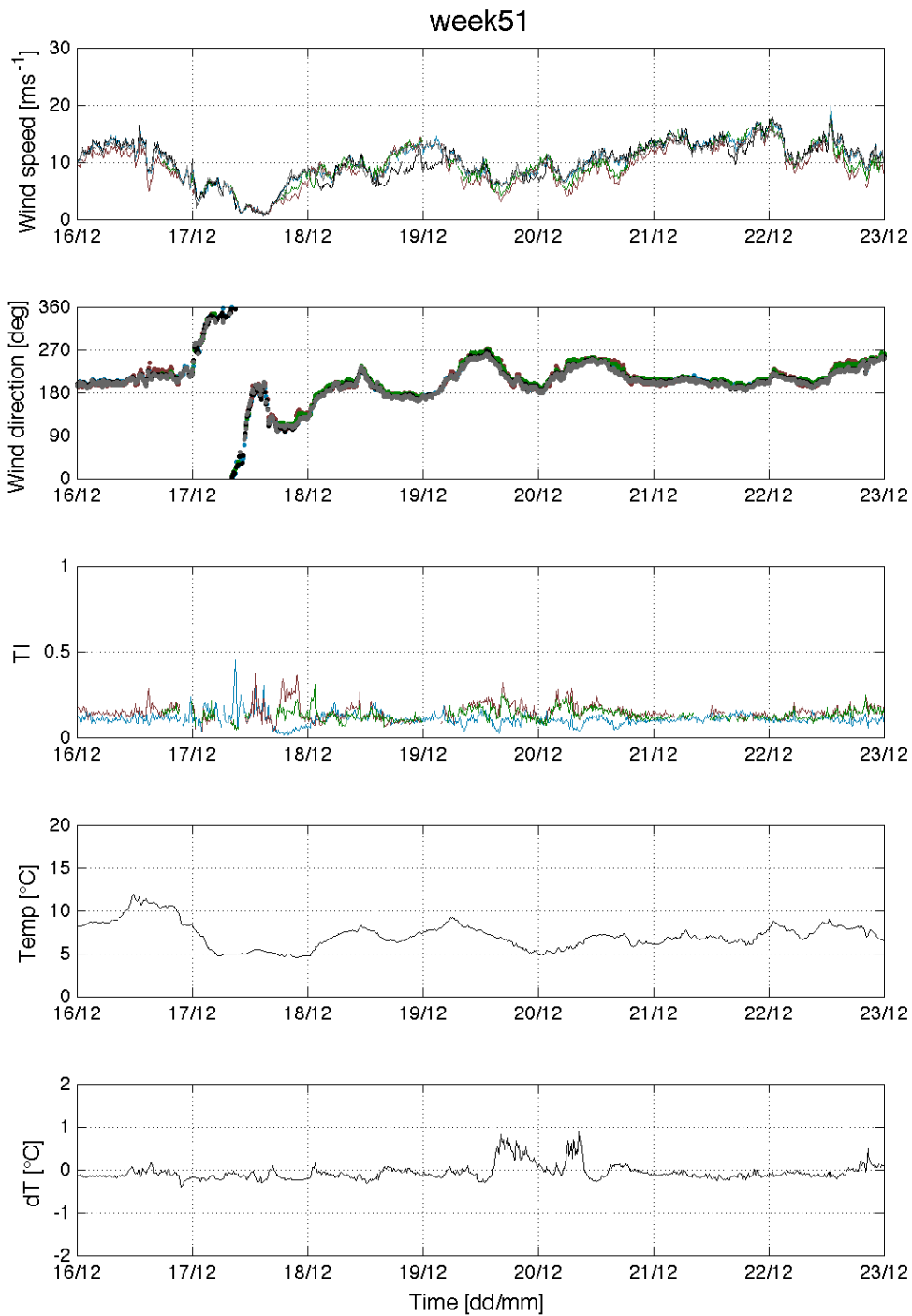


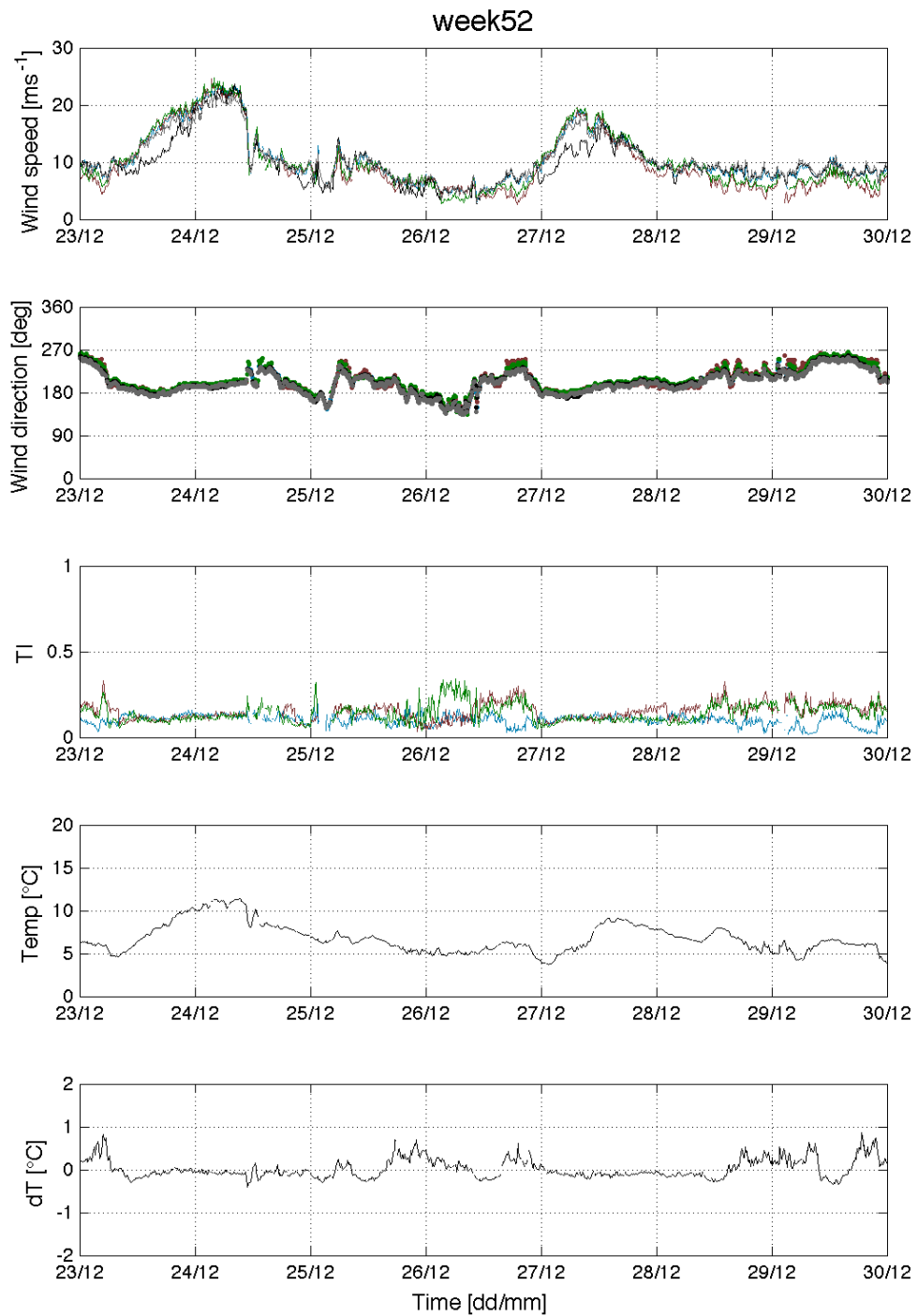


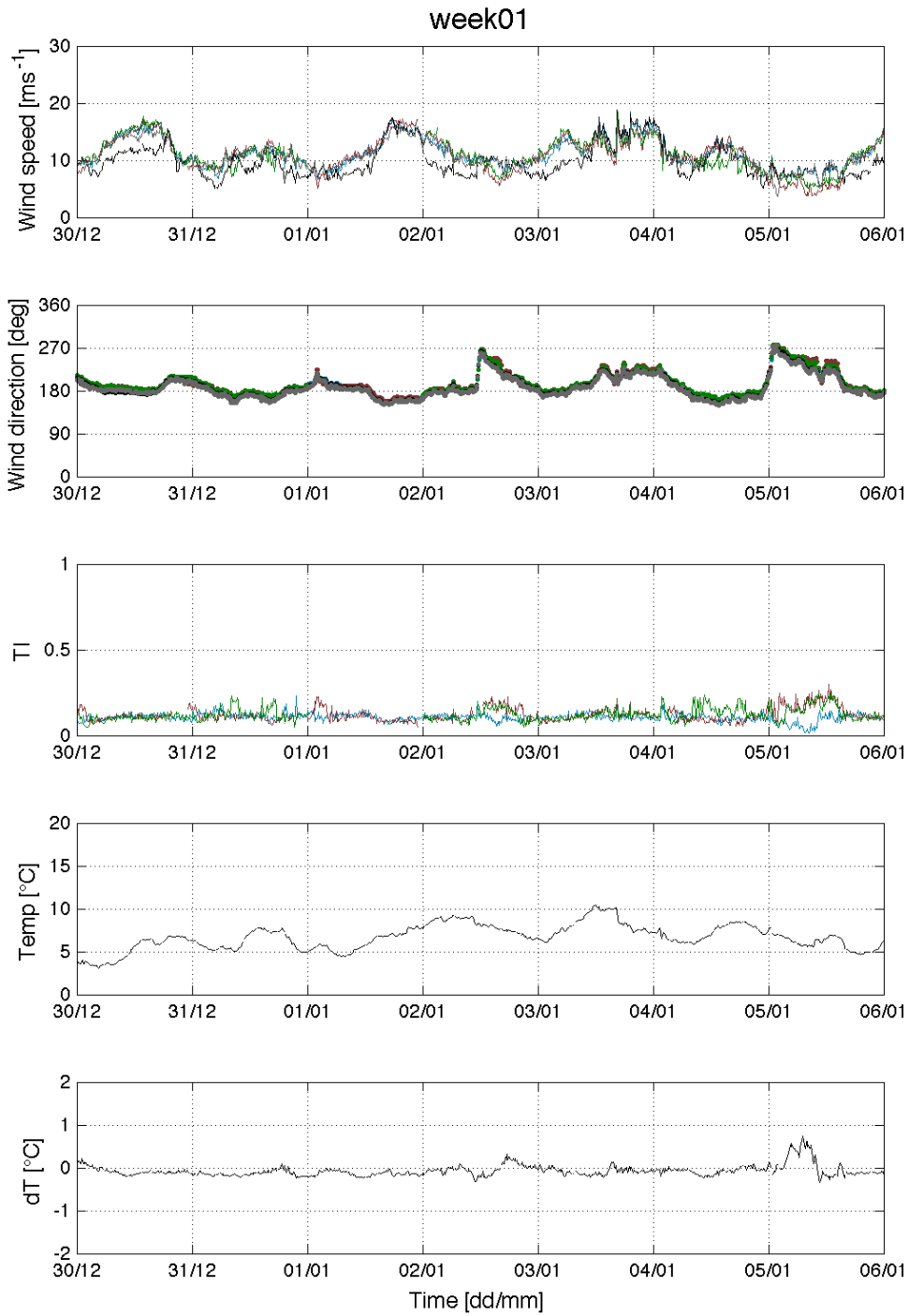


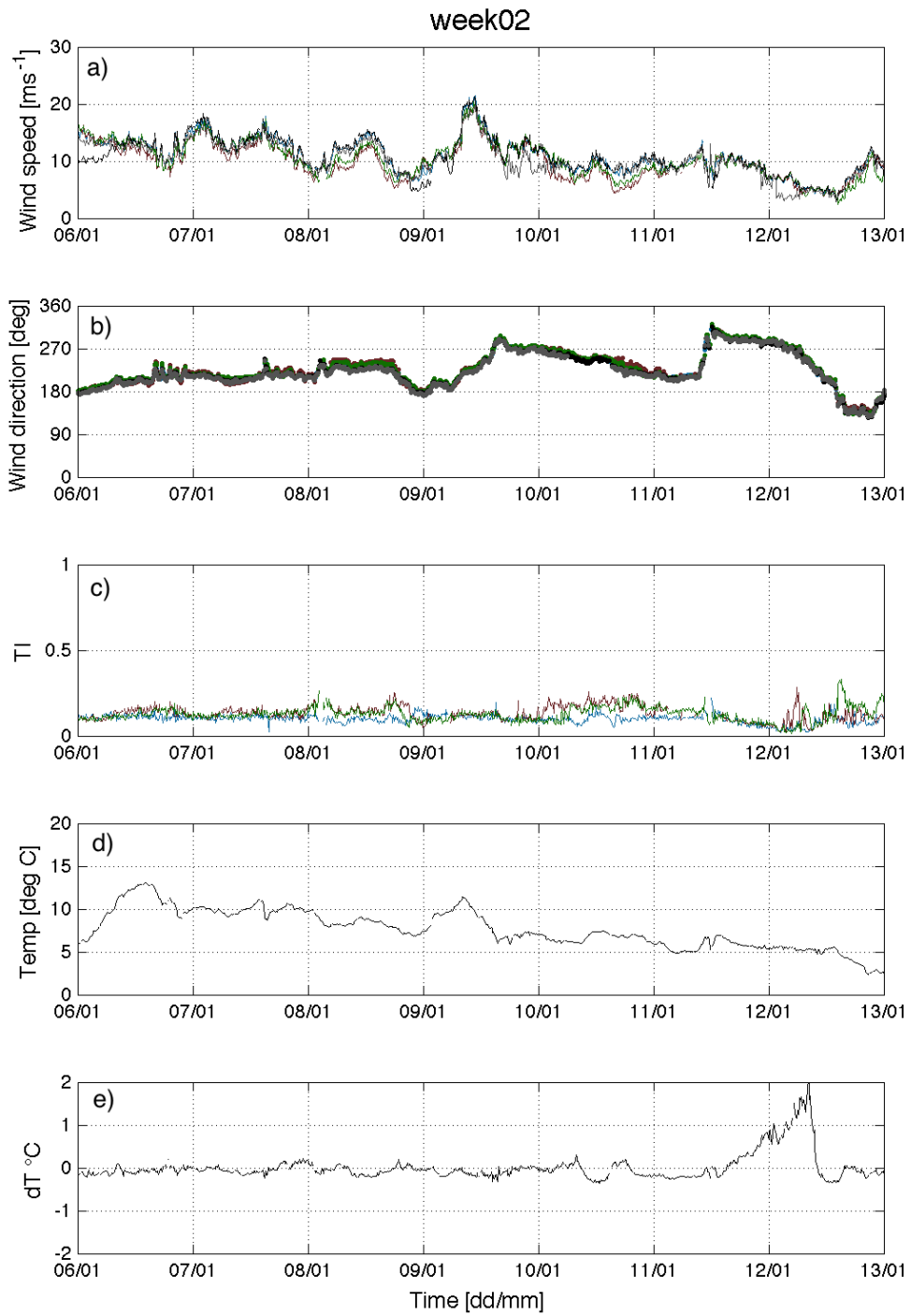


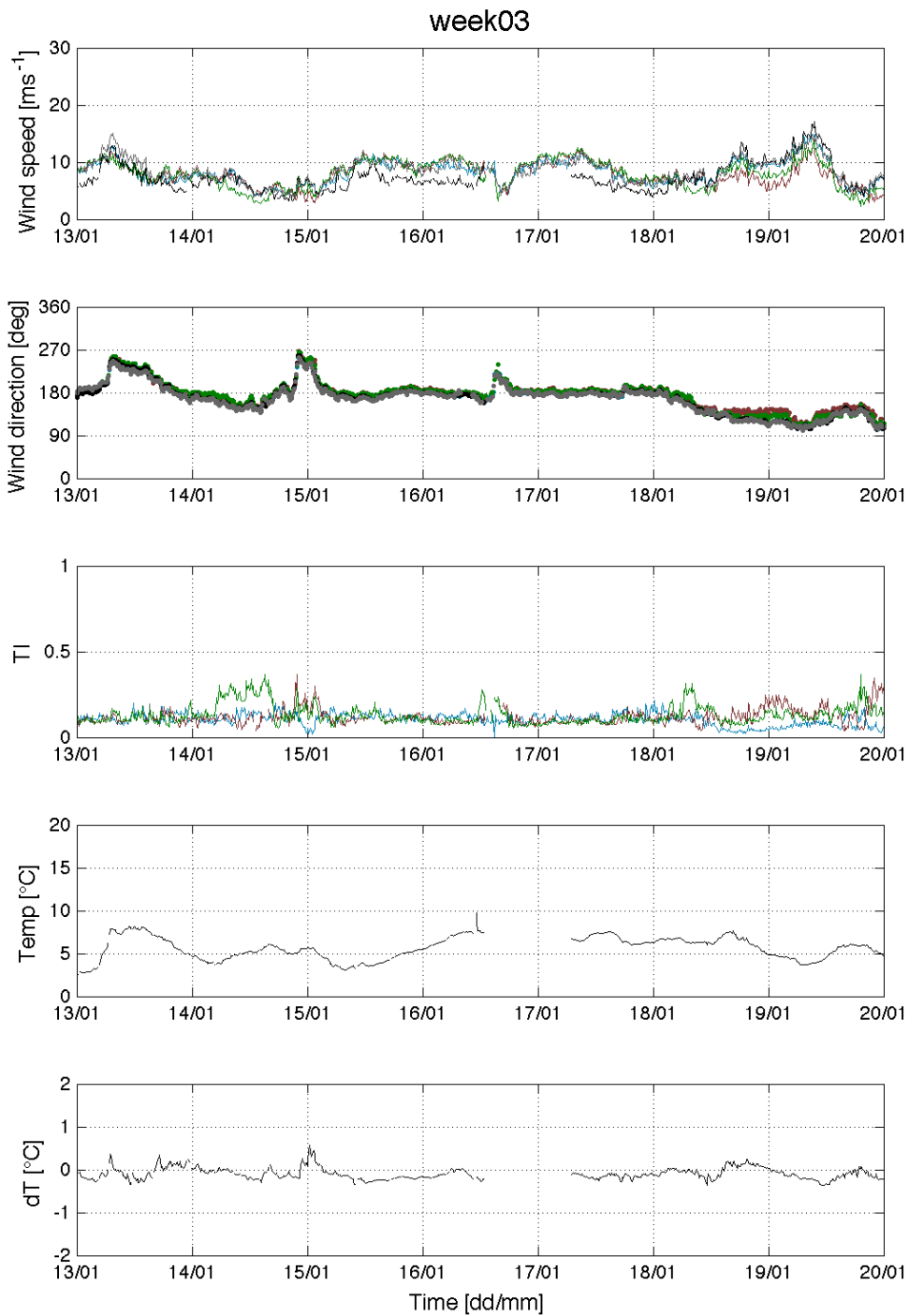


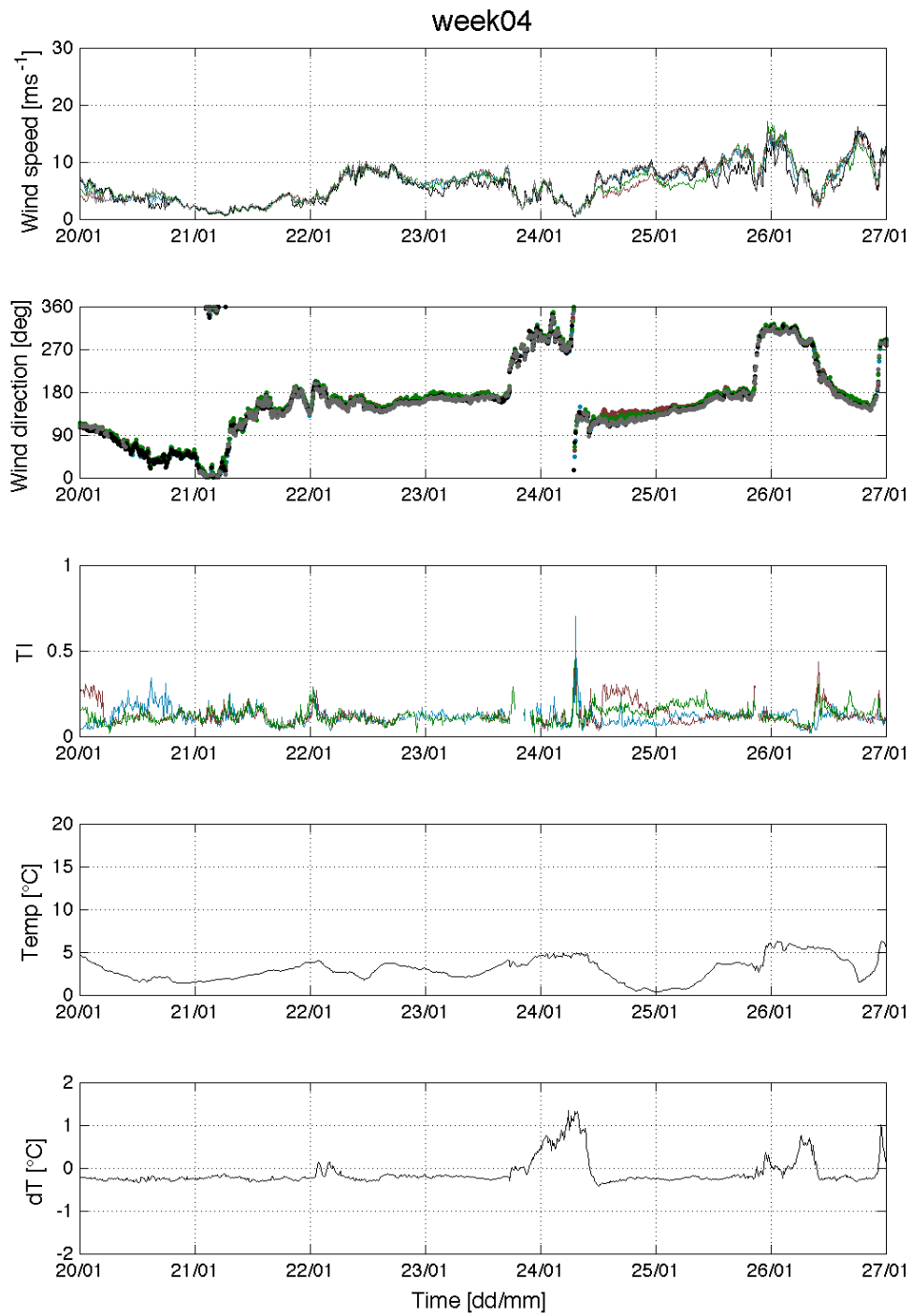


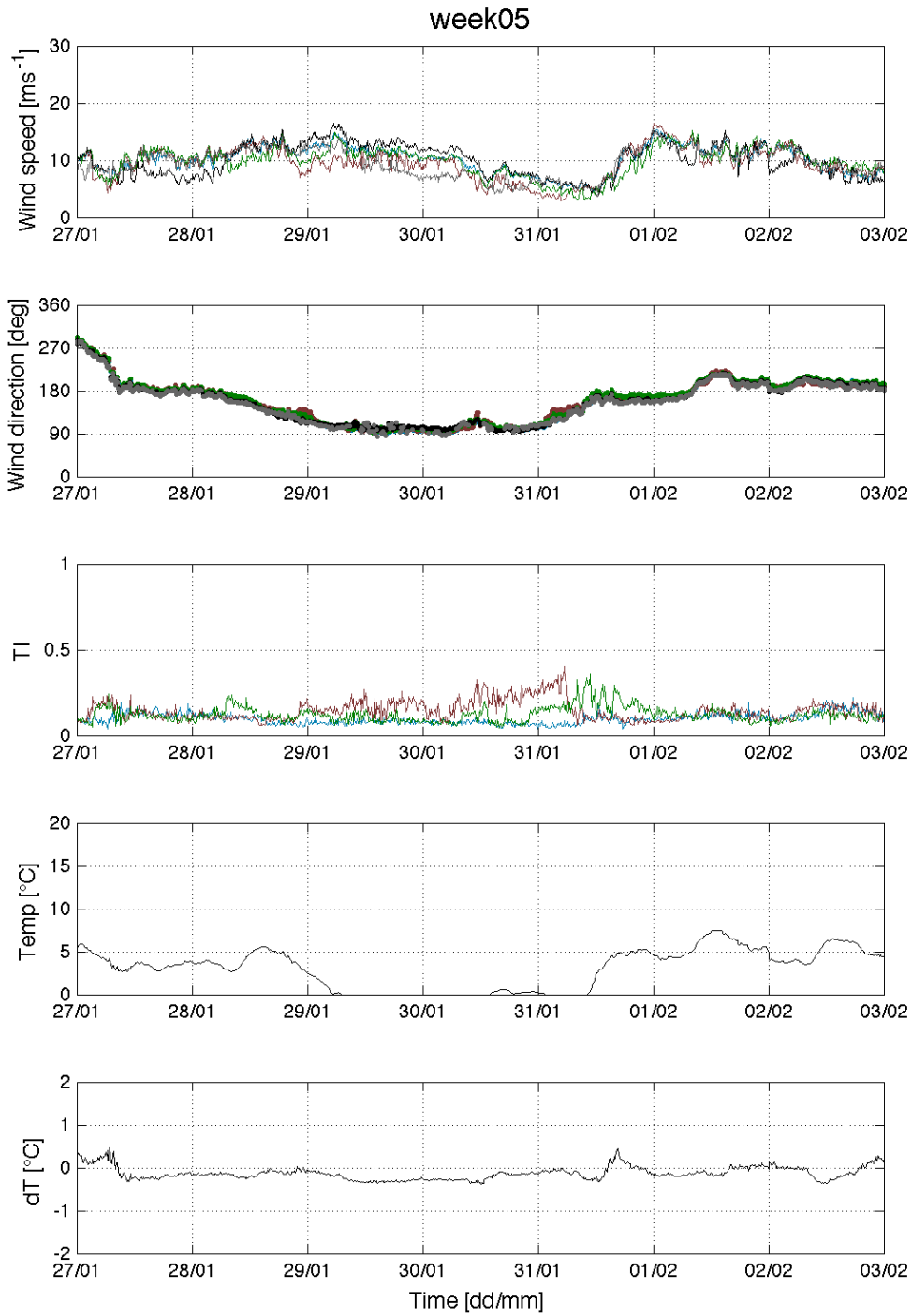


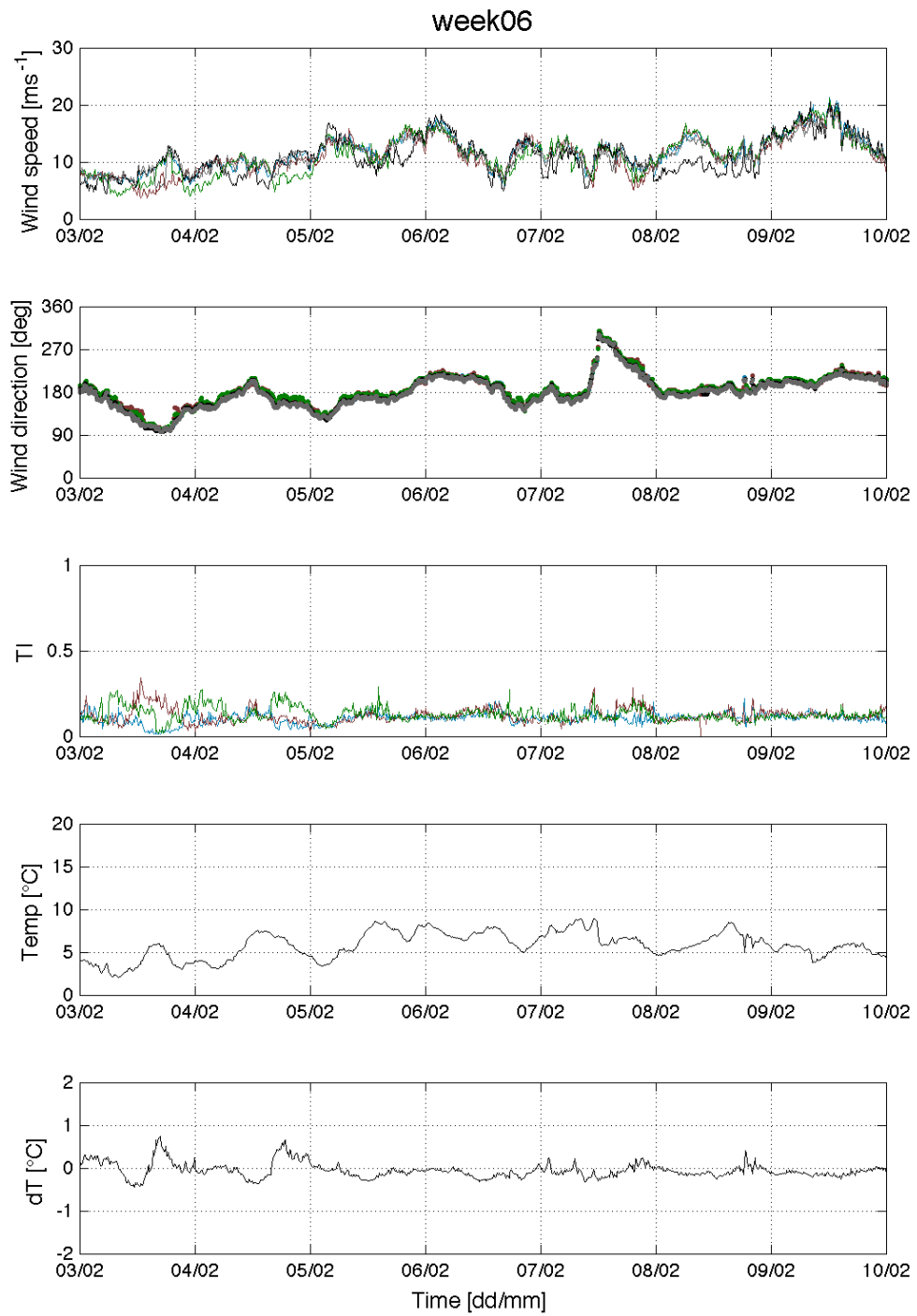


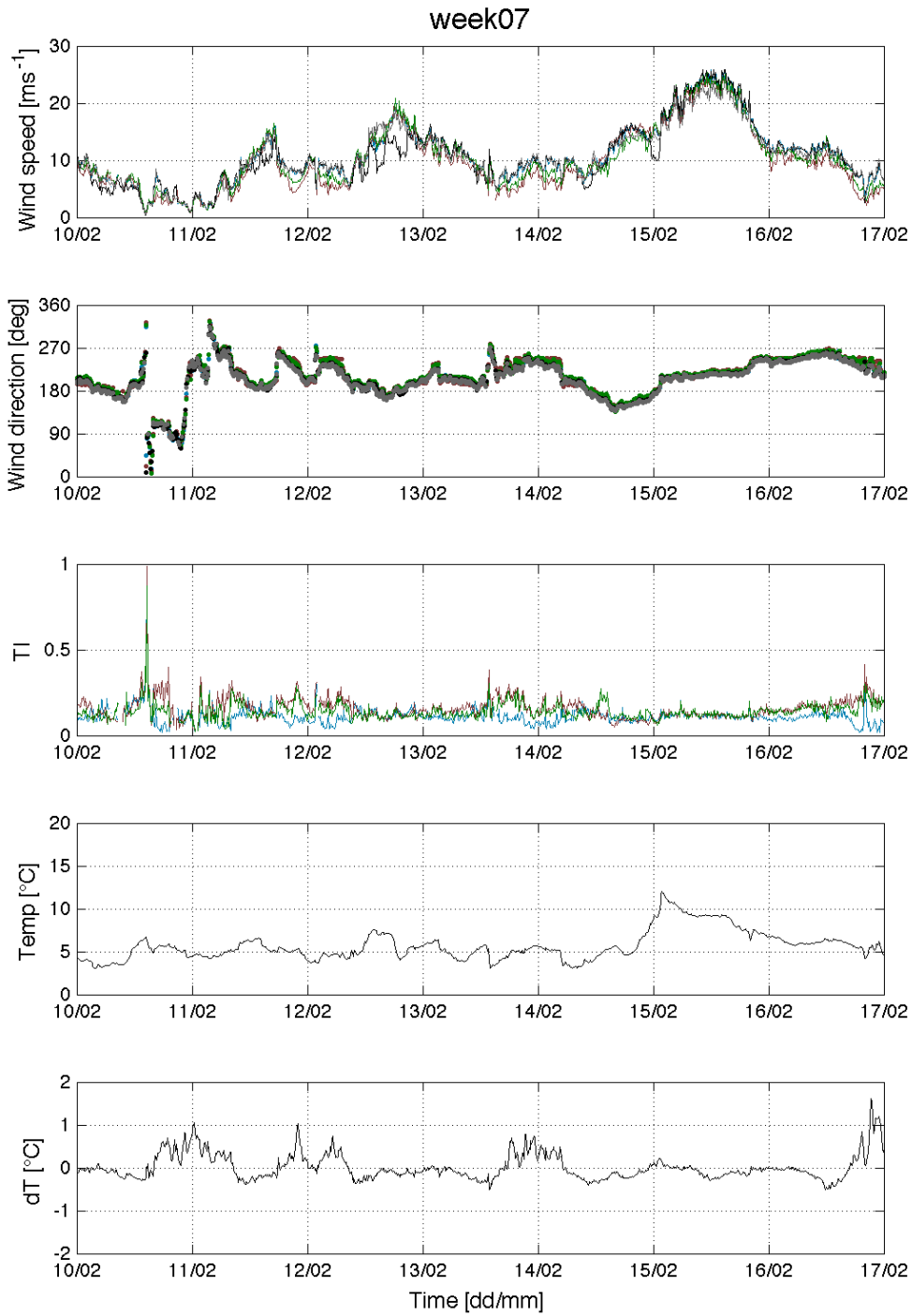


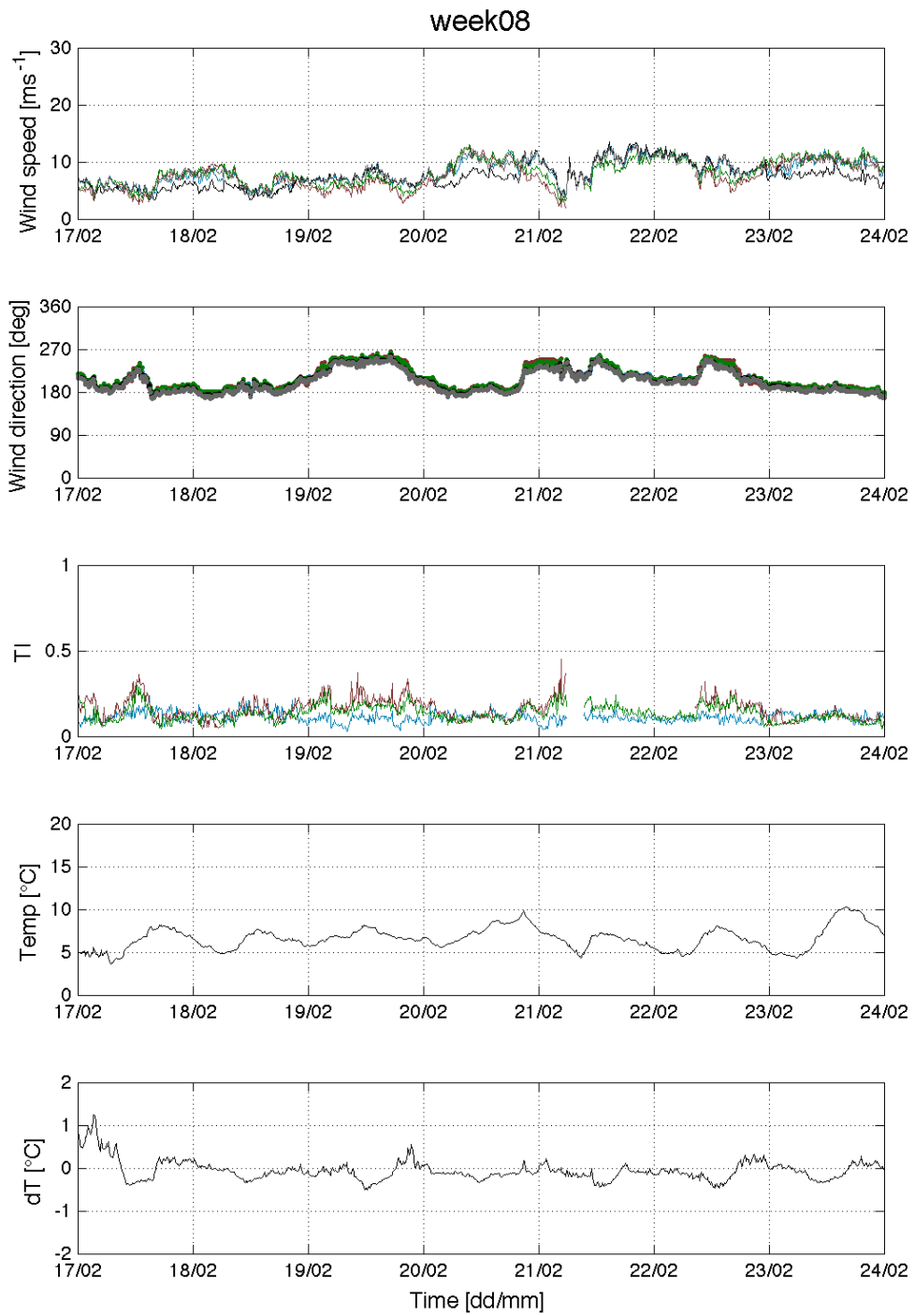


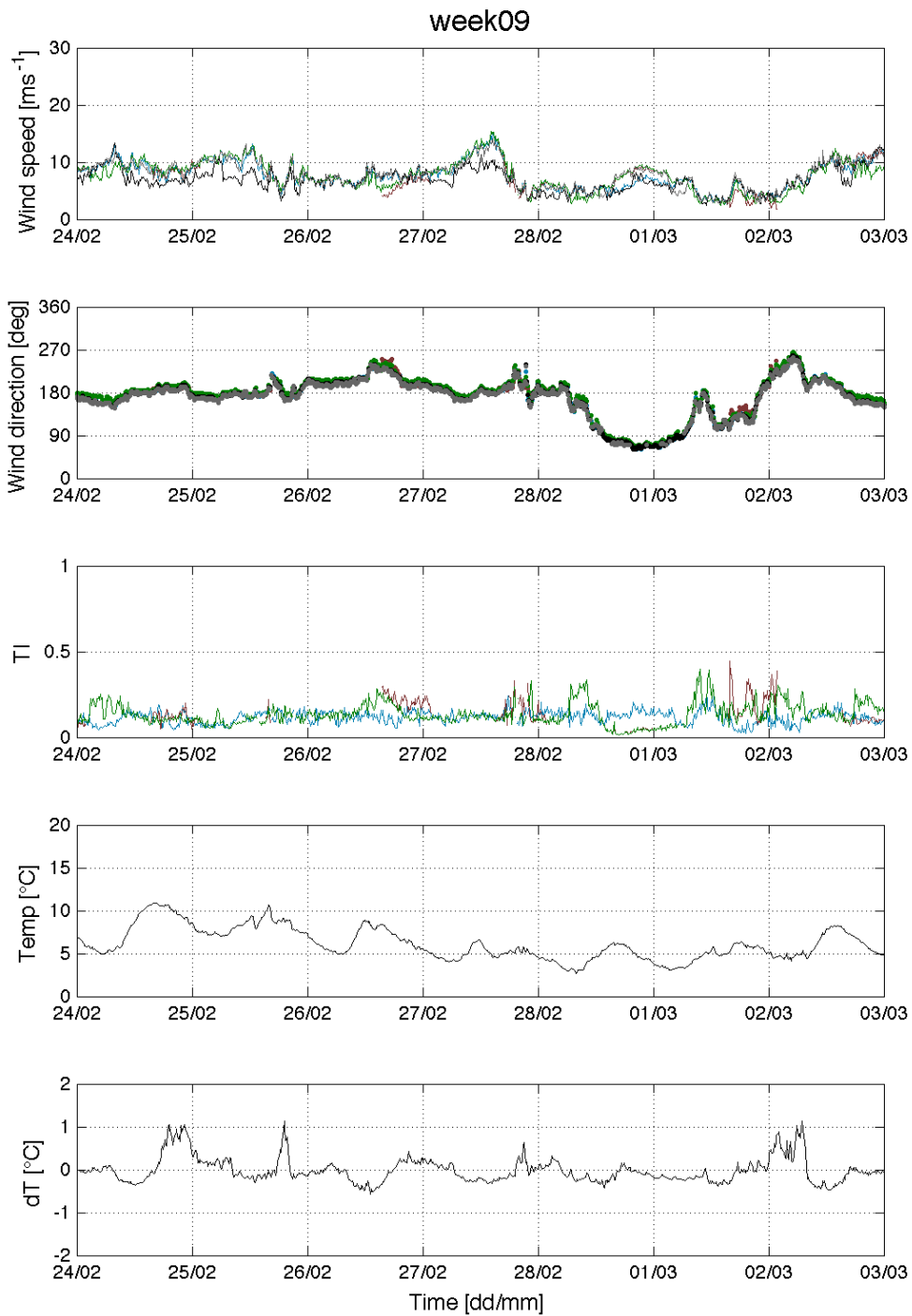


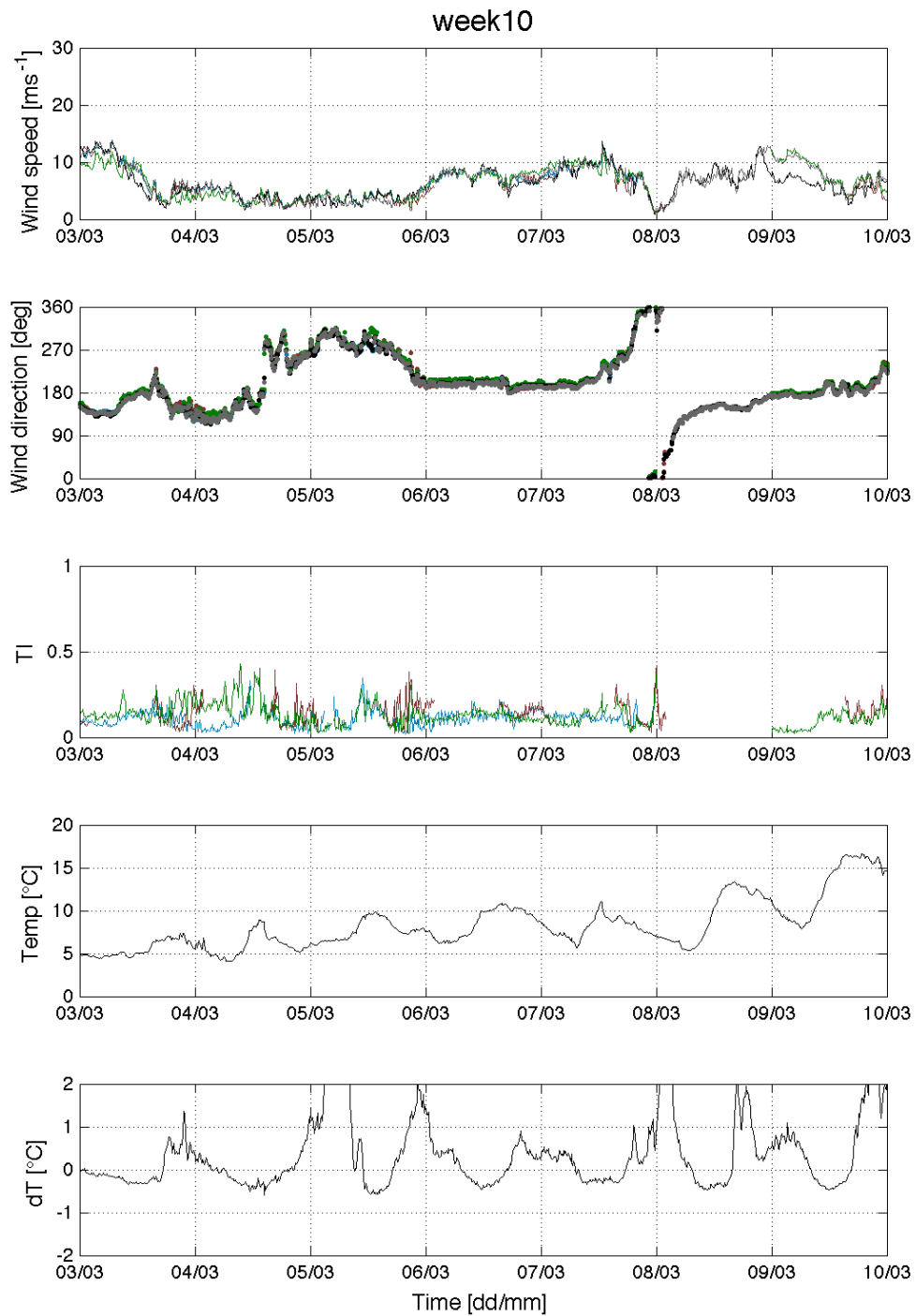


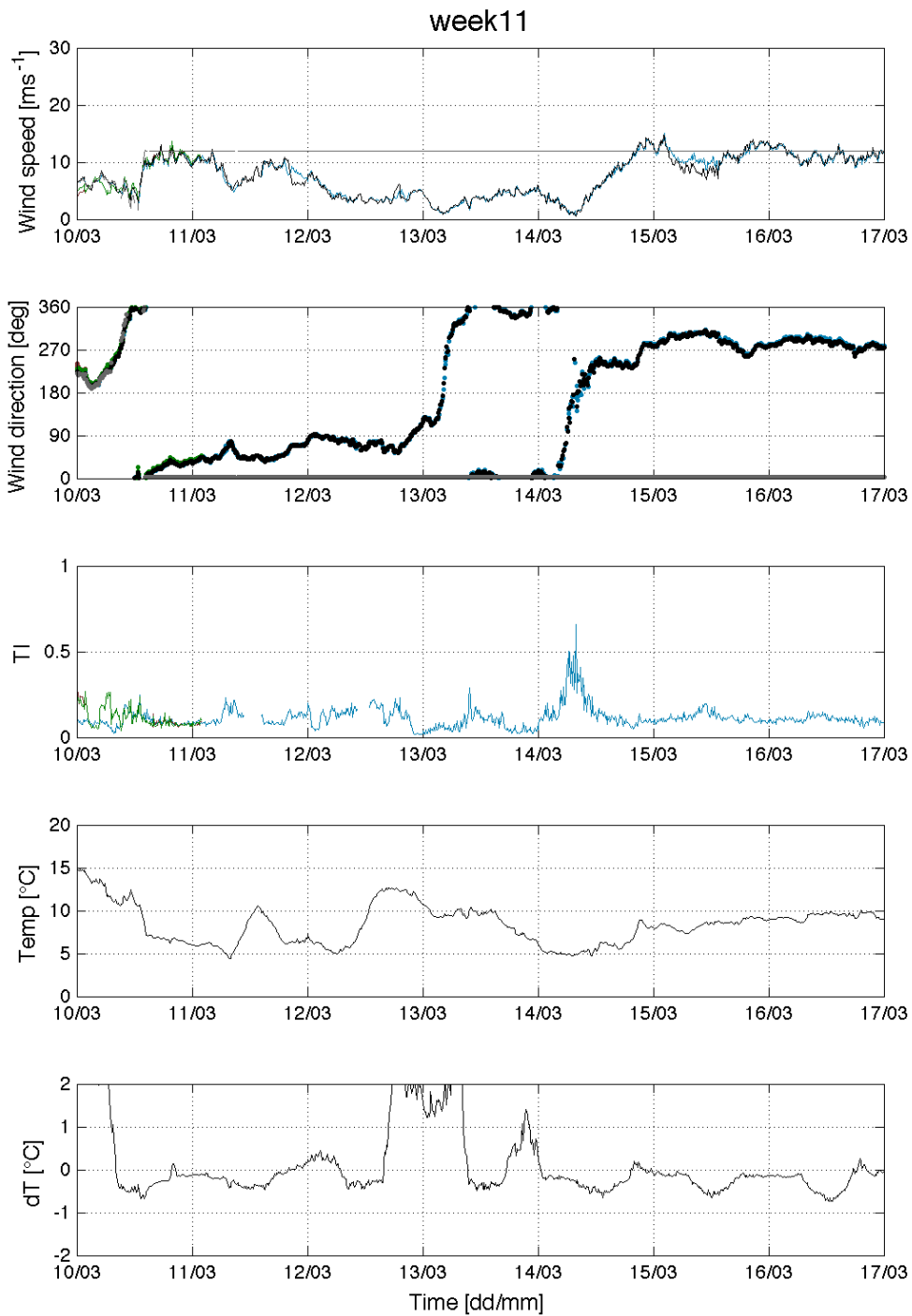


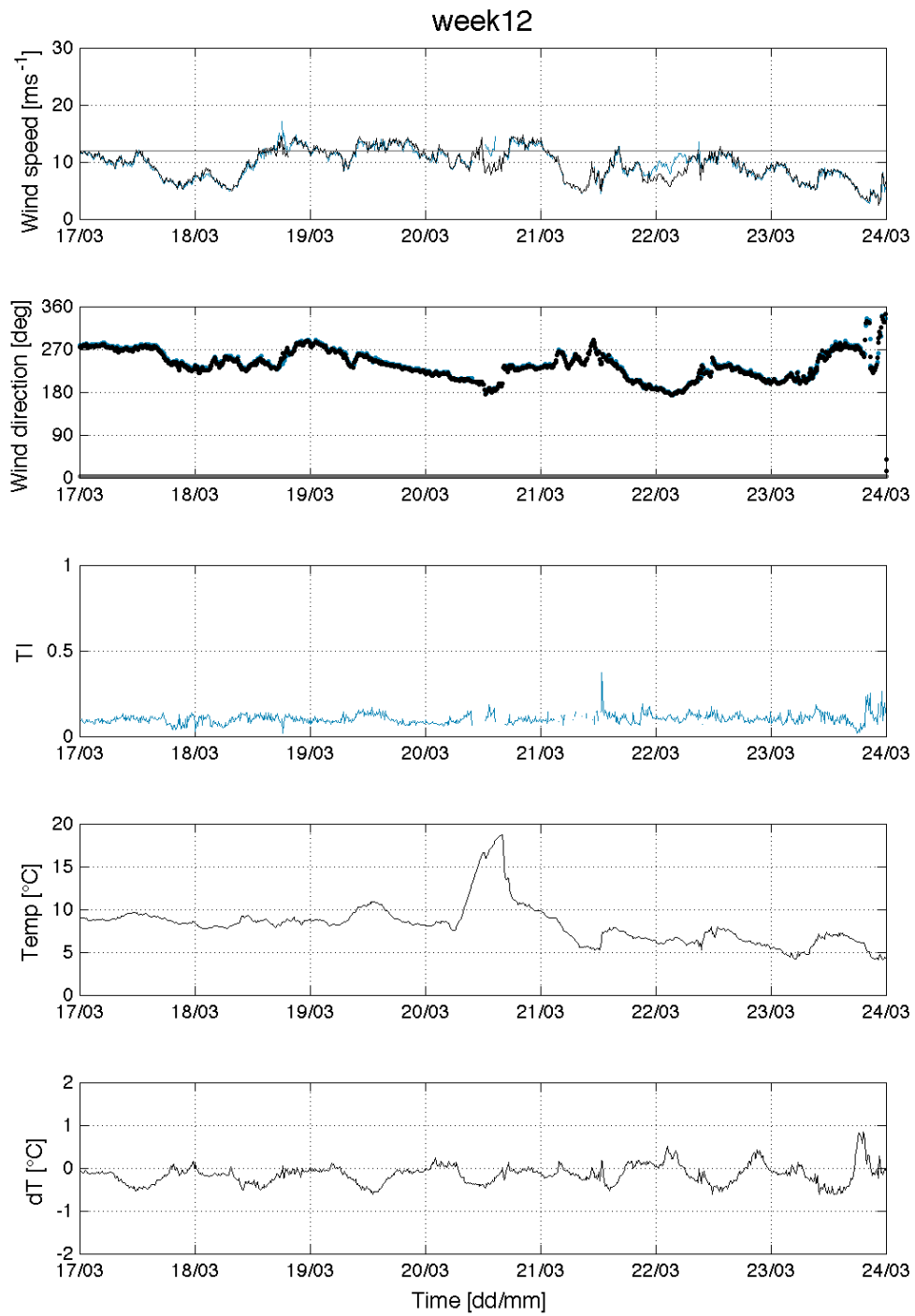


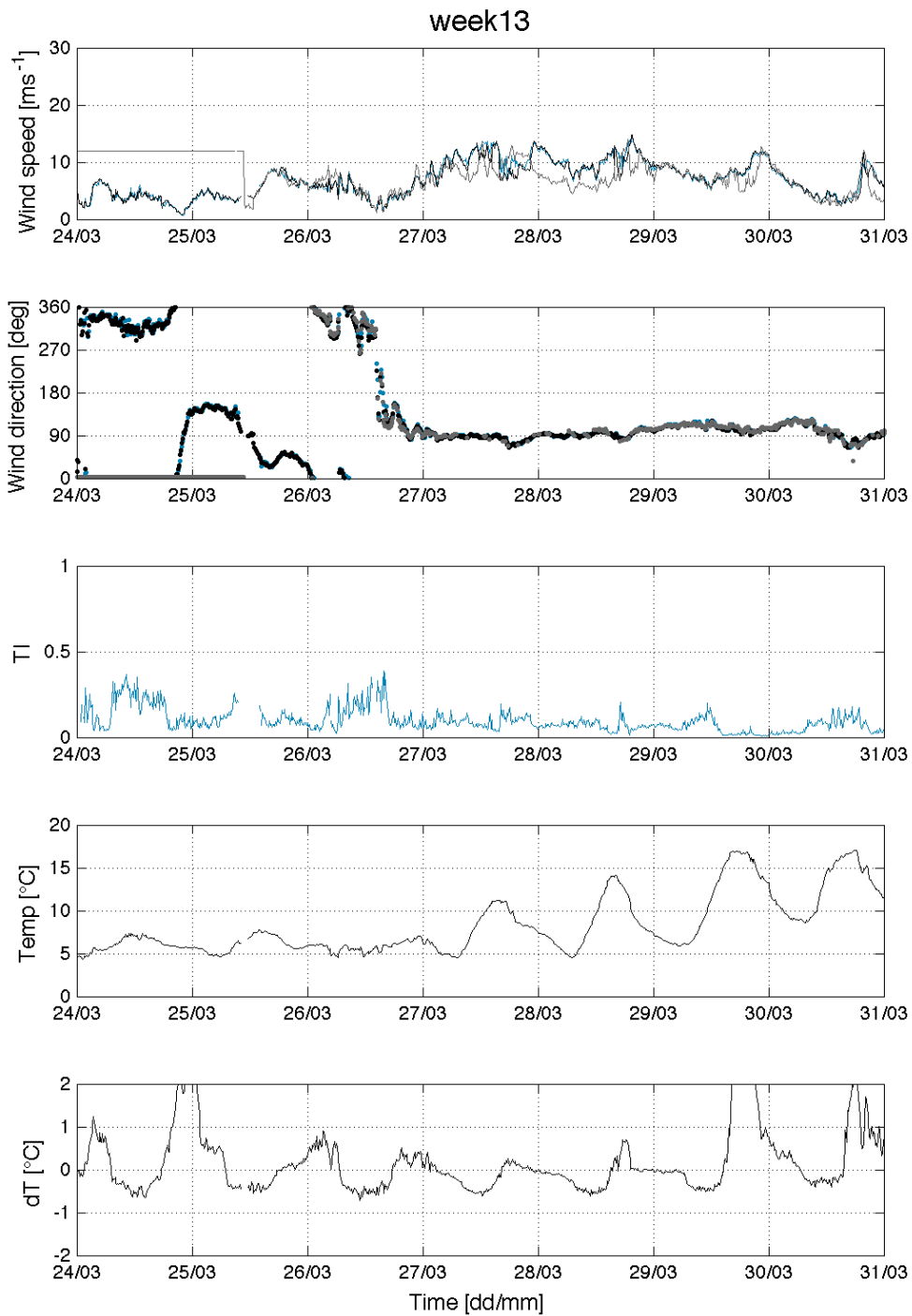


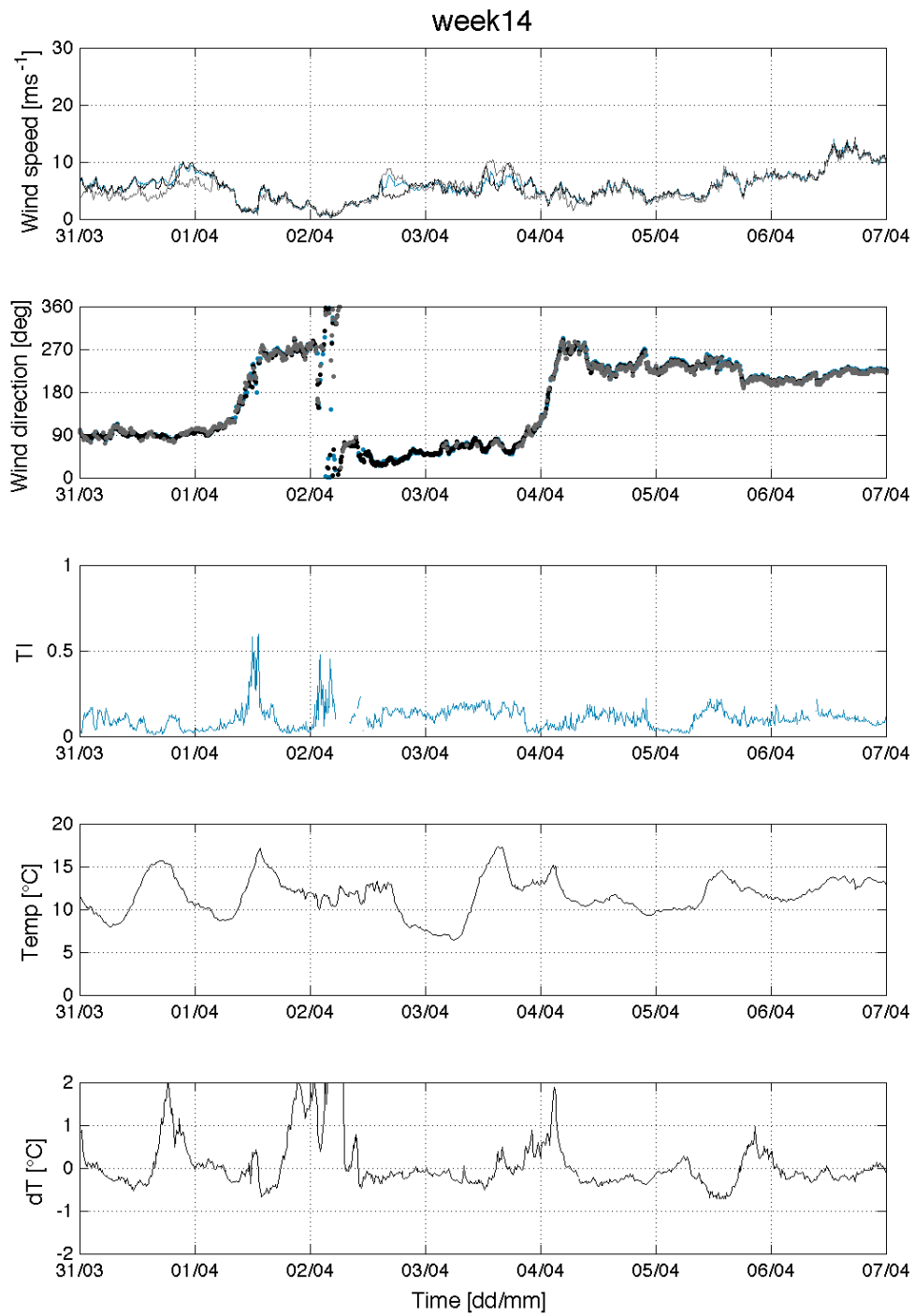


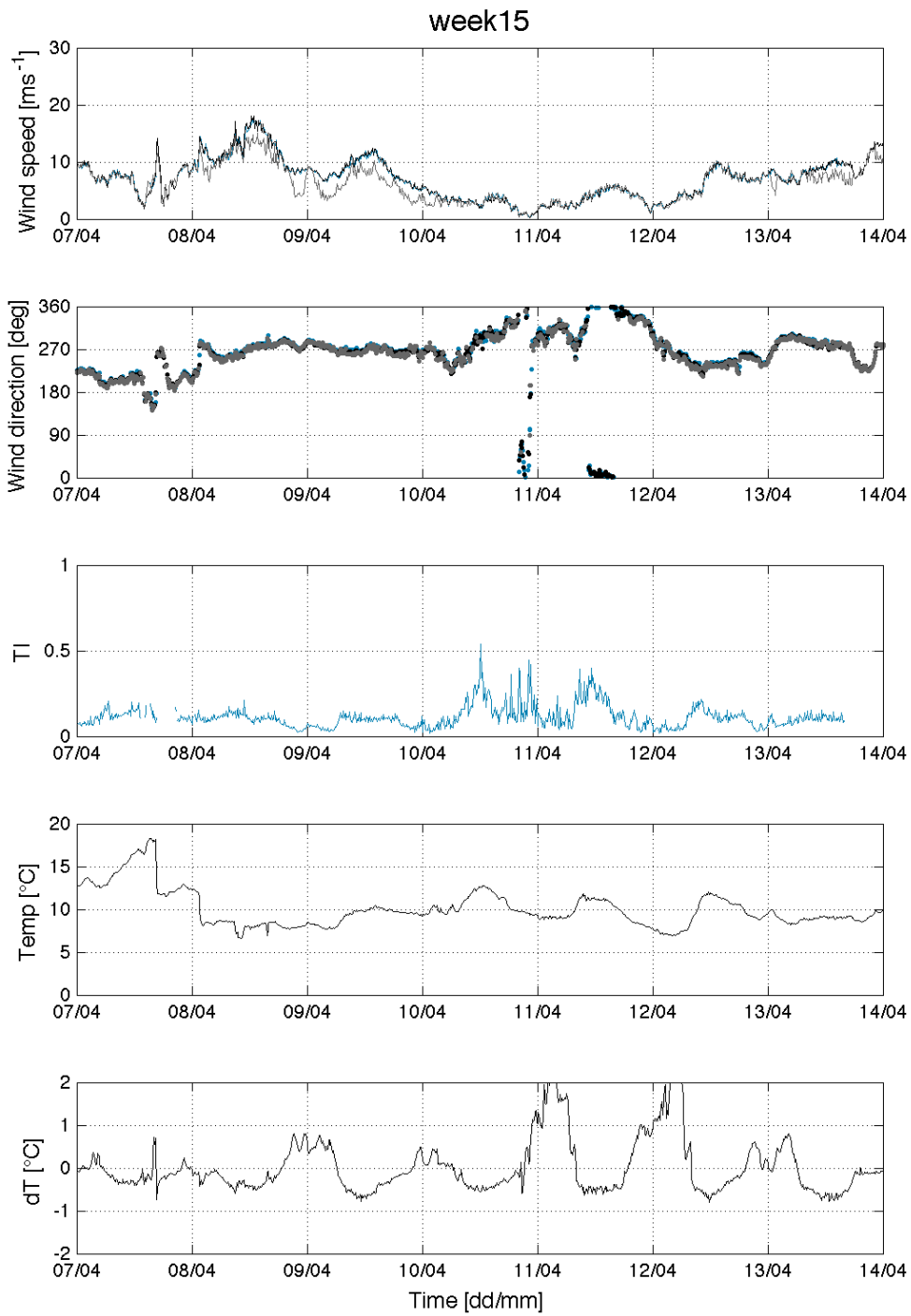


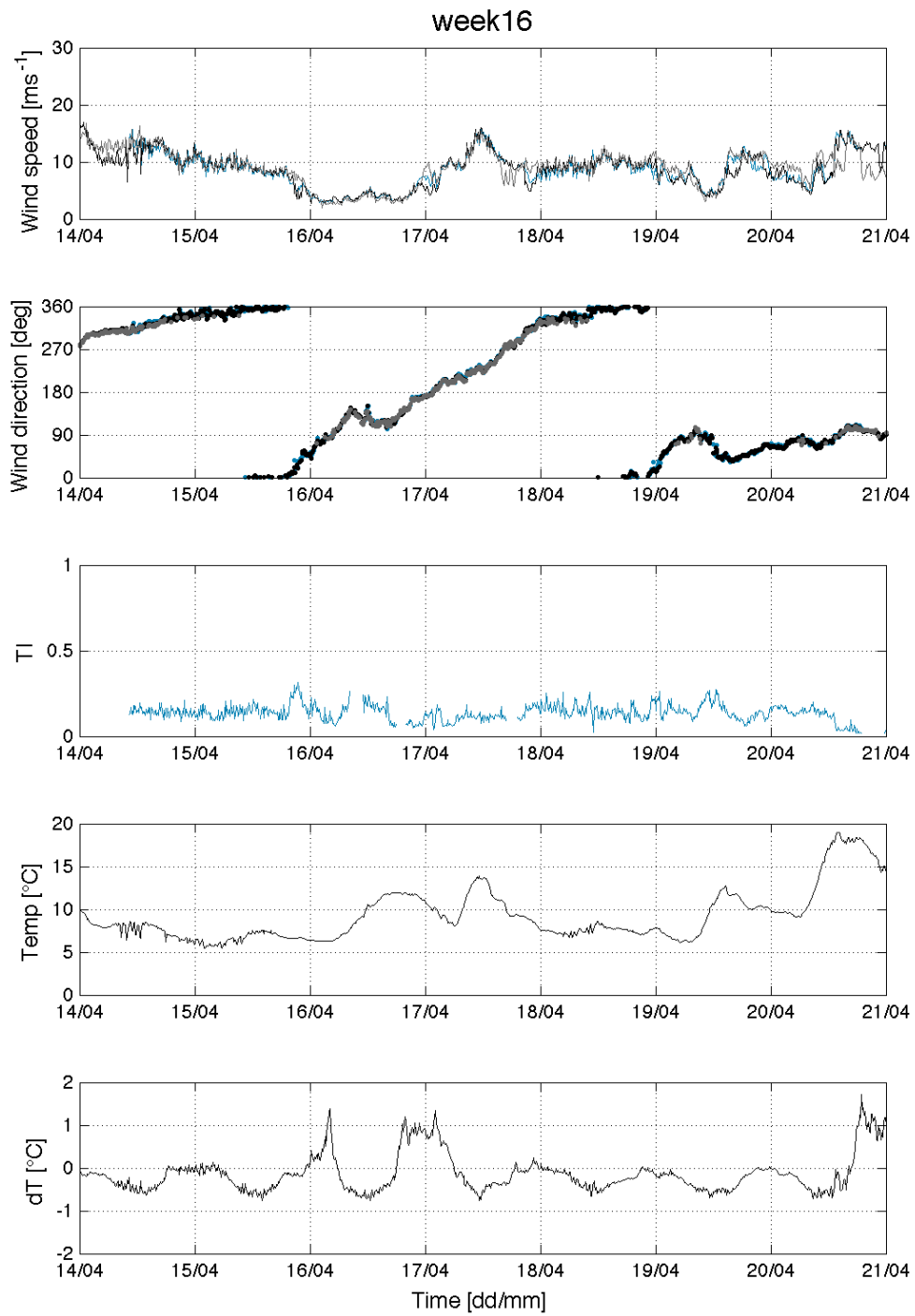


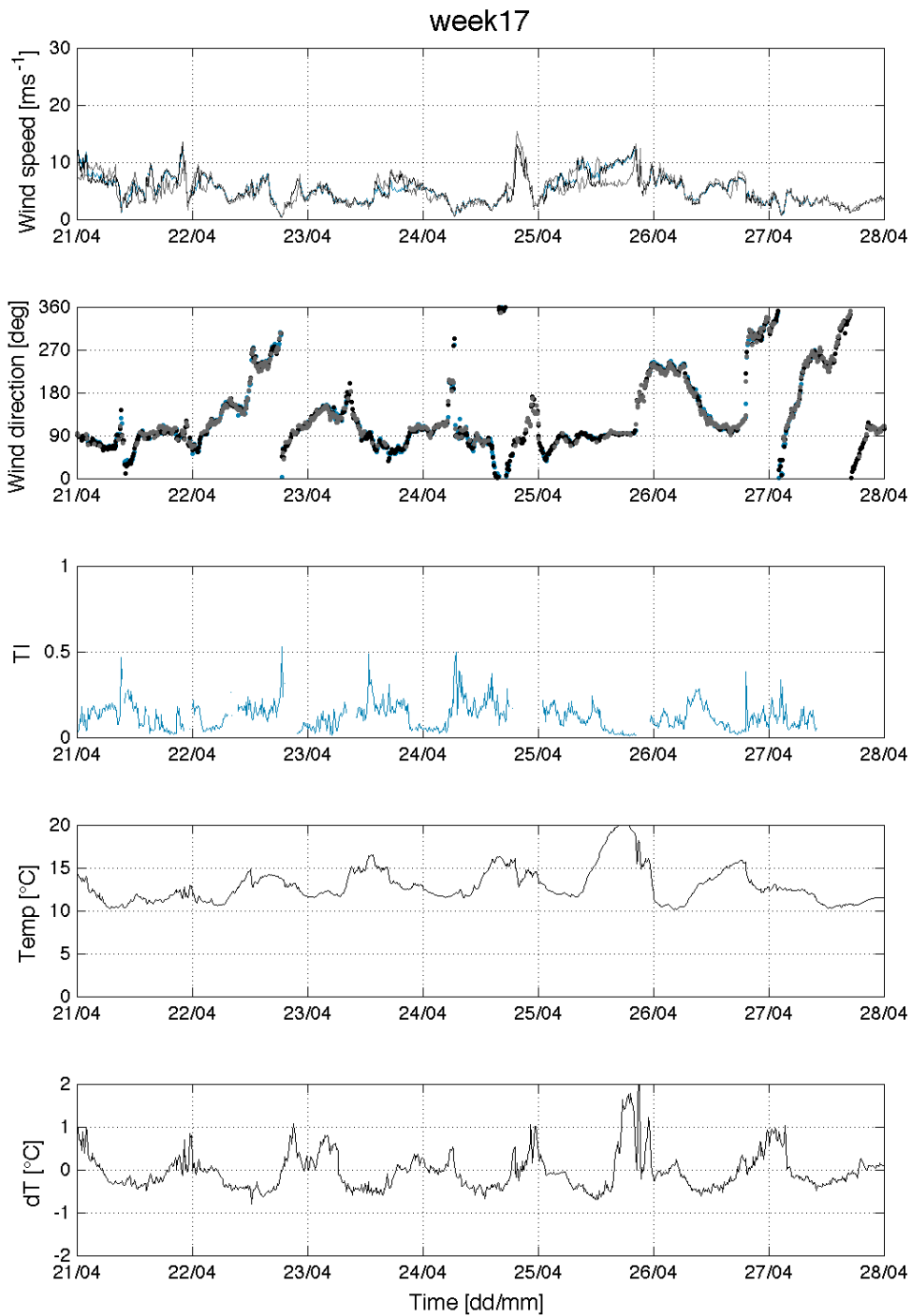


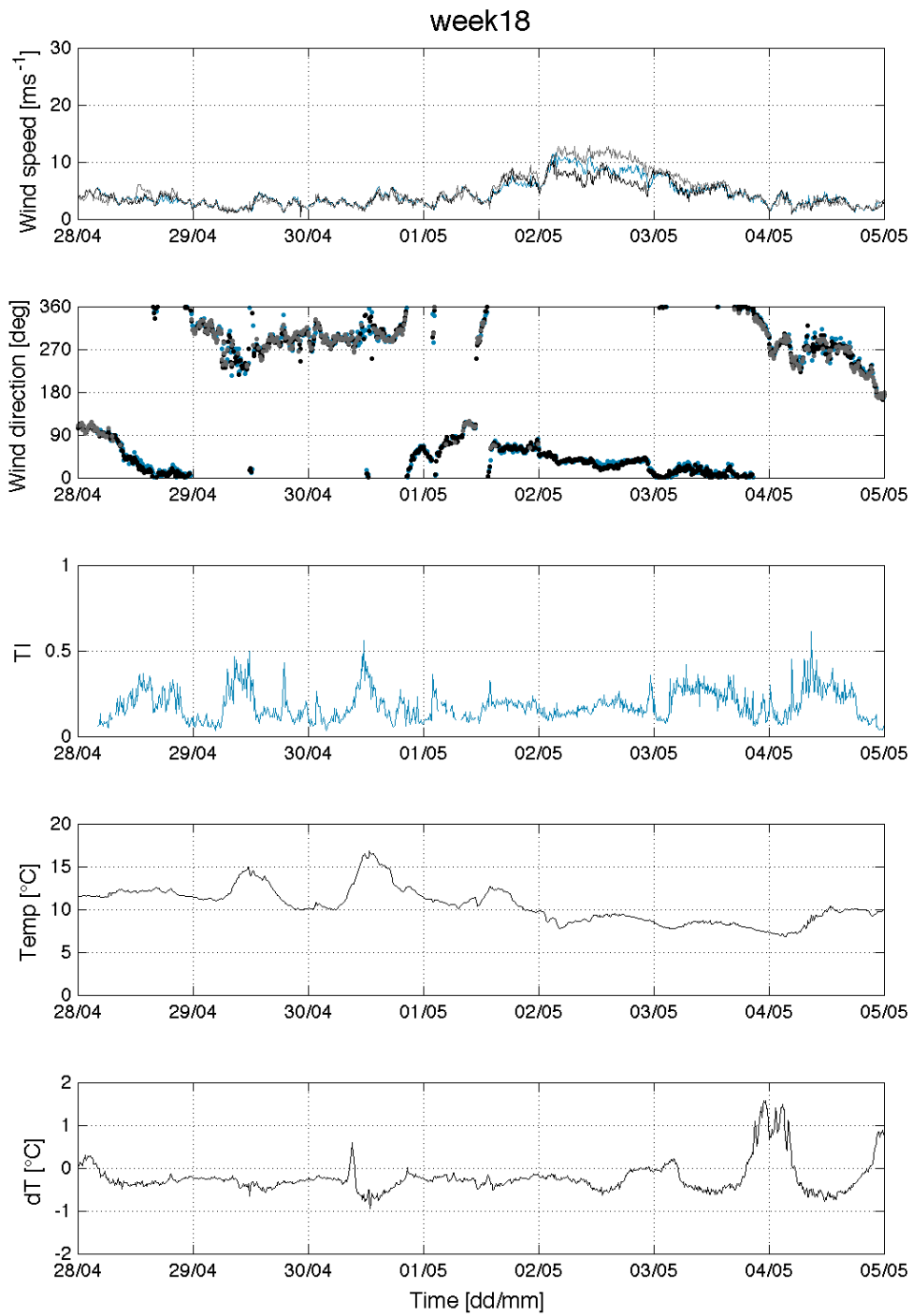


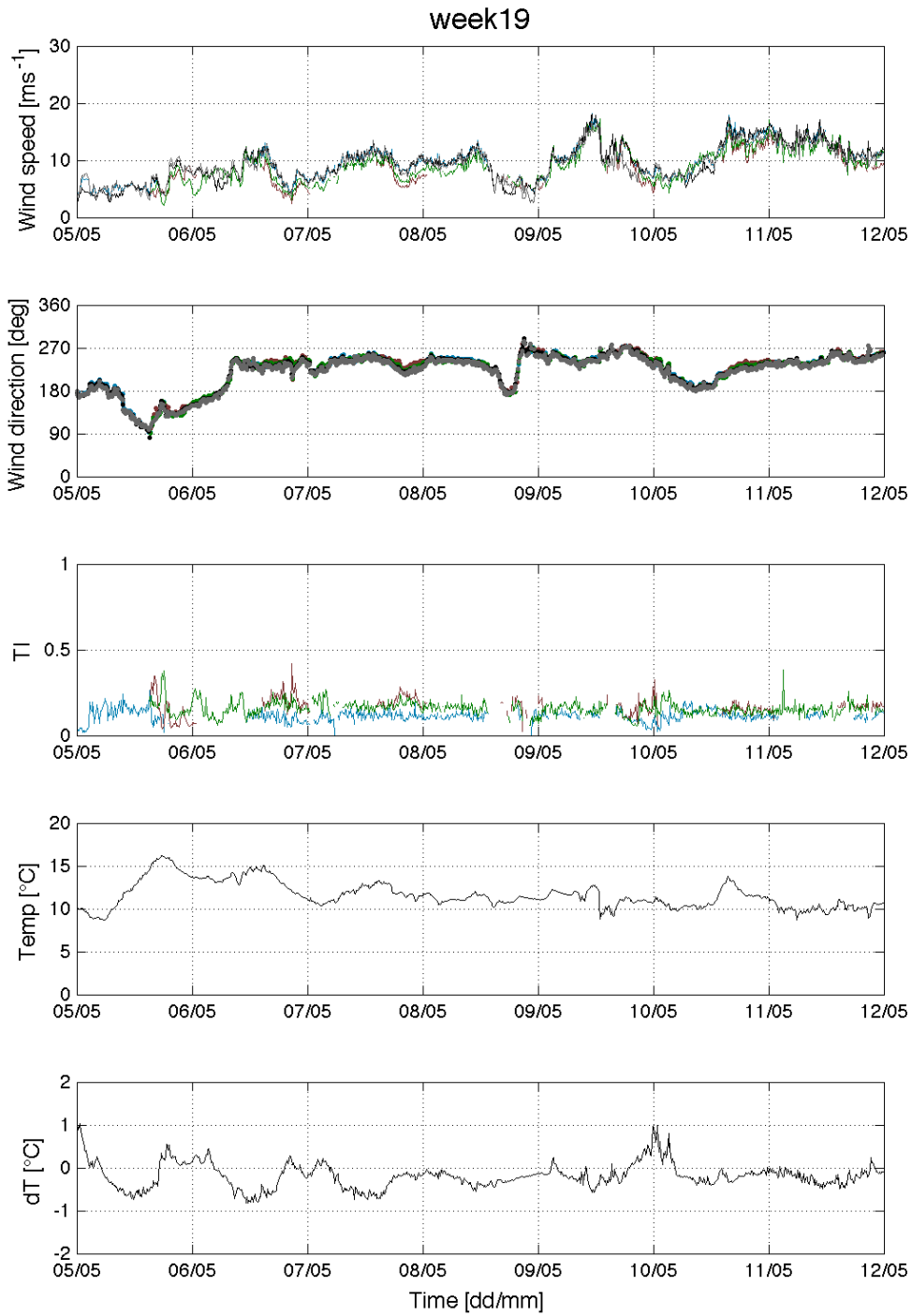












Bibliography

- Aitken, M. L., Banta, R. M., Pichugina, Y. L., and Lundquist, J. K. (2014). Quantifying Wind Turbine Wake Characteristics from Scanning Remote Sensor Data. *Journal of Atmospheric and Oceanic Technology*, 31(4):765–787.
- Aitken, M. L., Rhodes, M. E., and Lundquist, J. K. (2012). Performance of a Wind-Profiling Lidar in the Region of Wind Turbine Rotor Disks. *Journal of Atmospheric and Oceanic Technology*, 29(3):347–355.
- Alblas, L., Bierbooms, W., and Veldkamp, D. (2014). Power output of offshore wind farms in relation to atmospheric stability. *Journal of Physics: Conference Series*, 555(1):012004.
- Banta, R. M., Pichugina, Y. L., Brewer, W. A., Lundquist, J. K., Kelley, N. D., Sandberg, S. P., Alvarez II, R. J., Hardesty, R. M., and Weickmann, A. M. (2015). 3D Volumetric Analysis of Wind Turbine Wake Properties in the Atmosphere Using High-Resolution Doppler Lidar. *Journal of Atmospheric and Oceanic Technology*, 32(5):904–914.
- Barthelmie, R. J., Hansen, K. S., and Pryor, S. C. (2013). Meteorological Controls on Wind Turbine Wakes. *Proceedings of the IEEE*, 101(4):1010–1019.
- Chamorro, L. P. and Porté-Agel, F. (2011). Turbulent Flow Inside and Above a Wind Farm: A Wind-Tunnel Study. *Energies*, 4(11):1916–1936.
- Christakos, K. (2013). *Characterization of the coastal marine atmospheric boundary layer (MABL) for wind energy applications*. University of Bergen. (Unpublished Master’s thesis).

- Eecen, P. and Verhoef, J. (2007). EWTW Meteorological database Description June 2003 - May 2007. Technical report. ECN Wind Energy.
- Ehrlich, R. (2013). *Renewable Energy; a First Course*. CRC Press.
- Fitch, A. C., Olson, J. B., Lundquist, J. K., Dudhia, J., Gupta, A. K., Michalakes, J., and Barstad, I. (2012). Local and Mesoscale Impacts of Wind Farms as Parameterized in a Mesoscale NWP Model. *Monthly Weather Review*, 140(9):3017–3038.
- Foken, T. (2008). *Micrometeorology*. Springer, Berlin, Heidelberg.
- Global Wind Energy Council (GWEC) (2015). Global wind report - Annual market update. Technical report. URL http://www.gwec.net/wp-content/uploads/vip/GWEC-Global-Wind-2015-Report_April-2016_22_04.pdf. Last accessed on 28.May.2016.
- Gryning, S.-E., Batchvarova, E., Brümmner, B., Jørgensen, H., and Larsen, S. (2007). On the extension of the wind profile over homogeneous terrain beyond the surface boundary layer. *Boundary-Layer Meteorology*, 124(2):251–268.
- Holton, J. R. and Hakim, G. J. (2012). *An Introductory to Dynamic Meteorology*. Academic Press, Boston, fifth edition.
- Hu, B. (2015). Wind speed and wake studies using scanning LiDAR measurements. Technical report. ECN Wind Energy.
- International Energy Agency (2013). Ground-based vertically-profiling remote sensing for wind resource assessment. *IEA Wind RP 15*.
- Iungo, G. V. and Porté-Agel, F. (2014). Volumetric scans of wind turbine wakes performed with three simultaneous wind LiDARs under different atmospheric stability regimes. *Journal of Physics: Conference Series*, 524(1):012164.
- Iungo, G. V., Wu, Y.-T., and Porté-Agel, F. (2013). Field Measurements of Wind Turbine Wakes with Lidars. *Journal of Atmospheric and Oceanic Technology*, 30(2):274–287.

- Kumer, V.-M., Reuder, J., Dorninger, M., Zauner, R., and Grubisic, V. (submitted for review). Turbulent kinetic energy estimates from profiling wind LiDAR measurements and their potential for wind energy applications. *Renewable Energy*.
- Kumer, V.-M., Reuder, J., Svardal, B., Sætre, C., and Eecen, P. (2015). Characterisation of single wind turbine wakes with static and scanning WINTWEX-W LiDAR data. *Energy Procedia*, 80:245 – 254.
- NORDEX (2016). N80/2500 N90/2300. URL http://www.nordex-online.com/fileadmin/MEDIA/Produktinfos/EN/Nordex_N90_2300_GB.pdf. Last accessed on 12.Apr.2016.
- Pauliac, R. (2009). Windcube User’s manual. LEOSPHERE.
- Peña, A., Hasager, C. B., Lange, J., Anger, J., Badger, M., Bingöl, F., Bischoff, O., Cariou, J.-P., Dunne, F., Emeis, S., Harris, M., Hofsäss, M., Karagali, I., Laks, J., Larsen, S. E., Mann, J., Mikkelsen, T., Pao, L. Y., Pitter, M., Rettenmeier, A., Sathe, A., Scanzani, F., Schlipf, D., Simley, E., Slinger, C., and Wagner, R. (2013). Remote Sensing for Wind Energy. chapter 5. Pulsed lidar, pages 102–121. DTU Wind Energy. (DTU Wind Energy E; No. 0029(EN)).
- Schepers, J. G., Obdam, T. S., and Prospathopoulos, J. (2012). Analysis of wake measurements from the ECN Wind Turbine Test Site Wieringermeer, EWTW. *Wind Energy*, 15(4):575–591.
- Stull, R. B. (2003). *An Introduction to Boundary Layer Meteorology*. Kluwer Academic Publishing, Dordrecht, 9 edition.
- Wagner, R & Courtney, M. (2010). *Accounting for the speed shear in wind turbine power performance measurements*. PhD thesis. Risø National Laboratory for Sustainable Energy. (Risø-PhD; No. 58(EN)).
- Wallace, J. M. and Hobbs, P. V. (2006). *Atmospheric Science: An Introductory Survey*. Academic Press, 2 edition.

- Westerhellweg, A., Cañadillas, B., Kinder, F., and Neumann, T. (2013). Wind Flow Conditions in Offshore Wind Farms: Validation and Application of a CFD Wake Model. *Green*, 3(1):27–34.
- Westerhellweg, A., Canadillas, B., Kinder, F., and Neumann, T. (2014). Wake measurements at Alpha Ventus: Dependency on stability and turbulence intensity. *Journal of Physics: Conference Series*, 555(1):012106.
- Wu, Y.-T. and Porté-Agel, F. (2012). Atmospheric Turbulence Effects on Wind-Turbine Wakes: An LES Study. *Energies*, 5(12):5340–5362.
- Zhang, W., Markfort, C. D., and Porté-Agel, F. (2013). Wind-Turbine Wakes in a Convective Boundary Layer: A Wind-Tunnel Study. *Boundary-Layer Meteorology*, 146(2):161–179.